Summer 8-23-2019

Assessment of Helical Anchors Bearing Capacity for Offshore Aquaculture Applications

Leon D. Cortes Garcia
University of Maine, leon.cortes@maine.edu

ASSESSMENT OF HELICAL ANCHORS BEARING CAPACITY FOR OFFSHORE AQUACULTURE APPLICATIONS

By

Leon D. Cortes Garcia

B.S. National University of Colombia, 2016

A THESIS

Submitted in Partial Fulfillment of the

Requirements for the Degree of

Master of Science

(in Civil Engineering)

The Graduate School

The University of Maine

August 2019

Advisory Committee:

Aaron P. Gallant, Professor of Civil Engineering, Co-Advisor

Melissa E. Landon, Professor of Civil Engineering, Co-Advisor

Kimberly D. Huguenard, Professor of Civil Engineering

ASSESSMENT OF HELICAL ANCHORS BEARING CAPACITY FOR OFFSHORE AQUACULTURE APPLICATIONS.

By Leon Cortes Garcia

Thesis Advisor(s): Dr. Aaron Gallant, Dr. Melissa Landon

An Abstract of the Thesis Presented
in Partial Fulfillment of the Requirements for the
Degree of Master of Science
(in Civil Engineering)
August 2019

Aquaculture in Maine is an important industry with expected growth in the coming years to provide food in an ecological and environmentally sustainable way. Accommodating such growth, farmers need more reliable engineering solutions, such as improving their anchoring systems. Current anchoring methods include deadweights (concrete blocks) or drag embedment anchors, which are of relatively simple construction and installation. However, in the challenge of accommodating larger loads, farmers have used larger sizes of the current anchors rising safety issues and costs during installation and decommissioning. Helical anchors are a foundation type extensively used onshore with the potential of adjusting the aquaculture growth demand, though research understanding their lateral and inclined capacity needs to be performed first. This study addresses such topic by performing 3D finite element simulations of helical anchors and studies their reliability for offshore aquaculture farming. Results obtained in this research indicate that the helical anchors capacity could be related to either pure vertical or horizontal resistances, depending on the load inclination angle. Reliability evaluation of helical anchors for inclined loading demand from an oyster aquaculture farm using the Hasoferd-Lind method, indicated these anchors are feasible for operational aquaculture loads.

DEDICATION

To my family: my parents, Luz Marina and Ruben Dario, and sister, Sandy.

To my future wife: Laura.

Your support in this journey far away from home, made me stronger every time I needed.

ACKNOWLEDGEMENTS

I would like to thank the professors Dr. Melissa Landon and Dr. Aaron Gallant for giving me this life-changing opportunity. Thanks to them for their guidance that made me give the best of myself. To the professor Dr. Aaron Gallant I want to give my special thanks for the inexhaustible support during this process, always making a great effort helping me thinking in research ideas during really long meetings. From each of my professors, I take the best.

To the Sustainable Ecological Aquaculture Network (SEANET) supported by National Science Foundation award #IIA-1355457 to Maine EPSCoR at the University of Maine and the University of Maine System Research Reinvestment Fund (RRF). To the Maine Marine Composites staff, and Peter Morrison from Helix Mooring Systems, Inc. who helped me to understand and reconcile this research question.

To the UMaine Civil Engineering faculty, I appreciate the knowledge they shared to me and the way they did. Always understanding the students' weaknesses and making the best to explode all our potential.

To my civil engineering friends, Hakeem, Sohaib, Babak, Rachel, Preston, Astha, Belal, Jay, Pianpian, …, and everyone else that I forgot to mention, I am thankful to them for making this experience remarkable, charming, and especially delicious! (they all know why). To Peter, I dedicate these lines to express all the gratefulness I feel, his support and friendship made my second year something completely different. To my Latin-American friends, Daniela, Armando, Edna, Diana, and my good friend Danilo (“Nilo”), I say thanks for making this experience more joyful. To my brilliant and away friend Felipe Uribe-Henao I also say thanks for his advice and help when the numerical simulations requested that. To all of my friends, thanks for making this experience something that I will never forget.

Also, to my parents, Luz Marina Garcia Franco, and Ruben Dario Cortes Mosquera, my sister, Sandy Adyani Garcia Franco, brother-in-law Jesus Henao, and my little niece Maria Jose, I express my heartfelt thanks, for their support, and never-ending love, for accepting patiently my absence and respecting my personal realization goals. I say thanks to GOD for the health given to them and me.

Finally, to my loved girlfriend and future wife, Laura Ramirez Quintero, I say thanks for the constant support and encouragement during this process.

TABLE OF CONTENTS

LIST OF TABLES

LIST OF FIGURES

1 INTRODUCTION

1.1 Background

Aquaculture farming, the process of growing water-based organisms for human consumption, is a growing industry that is expected to supplement the food supply and help address challenges associated with a growing worldwide population. Aquaculture has shown great potential as a means to provide a reliable food source in an environmentally conscience manner to address these challenges. In Maine, this industry produces finfish, shellfish and seaweed, and contributes $35.7 million in income to residents (Cole et al. 2017). Local growth of this industry is consistent with worldwide trends, with growth expected to increase by 51 % by 2020 (Cole et al. 2017).

To accommodate this growth, more reliable and efficient engineering solutions for mooring and anchoring systems are desired to economically increase production and to move farms to deeper, more dynamic waters offshore (Menicou et al. 2012). In Maine, most aquaculture farms exist in estuarine rivers that are leased. Farmers typically rely on gravity anchors (concrete blocks) and drag embedment anchors (DEA) to resist lateral or inclined loads applied to mooring lines. While these anchoring methods have performed well, they have relatively low efficiencies (resistance to weight ratio) and installation requires the use of larger, more costly vessels and equipment. Costs have also continued to rise with growth of the industry and demand on these resources. Anchor decommissioning costs also pose a challenge, as farming regulations require removal of any structure, including anchors, at the end of a leasing period.

Helical anchors are an innovative foundation type regularly used for onshore applications and may provide an alternative anchoring solution that helps address many of the challenges previously mentioned. Helical anchors are lightweight, have a high efficiency, and different capacities are simple to achieve by increasing their number and/or size of the plates or the installation depth. These anchors are screwed into the ground and may be installed and

decommissioned relatively easily in some circumstances. For instances, some farmers simply use divers to install/uninstall these elements. However, little is known about their performance under this unique water loading. Onshore applications generally design the foundation such that helical anchors generate capacity in compression or tension via vertical loading. A significant amount of work and research has been conducted to understand the influence of depth, plate size, plate spacing, and soil type on the vertical capacity. While manufacturers often provide design recommendations regarding capacity for vertical loading, few design guidelines and recommendations are available to predict performance of helical anchors under lateral or inclined loading, as would be applied for aquaculture applications.

1.2 Objectives

This research focuses on an assessment of helical anchors under inclined loads so their use may be reliably extended to the aquaculture industry. The capacities of multiple commercial helical anchors are studied for a range of inclination angles and cohesive soil conditions. The study considers both the geotechnical and structural capacity of the anchor in development of a failure envelope. A reliability framework to address inherent uncertainties in design is also introduced, including an example for an oyster aquaculture farm located in an estuarine river in Maine (studied as part of the NSF sponsored SEANET project by others).

The main objectives of this research are: i) to present a methodology to evaluate the capacity of helical anchors under inclined loading, considering both the geotechnical and structural limits of this foundation type and ii) to develop a framework to efficiently evaluate this failure envelope and the reliability of helical anchors for aquaculture applications. The intellectual merit and potential to advance knowledge of helical anchors exists in the numerical evaluation of these elements under inclined loads, for which there is currently a paucity of field-performance data and limited experience using this foundation type to resist lateral and inclined loads. Broader impacts

of this research include the potential to make performance of helical anchoring systems more predictable, the potential to reduce anchoring cost, and the potential for lessons learned through this study to be applied to other offshore mooring systems.

1.3 Summary

This research is summarized in five chapters, including this introduction.

Chapter 2 is subdivided into two parts, where background information regarding aquaculture mooring systems and helical anchors is provided. The first part includes a review of aquaculture farming structures and the magnitude of mooring loads observed in other studies. The second part presents a review of helical anchors, which largely address vertical capacity, and the limited information on evaluation and performance of helical anchors subjected to lateral and inclined loads.

Chapter 3 presents detailed 3D finite element simulations for different helical anchors and different soil conditions. Though cohesive sediments are only considered in this study, strength and stiffness is varied. A methodology to compute the failure (capacity) envelope encompassing all inclination angles is presented based on findings from the finite element simulations.

Chapter 4 presents a framework to evaluate the reliability of helical anchors under inclined loads. An example of the helical anchors' reliability for an aquaculture farm whose loads were measured before, is also presented.

Chapter 5 provides a summary of the findings and conclusions from this study. This summary concludes with recommendations for future work.

2 BACKGROUND

2.1 Aquaculture Background.

To understand the type of loads and structures that need to be hold by helical anchors on the aquaculture industry, this chapter reviews and defines some important aspects that are helpful to understand the problem that is being addressed. A review of the type of aquaculture infrastructure and species is first presented, followed by the type of mooring systems used and the implications that they have on the anchor demand. After this, a review of the types of analysis performed to estimate the aquaculture loads is presented, summarizing the reported mooring loads at the end of the chapter. Finally, a review of the current anchoring systems used on the aquaculture industry is illustrated.

2.1.1 Aquaculture Infrastructure and Species.

Aquaculture is the process of farming aquatic organisms in either water- or land-based systems. Water-based systems are related to farming nearshore or offshore in places such as rivers, estuaries, or open sea. Land-based systems are artificial habitats such as ponds or tanks, where there is human control of water circulation. This thesis focuses on near-shore estuarine systems in Maine, where aquaculture farming is dominated by three species: i) finfish, ii) shellfish and iii) sea vegetables (Cole et al. 2017).

2.1.1.1 Finfish Cages and Net Pens

The process of finfish farming is usually performed using cages or net pens. These systems are located offshore, sometimes partially submerged to reduce or eliminate wave loading, and include a floating High-Density Polyethylene (HDPE) superstructure that prevents cages or net pens from sinking. Finfish cages dimensions range between 15 to 25 m diameter, 5-15 m depth, and are anchored to the seafloor with multiple mooring points. An example of different finfish

cages is presented in Figure 2.1. These cages shapes and rigidities will play a role in the determination of the drag forces as it will be discussed in the subsequent sections.

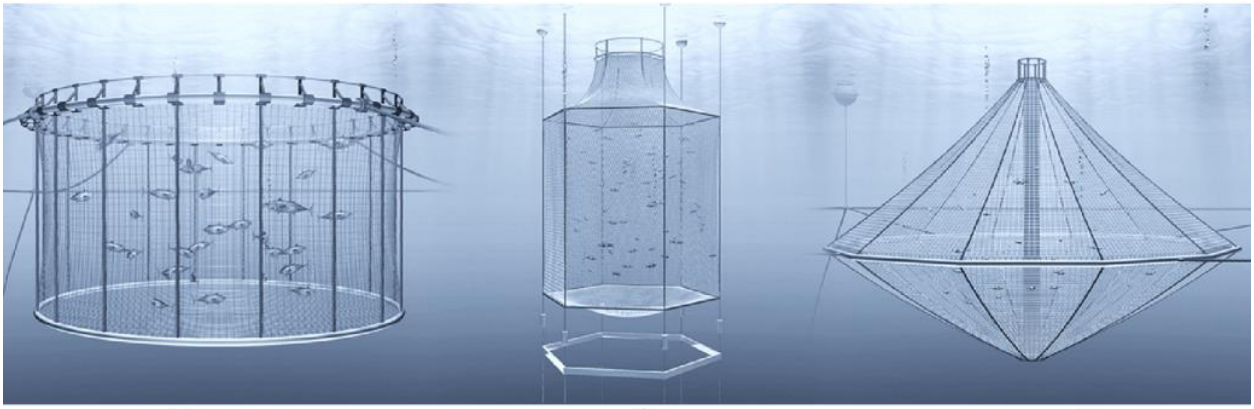

Figure 2.1. Aquaculture finfish cages: gravity flexible cage, b) tension leg system, c) rigid frame (Drach et al. 2016).

2.1.1.2 Long Lines: Floating Oyster Cages, Mussels' Socks and Seaweed

Long line systems consist of a surficial or submerged horizontal rope (head rope or main line) suspended with buoys and anchored at the ends. In this main lines, multiple aquaculture species (e.g., oysters, mussels, seaweed) are hanged or attached during the farming process (Figure 2.2).

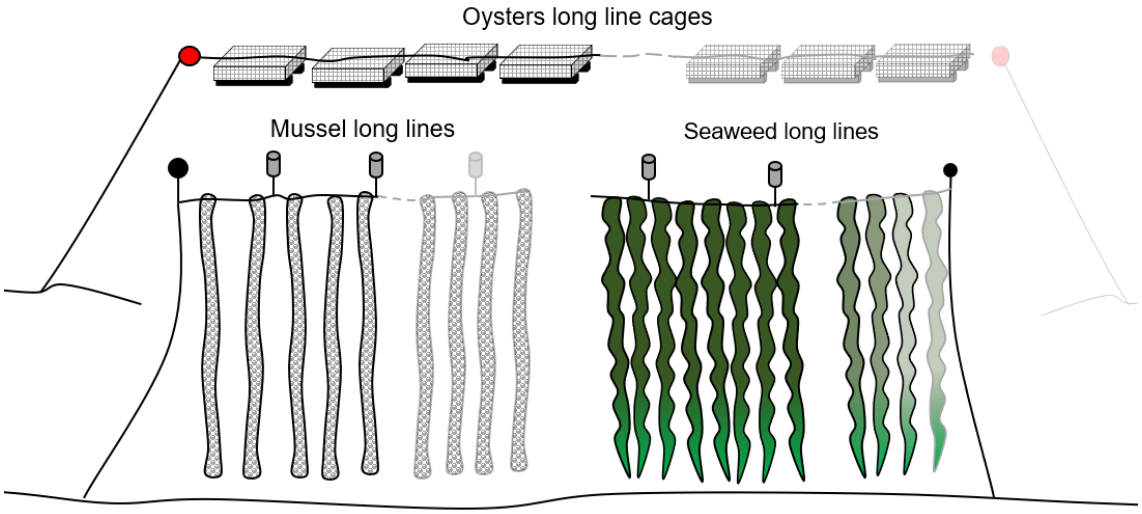

Figure 2.2. Long line farming schemes for oyster cages, mussel socks, seaweed.

Long line oyster farming is performed using floating bags or cages (smaller compared with finfish cages) that are placed one after another along the head rope. The idea behind the floating structures is that oyster get phytoplankton available at surface and the cages allow the water circulation. Typical cage sizes are 1 by 2 m approximately, and are arranged in systems of 40 to 50 cages together in water depths between 5 to 12 m. This farming system moves from one place to another to avoid seasonal temperatures that modify the growing process

Mussels farming is done using mussel "socks" consisting of a long net tube supported by a rope at its edge filled with juvenile shellfish. In long line structures, these socks are suspended consecutively along the mainline which requires more buoys to prevent sinking.

Sea vegetable farming is performed placing PVC pipes (approximately 5 cm diameter, 20 cm long) with plant spores along the head lines from where the seaweed will grow from the top to the bottom of the water column. Like mussel farming, seaweed long lines will need intermediate buoys to hold the system at surface.

2.1.1.3 Rafts Platforms

Shellfish rafts are floating steel or wood frames where vertical mussel "socks" are suspended (Figure 2.3). These structures are safe works stations from where farmers can handle the products in an efficient way. Typical dimension of the external frame are 12 meters, supporting up to 400 mussel socks, 14 m long approximately (Maine SEA Grant).

2.1.1.4 Aquaculture Farms Layouts

An aquaculture farm consists of one or more of the systems just discussed. Usually, aquaculture farms are placed in matrix arrangements with a system that attaches all the substructures (e.g. cages or rafts) together, and these ones to the sea floor in multiple points. Figure 2.4a and Figure 2.4b present the plan view of an aquaculture finfish and oyster farms in

southeast and central south Maine, respectively. Aquaculture farm layouts could imply a considerable number of individual elements which will increase the mooring loads due to an increase in the exposed. Further details of these interactions are addressed in multiples studies discussed in the next section.

Figure 2.3. Example of mussel raft. (Images: https://www.seagrant.umaine.edu/aquaculture/resources-for-shellfish-growers/aquaculture-methods-guide)

a) b)

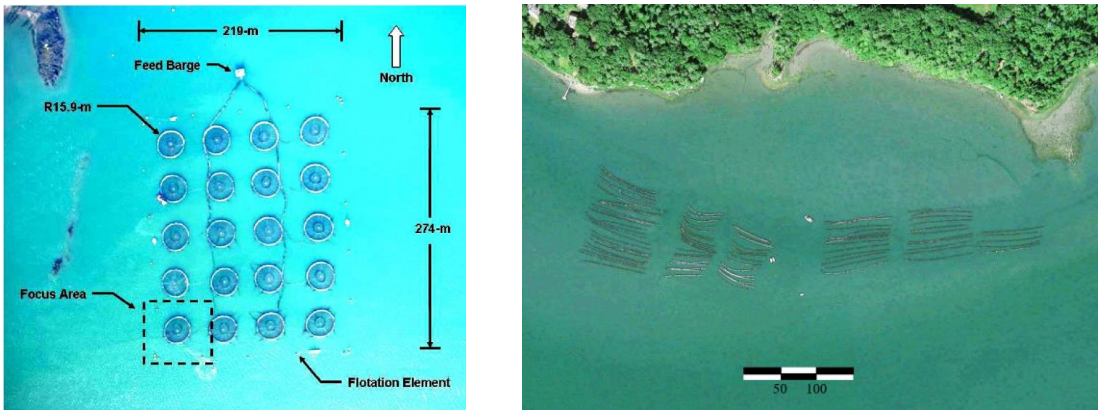

Figure 2.4. Examples of aquaculture farms arrangements for: finfish cages in South-east Maine (Fredriksson et al., 2006) a), and oyster cages in the Damariscota River, Maine. [scale in meters]

2.1.2 Aquaculture Mooring Systems

This section describes some characteristics of the mooring systems (ropes and chains) that transfer the drag forces from the aquaculture farm to the anchor head. As it will be discussed, differences in the mooring systems could lead to different anchor head loads even when drag forces on the aquaculture system are constant.

2.1.2.1 Mooring Types

Three types of mooring systems are used for offshore floating structures: i) catenary, ii) taut or semi-taut, and iii) vertical or tension legs. Catenary systems have a mooring rope or mooring chain attached at the seabed and forms a trigonometric curve leading to a floating system (Figure 2.5a). A large component of the load applied to the floating structure is absorbed by the weight of the steel catenary mooring line at the seabed, which mitigates sudden abruptly loads followed by a slack state (¨snap loading¨). A limitation of this system is the relatively large footprint required for the line extension, which is approximately two times the water depth that can be variable on an estuarine river (Randolph and Gourvenec 2011). In a catenary system loading at the anchor head is said to be horizontal, although, a small inclination of the chain at the anchor head is necessary to transfer the load. Taut or semi-taut systems (Figure 2.5b) are considered in deeper environments where the length of the catenary line is a limiting installation factor, due to its weight, or where a reduced farming footprint is desired. Inclined loads between 30 and 45 degrees (footprints per anchor of 1 to 1.5 the water depth) are resisted by the anchor (Randolph and Gourvenec 2011). The vertical mooring system (Figure 2.5c) is considered in water depths greater than 100 m for aquaculture applications (Turner, 2000) or 1000’s m for oil and gas industries using steel cables that in most of the cases are attached to deep piles (Randolph and Gourvenec 2011).

For the aquaculture industries placed in either open ocean or estuarine environments, the most used mooring system is the catenary mooring. This is due to the nature of the anchors used (drag embedment anchor or concrete blocks) where a preference to be loaded in the horizontal direction is due to gain friction resistance from the soil (concrete blocks) or maximize soil capacity (drag anchors). Further discussion of these anchors is addressed in section 2.1.4. Sometimes vertical mooring legs are used along the long lines as vertical droppers to prevent horizontal movement of these. Typical chain diameters for finfish aquaculture and in the order of 1 or 2 inches (e.g. Fredriksson et al 2008) and typical mooring ropes for shellfish aquaculture farming in shallow waters are lower than 1 inch. Typical factors of safety greater than 2 are used in design of these components (Fredriksson et al. 2008 and Nguyen et al. 2019).

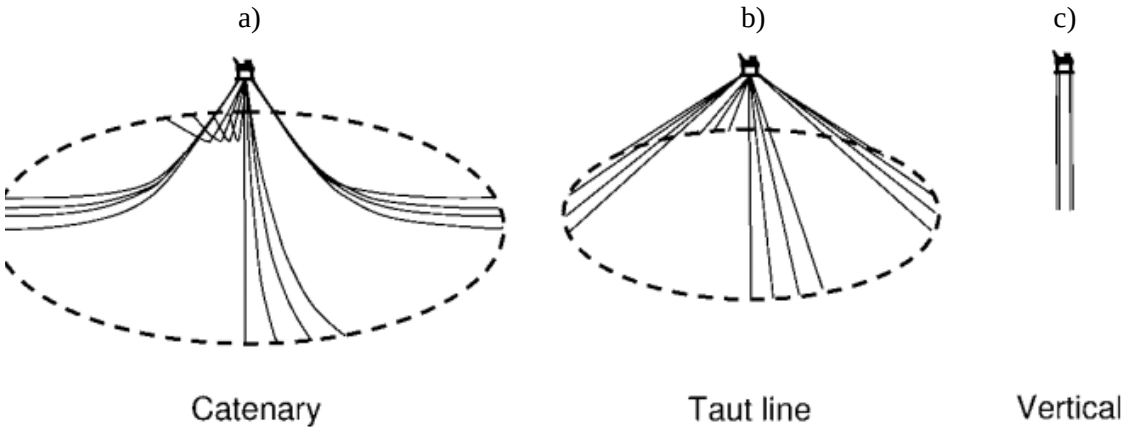

Figure 2.5. Floating mooring types: a) catenary, b) taut, c) vertical.

2.1.2.2 Initial Mooring Tension

A mooring consideration that depends on the desired movement of the structure, relates to tension in the line, which ca be slack or pre-stressed (Figure 2.6). Slack mooring is desired when single mooring points are considered, and movement is allowed. On this condition, there is a period when the mooring system, thus the anchor, do not experience any kind of loading. During a pre-

stressed condition, aquaculture systems are desired to stay in place and no movement is allowed. In estuarine farming systems, this condition is achieved by placing the farm on site during low tide and drowning the buoys, so when it comes to intra tides or high tides the system does not move around. This former type of mooring condition can avoid abrupt dynamic loading that could damage the system integrity. Rudi et al. (1998) recommended 3 kN pretension values for finfish cages mooring systems in open ocean and estuarine environments.

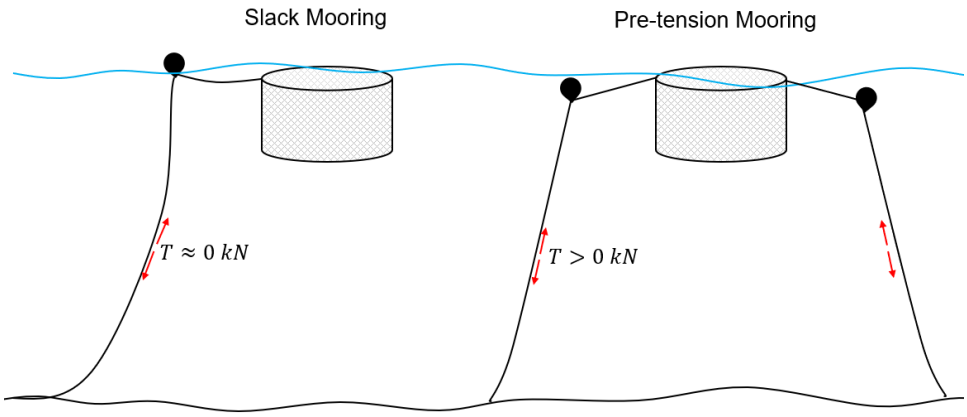

Figure 2.6. Slack and Pre-stressed systems.

2.1.2.3 Mooring Layouts

There are three types of fixed mooring layouts for aquaculture farming, where redundancy and fixities are the main variables. Figure 2.7a and b present twin and radial moorings layouts which are considered simple and easy to install; however, higher loads are expected in the anchors and redundancy is limited. Orthogonal moorings (Figure 2.7c) represents a more fixed and redundant system, however, more anchors are required. Single mooring points are also used in some cases as they have multiple environmental benefits due to the non-accumulation of sediments on the seabed, however, the lack of redundancy on these systems make them less popular.

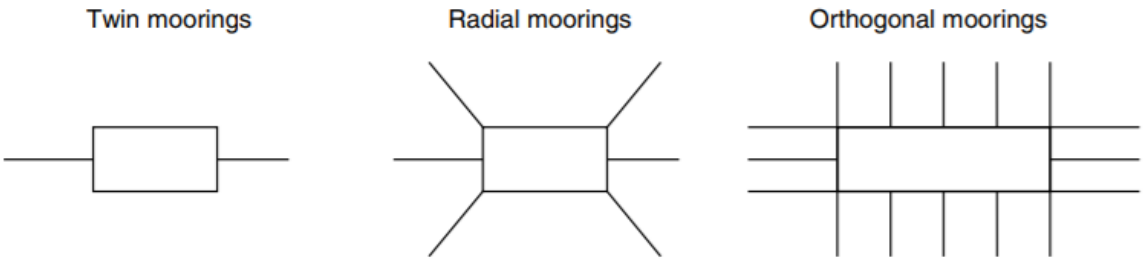

Figure 2.7. Aquaculture mooring layouts, (Turner 2000).

2.1.3 Aquaculture Mooring Loads

The main purpose of this section is to present a review of the different methods used to estimate aquaculture mooring line loads and present a review of the reported values in the literature. For this research, which is to study helical anchors under inclined loads, it will be ideal that mooring loads were recorded at the anchor head. However, loads are usually evaluated as drag forces on the aquaculture systems and then transferred with analytical solutions to the anchors heads. Other times loads are calculated or measured along the mooring line without considering the mooring line weight. In some mooring systems (e.g. taut or semi taut) it could be expected that the mooring line load at the fairlead is the same than in the anchor head, however, this might not always be the case, as it depends on the type of mooring used (e.g., catenary) which can modify the load at the anchor head. For the sake of clarification, the loads reported on the next section will be reported as mooring loads, so, the effects of the mooring line weight or inclination will not be considered.

Quantification of mooring line loads in an aquaculture system requires and understanding of multiple variables that are dependent on the environmental conditions (e.g., current velocity and direction, waves, wind, sea depth, biofouling) and structural considerations (e.g., farm dimensions and geometry, number of anchoring points, farmed species in the structure). These variables make this calculation a complex problem to approach. Most research aimed at determining mooring loads has been performed in finfish aquaculture (e.g., Fredriksson et al. 2004; Huang et al. 2009;

Vassiliou et al. 2012; Zhao et al. 2015), with some cases in shellfish and seaweed aquaculture (e.g. Olanrewaju et al. 2016; Gagnon and Bergeron 2017; Nguyen et al. 2019). Mooring design is not typically performed by small-scale farmers due to the difficulty associated with quantifying and understanding the influence of these variables. A trial and error approach is typically relied on by most of the farmers in Maine.

There are 4 methodologies for the quantification of these loads, being this: i) analytical analyses, ii) numerical analyses, iii) physical scale models, and iv) field measurements. A summary of the experience collected on the New Hampshire open ocean aquaculture project and the loads used in practical consulting for a Maine mooring design company, Maine Marine Composites (MMC), are summarized in the practical experience subchapter.

2.1.3.1 Analytical Analyses

Analytical analyses consist in the use of the Morison's equation (Morison et al. 1950) to determine the drag forces on the aquaculture system and then transfer this load to the mooring system, where the anchor load depends on the number of anchoring points. Morison's equation calculates inertial-(function of acceleration) and drag- forces (function of velocity) on an element submerged in a fluid. The inertial term is important when dynamic forces are applied to structures. Drag forces are considered under steady-state flow conditions where the water velocity is more influential on the body motion. Consideration of both forcing mechanism is computed as follows:

$$F = \rho C_m V \dot{u} + \frac{1}{2}\rho C_d A u|u| \tag{2.1}$$

where:

F: Total force on the object.
ρ: Water density.
$C_m = 1 + C_a$: inertia coefficient and C_a is the added mass coefficient.
V: Volume of the system.
$\dot{u}$: Flow acceleration.

F_D: Drag coefficient
A: Cross sectional area
u: Flow velocity.

When neglecting the inertial effects (e.g., in an estuary with not wave effects), the second term of the Equation (2.1) is dependent in large part on the drag coefficient, which differs based on the aquaculture cage, raft, or long line system that has been deployed. Difficulty in the determination of this coefficient also arises as it depends on the shape of the structure, current attack angle, number of individual cages/rafts/long-lines exposed to the current, and biofouling (Lekang 2008). Figure 2.8 presents how the current velocity changes the net shape, thus the drag coefficient. Drag coefficients also change with the cage shape (i.e. a cubic cage type is less aerodynamic than a cylindrical one). Typically, this coefficient is determined experimentally (e.g. Milne 1979; Aarsbes et al 1990; and Fridman and Danilov 1967, cited by Balash et al. 2009) and in most of the cases is defined in terms of the mesh solidity (mesh diameter and spacing), number of knots, and Reynolds number.

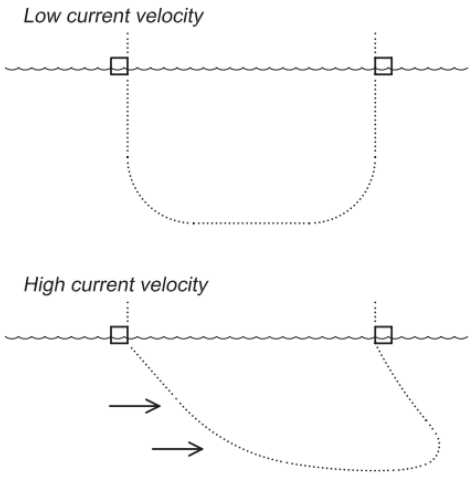

Figure 2.8. Finfish/cage shape changes due to currents (Lekang 2008).

A useful methodology to estimate drag forces on finfish aquaculture cages using rigid nets is presented by Lekang (2008) citing Løland (1993). This methodology computes parallel (F_{DP}) and normal (F_{DN}) drag forces (Figure 2.9) on an aquaculture system based on the current direction

as:

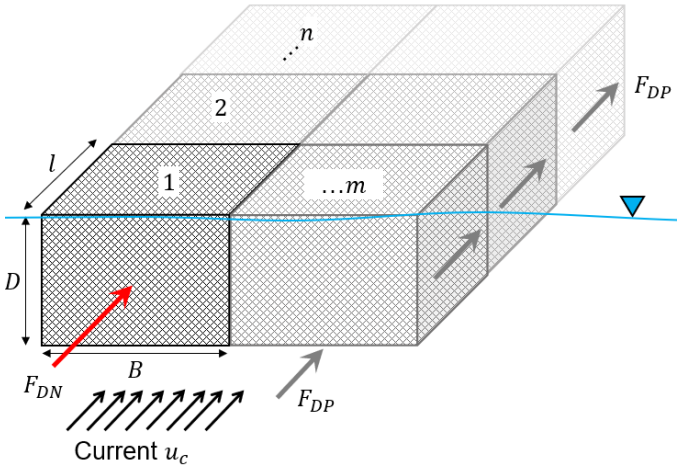

Figure 2.9. Current drag forces on aquaculture cages.

$$F_{DN} = \frac{1}{2}\rho C_{DN} u_c^2 (BD) m \left(\frac{1 - r^{4n}}{1 - r^2}\right) \tag{2.2}$$

$$F_{DP} = \frac{1}{2}\rho C_{DP} u_c^2 (B + 2D) l m \left(\frac{1 - r^{4n}}{1 - r^2}\right) r^2 \tag{2.3}$$

where:

F_{DN}: Normal drag forces
F_{DP}: Parallel drag forces
ρ: Water density.
C_{DN}: normal drag coefficient to the current direction
$C_{DN} = S_n - 1.24S_n^2 + 13.7S_n^3$ (Løland 1991)
S_n: solidity
$S_n = 2\dfrac{bar\ diameter}{bar\ length}$
C_{DP}: parallel drag coefficient to the current direction
u_c: current speed
B: cage width
D: depth of the cage
l: length of the cage bag
n: number of cages parallel to the current direction
m: number of cages normal to the current direction
r: reduction factor
$r = 1 - 0.46C_{DN}$

The total force on the system in then calculated as:

$$F_{D\,tot} = F_{DN} + F_{DP} \tag{2.4}$$

This simplified methodology will allow estimation and comparison to loads measured or computed in the following sections for finfish applications and summarized at the end.

As mentioned previously, when a catenary system is desired, the previous horizontal forces (drag and wave forces) can be used to dimension the chain length, assuming the catenary chain is heavy and that the drag forces on this are negligible. Fredriksson et al. (2008) presented a design example using of a catenary system, where the line tension is calculated based on Equation (2.5) and the length of the catenary is calculated using the Equation (2.6).

$$T = F_H \cosh\left(\frac{P \times x}{F_H}\right) \tag{2.5}$$

$$S = \frac{F_H}{P} \sinh\left(\frac{P \times x}{F_H}\right) \tag{2.6}$$

where:

T: Mooring line tension
F_H: Horizontal force (drag and wave forces)
P: Unit weight per length of chain
x: Horizontal position along the catenary chain

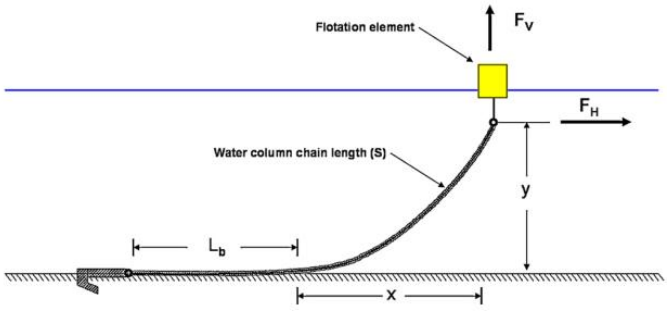

Figure 2.10. Catenary mooring geometric definitions (Fredriksson et al. 2008).

2.1.3.2 Numerical Simulations

The objective of this section is to summarize some studies that used numerical simulations to estimate mooring or drag forces on different aquaculture systems. Finite element analysis of aquaculture farms are advantageous because: (1) it couples multiple metocean conditions such as waves and currents at the same time, (2) it simulates a range of expected environmental conditions that may not be captured during field measurements, (3) it can represent the farm geometry and configuration with high accuracy, as opposed to theoretical analysis where the effect of the superstructure or the re-shape of the elements with time is not included, and (4) it computes stresses and strains applied to structural members, thus a better structural design can be approached, (5) multiple aquaculture configurations and layouts and orientations with respect to currents and waves attack angles can be studied to determine the most convenient design. However, these analyses do not couple the response with the anchoring and soil properties as it assumes the anchor is a rigid connection on the seafloor. For these reasons, most of the analysis presented herein presents either drag forces in the aquaculture structure that is not exactly on the anchor or mooring line (but it can be calculated with a mooring geometry) or mooring axial forces on the mooring lines that will be transferred to the anchor head.

Numerical analyses incorporate the two terms of Morison's equation in its calculations, as well as the Navier Stokes approach to solve the influence of turbulences and eddies on the structure. For seaweed aquaculture, Olanrewaju et al. (2017) presented a parametric dynamic analysis to estimate loads in a 100 x 100 m seaweed long line block with 30 planting ropes (100 kg each) planned at 200 m of Malaysia's coast. Three (3) models (mooring configurations) were analyzed with current speeds of 0.4 m/s. Models 1 and 2 had 8 mooring points and different mooring lines orientations, orthogonal and radial, respectively. Model 3 had 16 mooring points in a radial configuration. Analyzing a 10 m depth case scenario, it was found that mooring axial tension at the anchor head is approximately 2500, 1600 and 100 kN, for the models 1, 2, and 3, respectively. Note

the large differences in load reduction with the configuration and number of mooring points. When the model 3 was analyzed at 100 m water depth to assess its resilience, tension forces of approximately 270 kN were found.

On shellfish aquaculture, Kim et al. (2014) studied the effects of the implementation of abalone submergible cages in exposed marine environments in southern Korea. Abalone aquaculture is performed in submerged modules where arrangements of 16 containers (0.95x0.45x0.48 m) are placed in 3 m height and 4.2 x 4.2 m plan area frames, that attached with other 15 modules form an aquaculture farm. Farm dimensions are 14.1x14.1x3.2 m approximately with 4 mooring points at a water depth of 30 m. Two load cases were analyzed, submerged and surface cage, with both current and wave forces. Figure 2.11 shows how the maximum load is presented when the system is near the surface with a maximum anchor line tension of 172 kN.

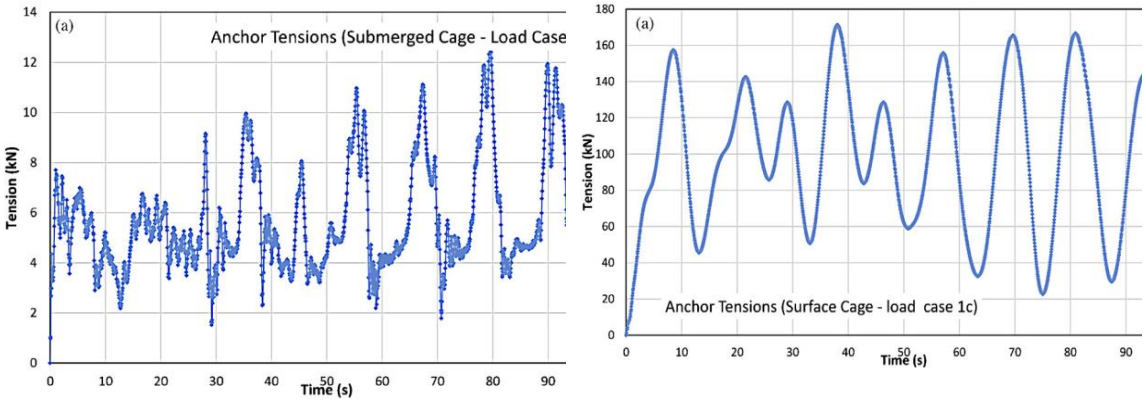

Figure 2.11. Force time series of a numerical analysis on abalone (shellfish) (after Kim et al. 2014).

For finfish aquaculture, Fredriksson et al. (2008) performed a preliminary design of an enclosed finfish concrete system located near Straits of Georgia, British Columbia, Canada. The concrete containment was cylindrical with 20 m diameter and 8 m height located on 20 m waters depth. Computational Fluid Dynamics (CFD) simulations were performed to know the drag coefficients through 4 x 11, 4 x 7, and 4 x 5 grids cages under multiple current velocities. Wave

forces were also computed using standard techniques and changing waves heights and wave periods. With the drag coefficients from the CFD analyses, Morison's equation was used to calculate the drag forces, neglecting the wave conditions. As a preliminary analysis the authors calculated horizontal drag forces on one cage and extrapolated these results to 4 cages obtaining loads of 256, 213, and 173 kN for systems with 44, 28, and 20 cages, respectively. Catenary mooring systems were analyzed obtaining tension forces of 73, 62, and 52 kN. Vassiliou et al. (2012) also performed a numerical approach of the loads presented at a typical Cyprus site with a 9x2 finfish net pens grid arrangement supported by 26 catenary mooring points, attached to 12-ton deadweight anchors. After considering a dynamic loading condition the maximum load in the anchor lines was 47 kN (Figure 2.12).

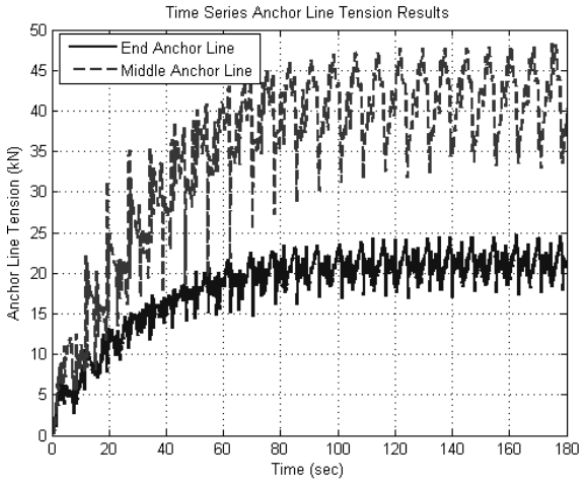

Figure 2.12. Loading time series of an anchor line in a 2 x 9 net pen grid exposed to 2 m height, 8 s waves and 0.4 m/s current (Vassiliou et al. 2012).

Drach et al. (2016) presented a numerical simulation for the design of a copper net gravity net pen for a site in the South Pacific. The cage was 20 m diameter with netting between a top and a bottom ring from where a concrete ballast weight was attached to prevent cage deformations. Dynamic results for storm events (9 m waves with a period of 10 s and collinear currents of 1.5 m/s)

are presented in Figure 2.13. Maximum mooring loads around 120 kN in an 8-anchor system are found for a shallow cage location.

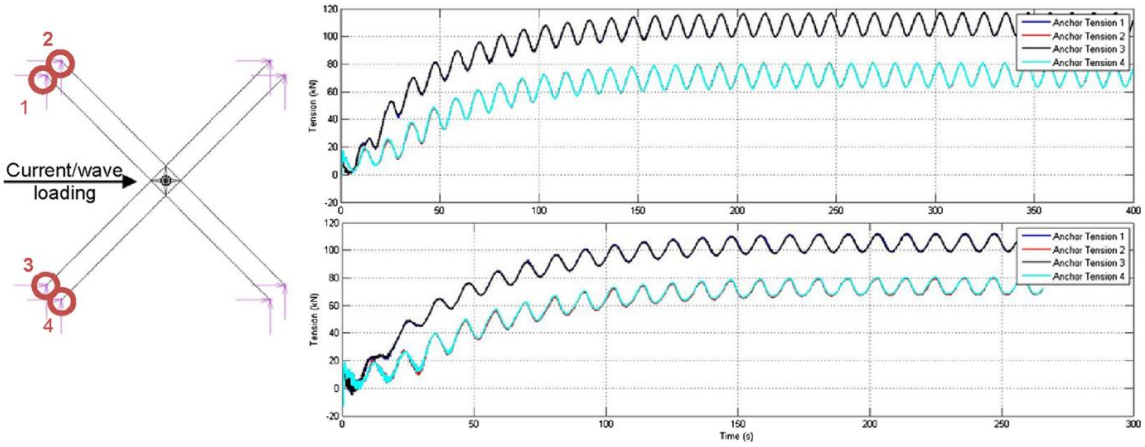

Figure 2.13. Mooring loading for an aquaculture net pen attached to 4 mooring points during loading. Top (surficial) bottom (submerged 10 meters) (Drach et al. 2016).

Huang et al. (2009) studied the loads on a 20 m diameter and 7 m height finfish cage attached to a single point mooring (SPM) system in Taiwan. The main purpose of this study was to assess the effect of a rigid frame on the loads and the reduction of the cage volume during a storm event. Results indicate that a rigid frame increases the load transferred to the mooring line but, reduces the volume deformation. After considering 50-year storm conditions with 6 m wave heights, 1 s period, and a current velocity of 1 m/s, maximum loads of 56 kN and 39 kN for a cage with a frame and a cage without it were calculated, respectively. Figure 2.14 presents the differences between the calculated loads after coupling both dynamic and kinematic effects. Note that during coupled analyses, current and waves loads are higher than the superposition of each force akin to changes in the deformation of the cage during loading, thus the drag coefficient. For the given metocean conditions and studied cages, the authors also analyzed a multi-cage farm in a one-row arrangement with current only and current and waves conditions. Equations 2a and 2b were obtained from statistical analysis and for a 5 cages system, mooring loads can reach a value of 145 kN, in a current and waves scenario.

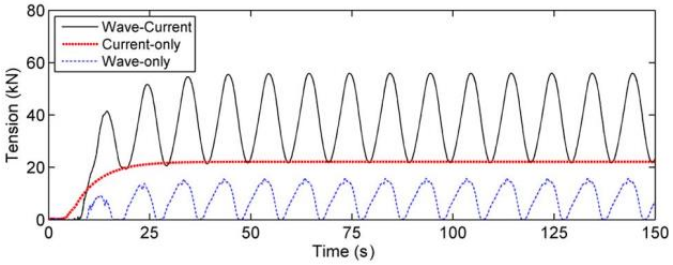

Figure 2.14. Influences of the dynamic effects of the waves and current forces.

Current only:

$$T_{max} = 7.72 \times N_{cages} + 16.10 \quad (2.7)$$

Current and wave:

$$T_{max} = 22.11 \times N_{cages} + 34.11 \quad (2.8)$$

where N_{cages}: Number of cages.

2.1.3.3 Physical Modeling

The estimation of aquaculture loads via physical models is advantageous as this approach attempts to simulate the environmental conditions that a prototype will experience, but often at a lower cost than field-monitoring programs. Additionally, the environmental conditions, including wave heights and currents velocities, are controlled. This methodology also overcomes the disadvantages of some numerical modeling where not all the effects are represented mathematically (e.g., the closure problem of the Navier Stokes equation). With these advantages, the physical model intent to predict the real behavior considering the geometry and environmental conditions as accurate as possible, however, for larger aquaculture farms it is said that some effects cannot be represented thus and underprediction of the loads is followed (Fredriksson et al. 2008).

Multiple finfish farms configurations were simulated in a 1:40 scale model by Zhao et al. (2015). Cages prototypes of 16 m diameter and 10 m depth were tested in a 56 m long, 34 m wide and 1 m deep tank. Figure 2.15 shows the maximum mooring loads for the studied configurations at a velocity of 0.9 m/s. It is also seen how the real maximum mooring line loads vary from 6.5 to

24 kN approximately, with maximum loads varying between 15 and 20% of the sum of all the mooring loads. These values percentages will be considered in the next subsection.

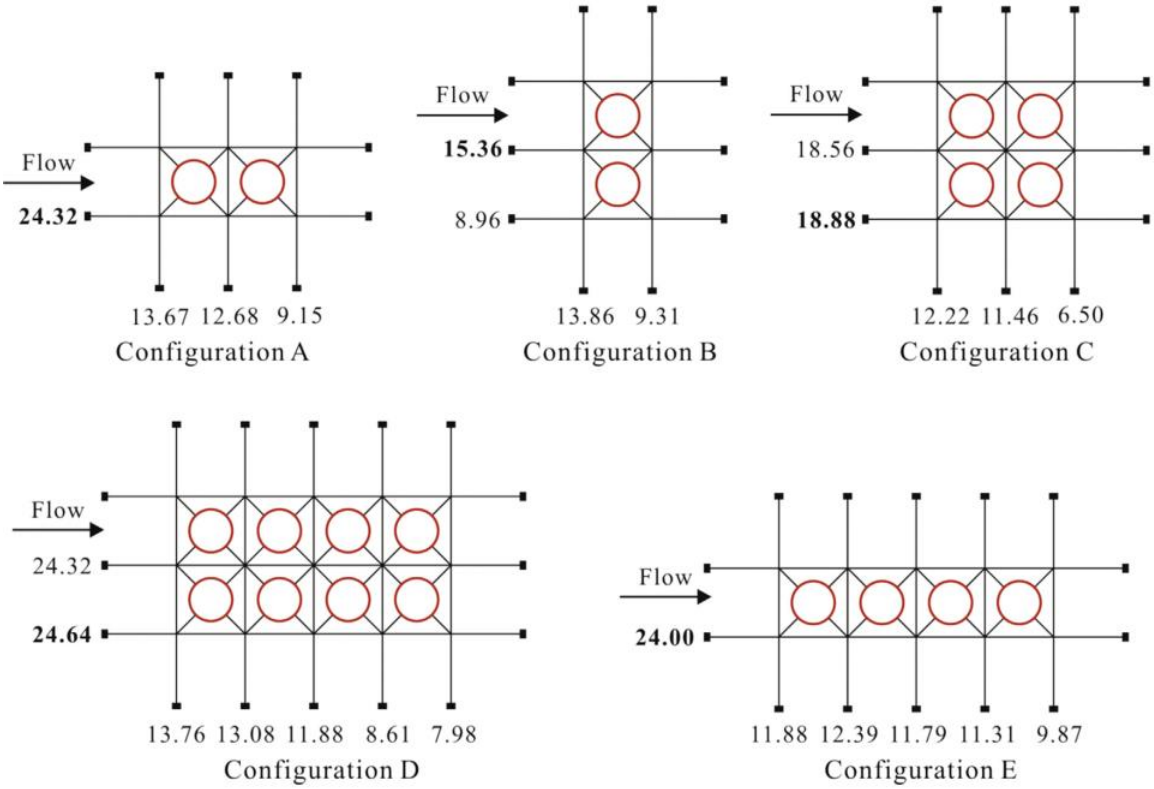

Figure 2.15. Mooring line loads on different finfish cages arrangements in water with 0.9 m/s currents (Zhao et al 2015).

Physical models in the Universiti Teknologi Malaysia, were performed to predict mooring loads on an aquaculture seaweed farm at South China Sea, Terengganu, Malaysia (Sulaiman et al. 2015). Models predict that for a 50-m depth moored system the design load could be around 39 kN.

2.1.3.4 Field Measurements

Field measurements from aquaculture farms are a direct measurement of the mooring loads applied to an anchorage system. When combined with measurements of metocean conditions, these measurements elucidate the environmental factors most influential to mooring line loads. However, field monitoring programs are expensive and often implemented for limited periods of time and

may not capture the most extreme environmental conditions. Field measurements are performed using load cells (Figure 2.16) attached to the mooring system and hard-wired to a data acquisition system to monitor the loads over time, usually weeks.

a) b)

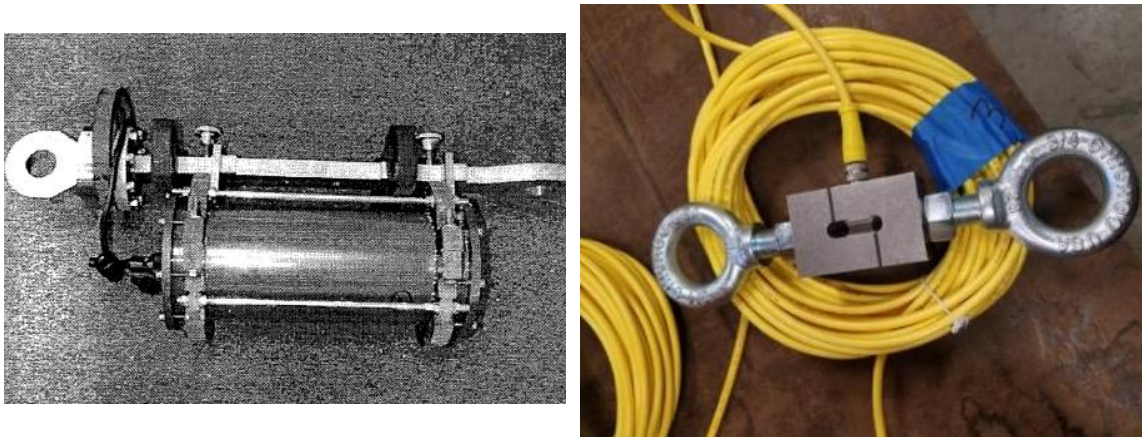

Figure 2.16. Load cells used to measure field loads a) 10k pounds and b) 5k pounds (from Irish et al. 2001 and Nguyen et al. 2019).

For shellfish aquaculture, Gagnon and Bergeron (2017), presented field study results in one mussel long line of a 15 long lines farm in the Gulf of St. Lawrence, Canada. The site has a depth between 20 and 24 m. The mooring system consisted of a 100-m mainline anchored at the ends by embedded anchors; also, intermediate modules anchored vertically by 81 kg concrete blocks were considered. The maximum load reported during the measuring time for the anchoring mooring lines was 580 N. Nguyen et al. (2019) presented a field data measurement for an oyster aquaculture farm in an estuarine river in Maine. The farm layout was 94.5 m long, 140 m wide, with two main horizontal lines from where 24 long lines (94.5 m long) with 45 cages each were attached perpendicularly. The average site water depth was 2.5 m and 18 mooring points (9 at each end) were used. During measurements, maximum loads of 3 kN where found on the mooring lines. The authors present the direct correlation between the tidal elevations a current velocity with the mooring loading (See Figure 2.17). A methodology to estimate mooring forces was also presented

from where in the worst-case scenario, a maximum load of 15 kN could be obtained for a tidal variation of 7 m in a 100-year return wave condition.

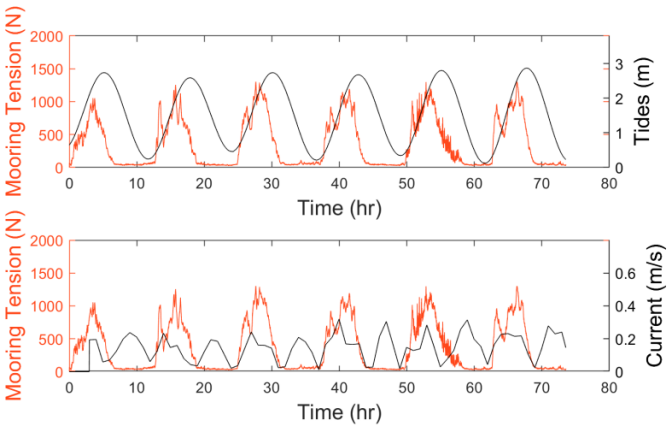

Figure 2.17. Relationships between tidal heights and velocities changes and mooring loads (Nguyen et al. 2019).

For finfish aquaculture, Colbourne and Allen (2000) presented a study of full-scale mooring loads for finfish cages close to Back Bay, New Brunswick, Canada, with the purpose of correlating the wave action on these loads. The water depth was between 20 and 30 meters at low and high tides. The aquaculture system consisted on concentric pipe rings 22 meters diameter moored to 8 lines. Each line had with it a load cell, from where loads were measured. It is shown that at this site, for a recording time of six weeks, between October 7 and November 17 of 1996, the maximum and extreme load was 2.4 kN and generally lower than 2 kN with a mean of 0.6 kN. Fredriksson et al. (2006) and Fredriksson et al. (2007) performed field data testing in an aquaculture site in down-east Maine, which is a site with a high tidal influence. The farm consists in a 5x4 grid with diameters around 30 meters each with a water depth around 15 m. Load cells in the anchor legs recorded a maximum load of 56 kN under working loads. Field instrumentation calculated the effect of waves on the mooring system, finding that waves heights and periods of 0.8 m and 2.2 s had a negligible effect on the anchor tension. In this study, the authors observed how the effect of biofouling increase the mooring loads akin to an increase in the drag forces (Figure 2.18). Clark et

al. (2018) present an example of how the biofouling effect on the mooring loads is extremely important, reporting a history case where a net pen with 35,000 salmon fish failed, releasing them to the environment.

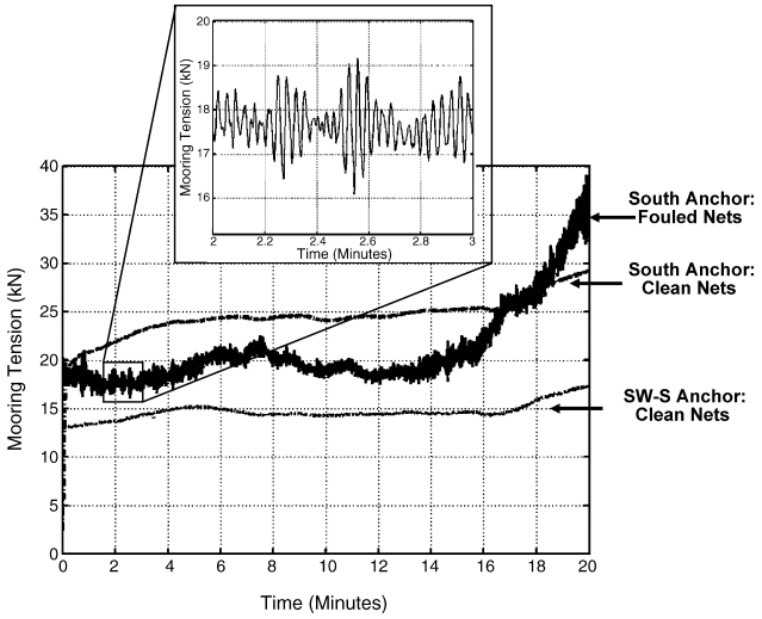

Figure 2.18. Effect of biofouling on the mooring loads (Fredriksson et al. 2007).

2.1.3.5 Practical Experience

An interesting project which presents a combination of the previous methodologies was performed by the University of New Hampshire (UNH). This project, called Open Ocean Aquaculture (OOA), is located at the south of the Isles of Shoals, NH, in the Gulf of Maine (Celikkol et al. 2006; DeCew et al. 2005; Fredriksson et al. 2000, 2004; Irish et al. 2001). During its implementation, multiple analyses and measurements of different types of finfish cages were performed to determine practical recommendations on the analysis and design of these ones.

Fredriksson et al. (2000) presented the design characteristics for the first trial at this site which consisted of 2 independent cages (16 m diameter each) in 50 m depth water with four mooring points each. The approach to do that was based on physical models. Maximum loads

measurements were taken in model tests, scale 1:22.5, as 54 kN. The selected design load of the system was 77 kN with anchor and mooring ropes factors of safety of 2.3 and 7.5, respectively. Irish et al. (2001) developed a system of load cells to monitor anchor mooring loads at the OOA site in those two fish cages. Records were taken during October 2000 to March 2001 until a failure in the recording system happened due to some storms presented at the site. The maximum load recorded during that period was around 3000 pounds (13 kN). Fredriksson et al. (2004) presented a numerical simulation and analytical formulation to design a four-grid system anchored in a catenary system at this site, its results present loads around 13 kN which were used to pre-size the system. Once doing this, a design load of 178 kN was obtained from a dynamical analysis. DeCew et al. (2005) performed numerical and physical scale models to know the performance of a modified cage and mooring systems there. The cage presented an irregular shape with a hexagonal plant view with 23 m diameter. Their results show that the mooring tensions loads would be around 25 kN or less, for an extreme case just related to the cage motion. When the authors performed a numerical simulation to include current loads, it is found that the mooring tension loads would be in the order of 160 kN.

Communications with Maine Marine Composites (http://mainemarinecomposites.com/), an engineering company dedicated to the design of aquaculture farms, offshore structures and boats, indicate that at small scale aquaculture farms (1-9 mussels rafts) the mooring load will be between 0.8 and 57 kN, and for large-scale aquaculture farms (four or more finfish cages) the load will be between 70 and 450 kN. These loads ranges are wide; however, they compare well with the studies reported herein.

2.1.3.6 Summary

A summary of the reported aquaculture loads for different metocean conditions and farm configurations is presented in Table 1. Under similar metocean conditions mooring loads are

different akin to farm configurations. As discussed previously, the estimation of mooring lines is a difficult process where dynamic (waves) conditions can be dominant and difficult to considerate. Nevertheless, aiming to give a context of a typical finfish farm cage subjected to current loads, the analytical solution provided by Lekang (2008) and Løland (1991) is compared with the reported results in Figure 2.19. There the drag (lateral) forces on a farm with 7 net pens of 20x20 m plan view sides and 7 m depth, aligned in the current direction are computed. Based on the results reported by Zhao et al. (2016), the maximum anchor load is calculated as the 20% of the total mooring forces. Then assuming a taut mooring line, inclined a β angle, the total mooring force at the anchor head is computed. Specific calculation details are presented in Appendix A

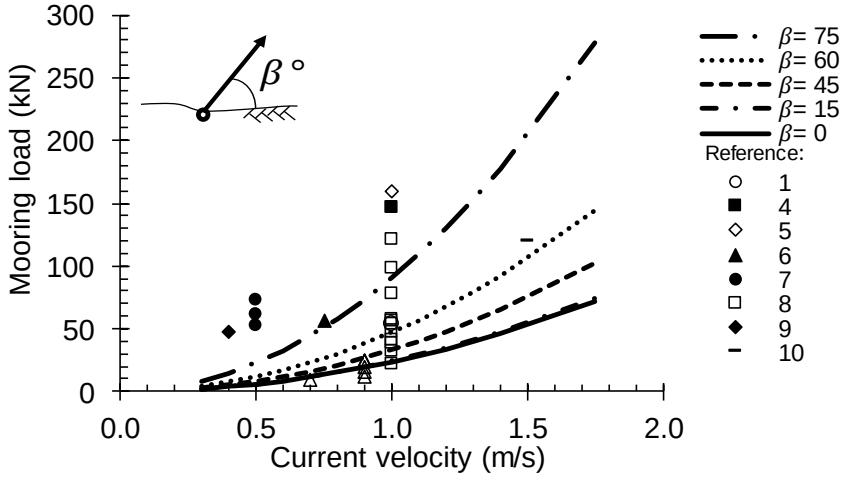

Figure 2.19. Summary of finfish aquaculture loads compared with theoretical solutions

Table 2.1. Summary of aquaculture loads and metocean conditions.

Reference	Study Type	Mooring System	Anchor Type	MP	No. Cages /longlines (-)	Dimensions B/L (m)	Dimensions D (m)	Water Depth (m)	Metocean conditions u (m/s)	Metocean conditions H (m)	Metocean conditions T (s)	Tidal range (m)	Max. Mooring load (kN)
Aquaculture Cages													
1 Fredriksson et al. (2000)	PM	K	DEA	6	2	16	6	55	1.0	7.98	8.15	-	54
2 Coulbourne and Allen (2001)	FM	SM-K	DEA	8	13	22	5	30	NR	-	-	10	2.6
3 Irish et al. (2001)	FM	K	DEA	4	1	16	6	52	NR	NR	NR	-	13
4 Fredriksson et al. (2004)	NM	K	DEA	12	4	25-15	15-9	52	1.0	9	8.8	-	147
5 DeCew et al. (2005)	NM-PM	SM	DW	3	1	23	NR	52	1	9	8	-	160
6 Fredriksson et al. (2006)	FM	NR	NR	26	20	31	NR	15	0.8	0.8	2.2	8-9	56
7 Fredriksson et al. (2008)	NM	K	DEA	34	44	20	8	20	0.5	-	-	-	73
				26	28					-	-	-	62
				22	20					-	-	-	52
8 Huang et al. (2009)	NM	SM	DW	1	1	20	7	30	1.0	6	10	-	39
					1				1.0	-	-	-	56
					1				1.0	-	-	-	22
					2				1.0	-	-	-	33
					3				1.0	-	-	-	41
					4				1.0	-	-	-	47
					5				1.0	-	-	-	53
					1				1.0	6	10	-	57
					2				1.0	6	10	-	79
					3				1.0	6	10	-	98
					4				1.0	6	10	-	122
					5				1.0	6	10	-	146
9 Vassiliou et al. (2012)	NM	K	DW	26	18	20	NR	18-70	0.4	2	8	-	47
10 Drach et al. (2016)	NM	K	DW	4	1	20	10	50	1.5	9	12	-	120
11 Zhao et al. (2016)	PM	NR	NR	8	1	16	10	20	0.7	-	-	-	9
				8	1				0.9	-	-	-	12
				10	2				0.9	-	-	-	24
				10	2				0.9	-	-	-	15
				12	4				0.9	-	-	-	19
				16	8				0.9	-	-	-	25
				14	4				0.9	-	-	-	24
Long lines Seaweed Aquaculture													
12 Sulaiman et al. (2015)	PM	NR	NR	2	1	100	-	50	2	-	-	-	25
13 Olanrewaju et al. (2016)	NM	NR	NR	16				10				-	100
				16				100				-	270
				8	30	100	-	10	0.4	1.5	10	-	2500
				8				10				-	1600
Long lines Shellfish Aquaculture													
14 Kim et al. (2014)*cage	NM	K	-	4	16	4	4	30	1.0	8	12	-	172
15 Gagnon and Bergeron (2017)	PM	K-TL	DW	2	1	100	-	20-24	0.2	3.5	-	1	0.6
16 Ngyen et al. (2018)	FM	SM	HA	18	24	94.5	-	2	0.3	-	-	3	3.0
					45			2		-	-	3	4.8
					24		-	2		-	-	7	11.0

Note: PM: Physical Modeling, FM: Field Measurement, NM: Numerical Modelling, K: Catenary, SM: Taut Semi-Taut, TL: Tension Legs, DEA: Drag Embedment Anchor, DW: Dead Weight, MP: Mooring Points, B: Cage diameter, L: Long line length, D: Cage depth, u: current velocity, H: Wave height, T: Wave period, NR: No Reported.

2.1.4 Aquaculture Anchors Uses

The current state of the art of the aquaculture foundations around the world consists in deadweight anchors as well as drag embedment anchors (DEAs). In some cases, aquaculture farmers seeking for redundant anchoring systems, use a combination of both methods in the same mooring line (from personal conversations with New England University and Cook Aquaculture in Coobscok bay).

Deadweight anchors (Figure 2.20a) are advantageous as: i) the capacity is obtained from their self-weight and the friction between this and the soil, ii) a deep knowledge of the soil properties is not required, iii) they can be loaded in multiple directions, iv) they are simple to construct and install. However, when this kind of anchor is used to hold larger loads than they use to hold (10-12 tons) (Buck and Bucholz 2004; Stevens et al. 2008; Vassiliou et al. 2012; Cardia and Lovatelli 2015) difficulties deploying and decommission are presented due to limitations in the available installation vessels and cranes sizes. This problem could be solved leasing large vessels and cranes; however, this implies an increase on the installation and decommissioning costs. In terms of their efficiency (ratio of load capacity to anchor weight) deadweight anchors could have approximate values of 0.5 and 0.3, while loaded vertically and horizontally in sandy soils, respectively.

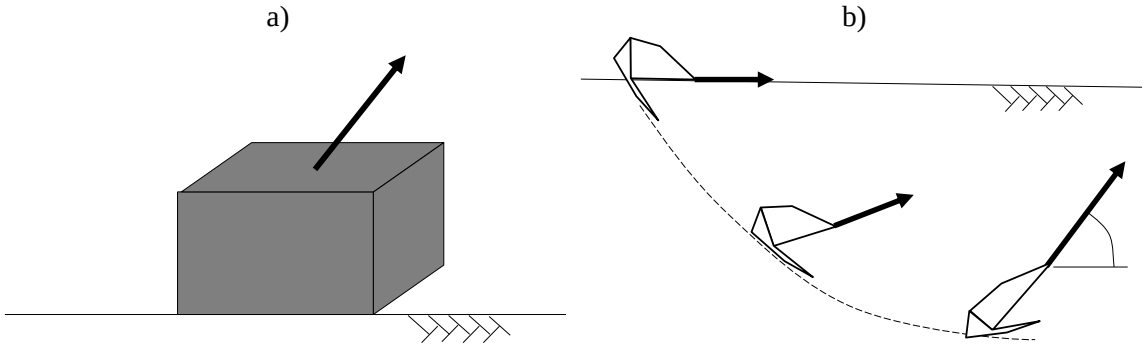

Figure 2.20. Current anchoring systems for aquaculture applications: a) concrete blocks, b) drag embedment anchors.

Drag embedment anchors (DEAs) are advantageous as they have greater efficiency (2.5 to 3.5) than dead weights since they get the capacity from their self-weight and soil resistance (Figure 2.20b). Some drawbacks of the implementation of the DEAs are: i) cost associated with soil properties investigation, anchor design, and installation, ii) preferential lateral loading limiting the inclination angle with respect the horizontal (Aubeny and Chi 2010; Vryhof 2018), and iii) environmental damage due to seabed dragging.

In terms of the capacity, the design of these elements considers certain characteristics of the seabed. It is said that if most of the bed is composed of rocky elements, deadweights will be a better option, as DEAs will no embed into the floor; on the other hand, if the bed is composed of muddy materials, DEAs will reach a good embedment (Cardia and Lovatelli 2015). Special attention needs to be taken locating deadweights in hard clay beds where drag forces could move these foundations (Cardia and Lovatelli 2015). The reliability of these anchors is considered another limitation as a not good characterization of the bed is well-thought-out and the trial and error method is executed most of the time (Menicou et al. 2012).

Some recent advances in aquaculture operations have reported the use of helical anchors as for anchoring systems in Europe (e.g., Hafbor n.d., FMS 2018) and some parts of the US (Catalina Sea Rach n.d., Helix Mooring Systems 2016). Their use is promising but still they are not completely popular due to installation limitations which is starting to be addressed by these companies. Further details about the behavior of helical anchors are giving in the next sections.

2.2 Helical Anchors Background

Helical anchors are a lightweight and efficient anchor type with a large potential to be used in offshore environments such as aquaculture farming or marine renewable energy. This chapter introduces the reader to helical anchors geometric definitions and presents a review of the previous studies published, aimed to understand the helical anchor behavior and to predict their capacity under multiple loading demands (e.g., vertical, lateral, inclined, or cyclic). After such review an appraisal of the installation procedures performed onshore is presented. Finally, this chapter presents a summary of the loads hold by helical anchor on previous studies which serve as proof of the potential of helical anchors for aquaculture applications.

Different denominations for helical anchors exist (e.g., screw anchors, helical piles, screw piles) which is related to the loading direction (compression or pullout-tension), nevertheless, all of them refer to steel foundations composed of a vertical cuboid-(square shaft) or cylindrical-(round shaft) section from where perpendicularly discrete helical plates are attached. Figure 2.21 presents an example of a helical anchor with two plates and its respective geometric definitions used in this research. To install them, a torque and a push is applied to the shaft, so it buries into the ground and once the helical plates are in contact with the soil, they screw the anchor in shearing the soil. After installation, this foundation is designed to sustain either axial (compression or tension) or lateral loads.

Helical anchors were first developed by the civil engineer Alexander Mitchel in 1836 in London, and the first uses of this technology were associated with offshore lighthouses and ship moorings (Lutenegger 2011). The use of these foundations expanded to ocean front piers, bridges, underpinning and anchoring to the ends of 1880s and was considered a great advance in the engineering field for that time (Lutenegger 2011). With the development of different foundation methods as driving piles, bored piles, and grouted anchors, among others, the use of helical anchors

offshore declined between the late 1890s and 1990s, when applications were more prevalent onshore (Lutenegger 2011; Perko 2009).

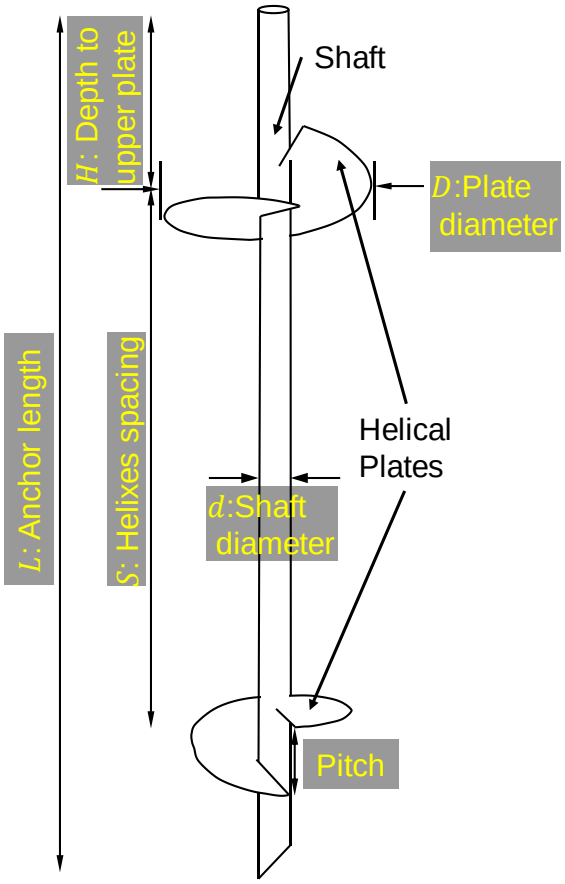

Figure 2.21. Helical anchor with square shaft.

Currently, helical anchors are well established in multiple uses onshore such as house foundations, buildings, construction additions, underpinning, light poles, pedestrian bridges, guy wire anchors, transmission towers, nature walks, excavations tie-backs and wind energy towers (Perko 2009). Helical piles are included in the International Building Code 2015 (IBC 2015), as deep foundations (Chapter 18, Section 1810) where structural and geotechnical design specifications are given for compression and tension loading.

Little information it is found in the literature with respect of the current use or design of helical anchors offshore, although their first uses were performed for such applications, there is not a guideline for such design. What does is recognized on the literature is the potential of helical anchors offshore for aquaculture or marine renewable energy solutions (Stevens et al. 2008; Gaudin 2014; Byrne and Houlsby 2015; Houlsby 2016; Lutenegger 2017; Mohajerani et al. 2016).

2.2.1 Helical Anchors Bearing Capacity

In this subchapter it is presented an overview of the available design methods and investigations performed on helical anchors aimed to explain its behavior under vertical, lateral, inclined, and cyclic loading conditions. Herein it can be seen how the bearing capacity varies due to the anchors' geometry, soil type, and loading direction.

2.2.1.1 Vertical Loading

Three methodologies are available for the determination of the geotechnical vertical capacity either in compression or tension, being these: i) cylindrical shear, ii) individual bearing plates and iii) torque correlation. The first two theories are based on the way the soil-anchor interaction develops the resistance (Mitsch and Clemence 1985; Mooney et al. 1985), while the latter is based on field experience where the anchors' capacity is associated with the torque requested to install it as of a way to perform indirect field testing.

The cylindrical shear method (Figure 2.22) assumes that at failure, a cylinder circumscribed by the helical plates perimeters it is formed, getting the resistance from the soil-soil friction contact, and that at the top (uplift) or bottom (compression) plate a bulb mobilizes the resistance as a function of the anchor geometry and depth. The generalized equation of this condition is:

$$P_u = \pi D_{avg}(m-1)S\tau + A_t q_{ult} + Q_{sh} \quad (2.9)$$

where P_u: is the ultimate geotechnical capacity, D_{avg} is the average plate diameter, $(n-1)S$ is the length of the created cylinder, m number of plates, τ is the soil shear resistance, A_t is either the top or bottom helix area, q_{ult} is the soil ultimate bearing capacity calculated as a function of the soil shear resistance and geometry, and Q_{sh} is the resistance around the shaft above the upper plate, depending on the adhesion or friction between the soil and the shaft.

The soil ultimate bearing capacity q_{ult} is determined based on the way the plate makes the soil fail, where helical anchors at shallow depths in sands, make the soil forming a cone to the surface (Mitsch and Clemence 1985), nevertheless for deep cases in sands and clays the ultimate soil bearing pressure, q_{ult}, could be defined in terms of the Terzaghi bearing capacity equation for circular foundations:

$$q_{ult} = 1.3cN_c + q'N_q + 0.3\gamma DN_\gamma \tag{2.10}$$

where c is the soil cohesion, q' is the effective pressure at the plate depth, γ is the soil unit weight, and N_c, N_q, and N_γ are bearing capacity factors function of the soil shear resistance. The previous expression is valuable nevertheless much of the research performed on helical anchors have determined that these factors are different for helical anchors than for shallow and deep foundations and dependent on the loading direction. For the clayey soils, the focus of this research, it is said that the bearing soil ultimate capacity should be computed as:

$$q_{ult} = N_c s_u \tag{2.11}$$

where s_u is the soil undrained shear strength.

The individual bearing capacity method (Figure 2.22) assumes that the anchor obtains the capacity from the soil bearing capacity above or below each plate, depending on the loading direction, uplift or compression, respectively. The anchor capacity for this method is:

$$P_u = \sum_n q_{ult} A_n + Q_{sh} \tag{2.12}$$

where the parameters have been previously defined.

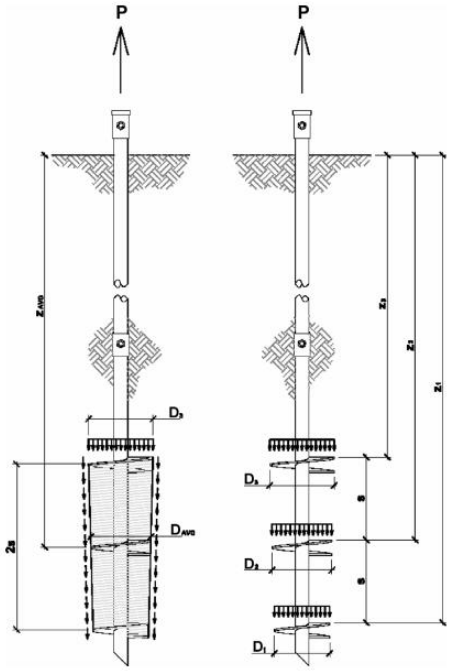

Figure 2.22. Cylindrical shear an individual plate bearing capacity methods (Perko 2009)

The torque correlation method was presented by Hoyt and Clemence (1989) as an approach to reduce the uncertainty of the prediction of the ultimate capacity based on poor soil shear resistance characterization. This methodology correlates the ultimate anchor capacity to the installation torque as:

$$P_u = k_T \times T \tag{2.13}$$

where k_T represents the torque correlation factor, and T is the average installation torque at the design depths. Hoyt and Clemence (1989) presents k_T values of 33 and 23 m^{-1} for square and round anchors with less than 89 mm shaft diameters, and 9.8 m^{-1} for anchors with 219 mm shaft diameter. Manufacturers (e.g., Hubell/CHANCE 2014; Magnum 2016) recommends the use of this methodology with torque correlation factors between 30 m^{-1} and 0.6 m^{-1} for small (1.5”

diameter) square shaft and for large (10" diameter) circular shafts, respectively. Note that no distinction is presented in most of the cases for this methodology for the type of soil or the loading direction (compression vs. uplift). Perhaps this method has been used it has been demonstrated that this method lacks on a match between the laboratory and field testing and do not represent a real failure mechanism (Perko 2000).

Parametrical studies

To correlate the geotechnical capacity of helical anchors with its geometry under vertical loading (compression or uplift), multiple parametrical studies have been performed using physical scale or centrifuge testing (e.g., Narasimha Rao et al. 1991, Narasimha Rao and Prasad 1993, Wang et al. 2010; Stanier et al. 2013,), numerical finite element simulations (e.g., Livneh and El Naggar 2008; Merifield 2011; Wang et al. 2013) and field testing (e.g., Abdelghany and El Naggar 2010; Sakr 2010a;b; Li et al 2018).

To find the critical spacing that separates the failure mechanisms proposed before, Narasimha Rao et al. (1991) and Narasimha Rao and Prasad (1993) performed numeral physical scale testing on helical anchors. Results indicate that for a spacing ratio (S/D_p) greater than 1.5 the failure mechanism was not cylindrical and conversely individual bearing plates, being maximum pull-out loads reached during the cylindrical shear development. Other laboratory studies performed by Stanier et al. (2013) and Wang et al (2010), validated the presence of the cylindrical shear failure for spacing ratios lower than 3, and numerical simulations with Large Deformation Finite Element (LDFE) methods indicates that the threshold where local failure occurs in plates instead of the cylindrical shear is around 3.2 (Wang et al. 2013). However, in contrast to these findings, Lutenegger (2009) presented field data testing, demonstrating that these thresholds do not apply for stiff soils.

In terms of the embedment depth, Lutenegger (2009) defined deep helical anchors for depth ratios H/D greater than 6, where the failure surface is similar to deep foundations, whereas Narasimha Rao et al. (1993), describes deep anchors when H/D is greater than 4 and no cracks are observed in surface. Narasimha Rao et al. (1993) also defined shallow anchors, when H/D<2, and the shear resistance is attributed to the cylinder formed by plate diameters and tension cracks are presented; and transition anchors, when 2<H/D<4, here the ultimate pull-out loading has contributions of the cylinder formed by the plates, the shallow plate resistance and shaft skin resistance between the shallow plate and the surface, some light cracks are observed in the surface.

When determining the breakaway factor, Nc, to estimate the upper plate bearing resistance, multiple discussions have been set in terms of which factors should be used, with a variation of these between 9 and 19. Money et al. (1985) and Narasimha Rao et al. (1991) recommend the use of breakaway factors determined by Meyerhof (1951) for single plates and validated with tests performed on plate anchors by Adams and Klym (1972) and Meyerhof and Adams (1968). These theories assume that the soil under tension has a similar load behavior than under compression with critical breakaway factors between 9 and 10. Adding to this method, Perko (2009), recommends using a value of 9 based on the theory presented by Skempton (1951) for deep foundations after including shape and depth factors. Merifield (2011) performed numerical simulations on helical anchors to determine the breakaway factors on multi-plate anchors, finding a critical value of 12.6. Young (2012) and Stuedlein and Uzielli (2014) analyzed real data on helical anchors testing to back-calculate this parameter. Young (2012) proposed a critical value of 11.4 for a relative depth greater than 6 and Stuedlein. Uzielli (2014) found a variation of the N_c values from 8 to 16 approximately, with a mean value close to 10. Figure 2.23 presents a summary of the back calculated values and equation proposed by Young (2012)

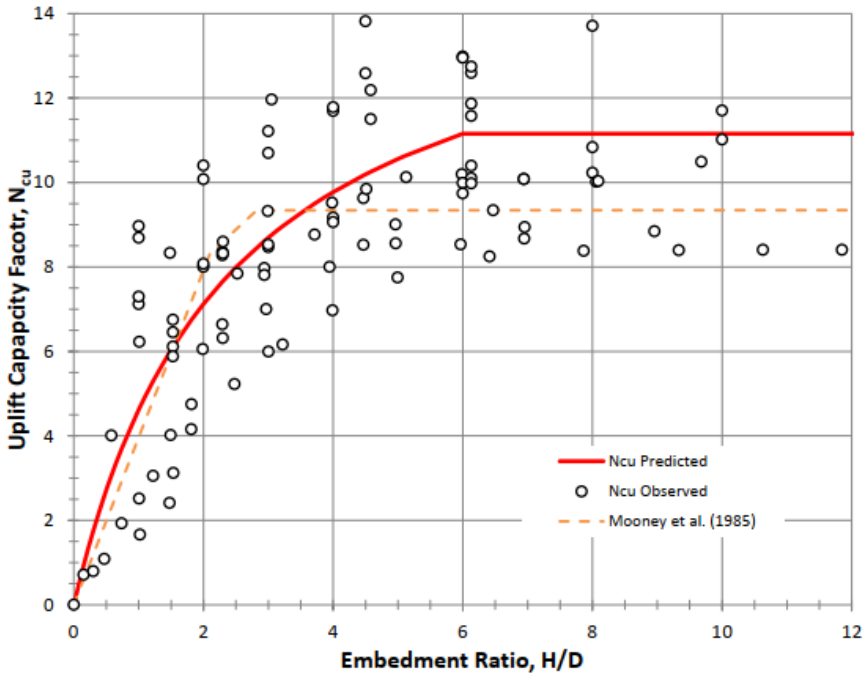

Figure 2.23. Changes in uplift breakaway factors with depth for helical anchors on clays (Young 2012)

Axial Load Transfer (ALT) has also been part of the discussion studying helical piles/anchors, to understand how much of the applied load it is being held by the helical plates or shaft. It is considered that the best way to predict this behavior is with the installation of strain gages (Figure 2.24) along the shaft at different depths. Abdelghany (2008), Abdelghany and El Naggar (2010) (2016) installed strain gages on small square shaft helical anchors (45 mm square shaft, 8”-10”-12” plates, 3.6m total length) under compression in clays founding that 12 to 16% of the load was taken by the shaft above the top helix, 38 to 62% by the inter-helix resistance, and 26 to 46% by the bottom helix. Zhang (1999) also study ALT in large shaft diameter helical anchors ($D/d = 1.6$) under compression and tension. Results indicate that under compression, the upper shaft resists from 35 to 40% of the load, while the interhelix zone takes from 40 to 20% of the load and the bottom helix around the same amount (20-40%). Tension test performed by Zhang (1999) on a short pile (SP) and a long pile (LP) indicate that 40% of the measured load is held by the upper

shaft in both cases, but with different distributions, having the SP more contribution from the surficial part. Figure 2.25 presents a normalized comparison of the axial load distributions at the ultimate loads applied for the previous cases.

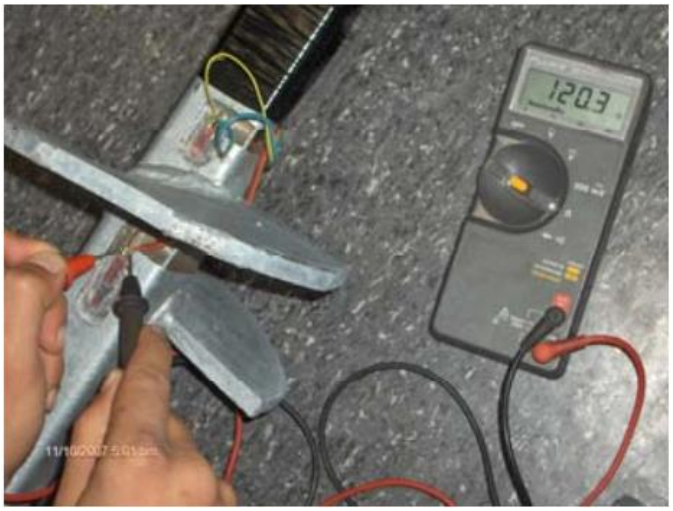

Figure 2.24. Strain gages installed on square shaft helical anchors (Abdelghany and El Naggar 2010)

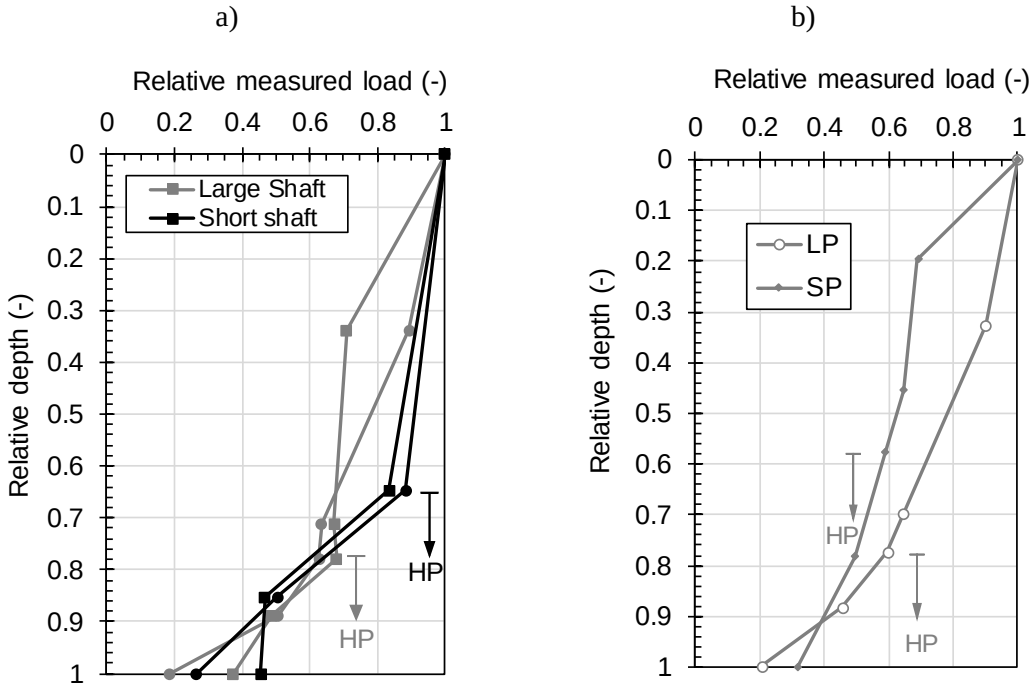

Figure 2.25. Axial load transfer (ALT) measured during field testing in: a) compression (after Zhang 1999, Abdelghany 2008), and b) uplift tension (after Zhang 1999).*HP: Helical Plates

Parametrical studies on helical piles performed by Nagata and Hirata (2005), Spagnoli and Gavin (2016), Papadopoulou et al. (2014) addressed the influence of: i) the helical plate to shaft diameter ratio, ii) number of plates, iii) soil stiffness, iv) soil undrained shear strength, v) and soil friction angle, on the vertical uplift behavior. Results indicate that uplift capacities increased when all these variables increased, being of most influence the plate diameter, soil stiffness, and undrained shear strength. Small changes were observed with the soil friction angle.

Failure Definition

In helical anchors pull-out test, force-displacement curves as the presented in Figure 2.26 are obtained. Common practices for the design of piles under compression have used a limit value of 10% of the pile diameter, which is related with acceptable displacements ranges for onshore applications lower than 1-2 inch (Perko 2009). In the helical anchors' case it would be the plate diameter who mobilizes the soil resistance. Among other interpretation methods on helical anchors exist: a) modified Davisson (ICC-ES 2007), b) Hansen Brinch-Hansen 1963) and c) Decourt (Decourt 1999). The modified Davisson method considers the 10% previous criteria but includes the additional force created by the shaft elongation or compression, so the failure load will be given by the intersection of the elastic displacement line starting from $0.1D$ with the real data. The other two methods, Hansen and Decourt methods, predict the ultimate load which creates a plunging mechanism during loading. These methods calculate the ultimate capacities based on regression analysis from the equations:

Hansen: $$P = \frac{\sqrt{\delta}}{C_1\delta + C_2} \tag{2.14}$$

Decourt: $$P = \frac{C_2\delta}{1 - C_1\delta} \tag{2.15}$$

where δ is the vertical displacement, and C_1 and C_2 are regression constants from the field-testing data. As this research will approach multiple loadings directions it is important to distinguish the

displacement direction, so for vertical pullout loadings displacement is u_z and for lateral load u_x.

Presented in Figure 2.26 are the 3 methods presented showing that for the given data the modified Davisson method predicts an ultimate load of 29 kN while the Hansen and Decourt methods predict loads of 53 and 57 kN, respectively.

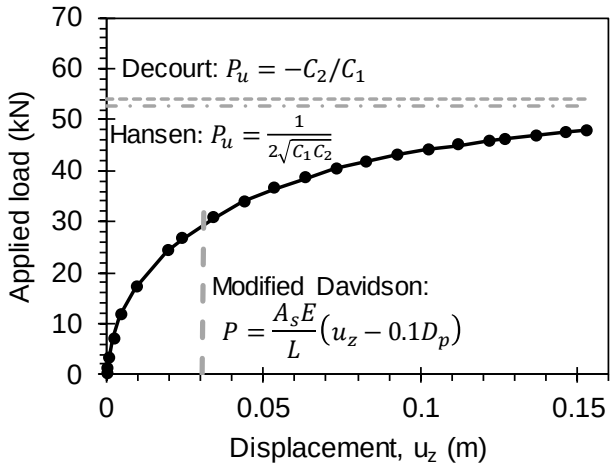

Figure 2.26. Load-displacement curve and capacity prediction methods.

Lutenegger (2008) performed a parametric study with multiple field tests, and found that the ultimate load at 10% of the plate diameter was an adequate normalization parameter for tests at different depths. Similar recommendations for this failure definition have been followed by other authors (e.g., Abdelghany 2008; Perko 2009). It is recognized the need and the advantage of using this normalizer, however, some authors (e.g., Stuedlein and Uzielli 2014, Lanyi-Bennet and Deng 2018) used 5% instead of 10%.

2.2.1.2 Lateral Loading

It is clearly stated by helical anchor manufacturers (e.g. Hubell/CHANCE 2013) that the ideal load conditions that these elements are manufactured for are axial loads where mobilization of the resistance from the plates is desired. Nevertheless, some environmental factors such as

earthquakes, currents, or winds may demand lateral loads on helical anchors, thus an understanding of helical anchors under this loading is important to assess. Soil-Helical anchors interaction under lateral loading presents multiples difficulties due to the complexity of the geometry and the soil response which changes while displaced during loading. In most of the cases, piles subject to lateral loads have been studied using soil-structure interaction theory based on finite differences where the soil is represented by means of springs reacting to the pile loading.

Parametrical studies

Few studies have investigated lateral loading capacity on the helical anchor which must consider both geotechnical and structural (i.e., shaft bending capacity) limits. Lateral capacity has been studied in terms of the number of plates, size, and location of the upper plate (Prasad and Narasimha Rao 1996; Mittal et al. 2010; Al-Baghdadi et al. 2015; Abdrabbo and El Wakil 2016), obtaining results that indicate that when compared to a single or plane pile without helices, helical anchors' geotechnical lateral resistance can be 1.2 to 3 times greater. Al-Baghdadi et al. (2017) also studied the effects of a vertical pullout or compression load on the lateral capacity of helical anchors, being the anchor vertically loaded first and then horizontally. Numerical analyses indicated that when compression loads up to 80% of the vertical capacity are applied, the lateral capacity could increase up to 1.9 times than without vertical load, while at the same amount of pullout load the lateral capacity could reduce this up to 0.85. Another way of gaining lateral capacity was presented by Abdelghany (2008) where the injection grout to the upper shaft section, increases the bending stiffness and the lateral capacity.

Puri et al. (1984) indicated that lateral resistance of HAs is not influenced by the number of plates when they are located at depths greater than three to five times the relative stiffness defined as:

$$T = \left(\frac{EI}{n_h}\right)^{1/5} \tag{2.16}$$

where EI is the pile shaft bending stiffness and n_h is the horizontal soil subgrade reaction, meaning that when helical plates are below the fixity point, they do not contribute to the lateral capacity and is just the shaft the element that works.

Failure definition

The lateral capacity of helical anchors has been estimated based on displacement limits, representing a concern on the superstructure sustained by the helical anchors, rather than the anchor-soil interaction limit states. IBC (2015) recommends the estimation of the lateral load capacity as half of the load that causes a tip lateral displacement of 1 inch (25.4 mm). However, some manufacturers (e.g. Magnum) use to define this capacity as the load present at a half inch, which assumes a linear behavior on the former definition. Some other authors (e.g., Prasad and Narasimha Rao 1996, Chari and Meyerhof 1983) use a criterion of failure when the load-displacement becomes linear with small changes in slope. When combined loading is applied (vertical and horizontal), Al-Baghdadi et al. (2017) used a limit inclination angle criterion of 0.25º for offshore wind jacks while Hubbell/CHANCE (2014) recommends using an angle lower than 15º for onshore structures.

2.2.1.3 Inclined Loading

On the previously presented studies, vertical and lateral behavior of helical anchors has been studied in a separated and independent manner performing numerical, physical, centrifuge, or field-testing analyses. However, few studies have focused on studying a combination of both demands on single helical anchors, which can be the case as in aquaculture farming or marine renewable energy. The behavior of either sallow (footings) or deep (piles) foundations under inclined loads and moments have been classically studied in terms of interaction diagrams (e.g.,

Chari and Meyerhof 1983; Meyerhof and Sastry 1985; Koumoto, et al. 1986; Randolph and Guorvenec 2011) were vertical, lateral, and moments capacities are combined in multiple plots (see Figure 2.27). After Meyerhof's work in the laboratory using rigid piles, it was proposed that the capacity under inclined loads should be determined by an equation of the form:

$$\left(\frac{H}{H_0}\right)^2 + \left(\frac{V}{V_{90}}\right)^2 = 1 \tag{2.17}$$

where H and V are the horizontal and vertical components of the inclined load, and H_0 and V_{90} are the pure lateral and vertical capacities. Numerical simulations (e.g., Lit et al. 2014; Conte et al. 2015) evaluated the validity of the previous solution. Conte et al. (2015) studied flexible reinforced concrete piles under inclined compression loads, defining failure at 5% of the pile diameter, interaction diagrams indicate that the previous theory for rigid piles does not match for flexible. Li et al. performed more than 500 numerical simulations to find a complete interaction diagram of piles under inclined lading in compression, tension and external moments. Displacement controls were used, and failure was defined as the point where the numerical model collapsed. Note that Li et al. did not control the load direction and their main aim was to investigate failure envelopes which are presented in Figure 2.28.

Among the studies of helical anchors under inclined loads there are the reported by Zhang et al. (2009) and Dong and Zheng (2015) were the behavior of rigid helical anchors doing physical scale testing at an inclination of 30 degrees was studied reporting how the stress distribution changes around the plates during the inclined loading. Also, physical testing was also performed by Reape and Naughton (2018) and Sakr et al. (2016) on sands. Reape and Naughton (2018) found that for large shaft diameter helical piles, the plunging inclined load capacity is larger under lateral than during vertical loading, conversely to the results presented by Sakr et al. (2016).

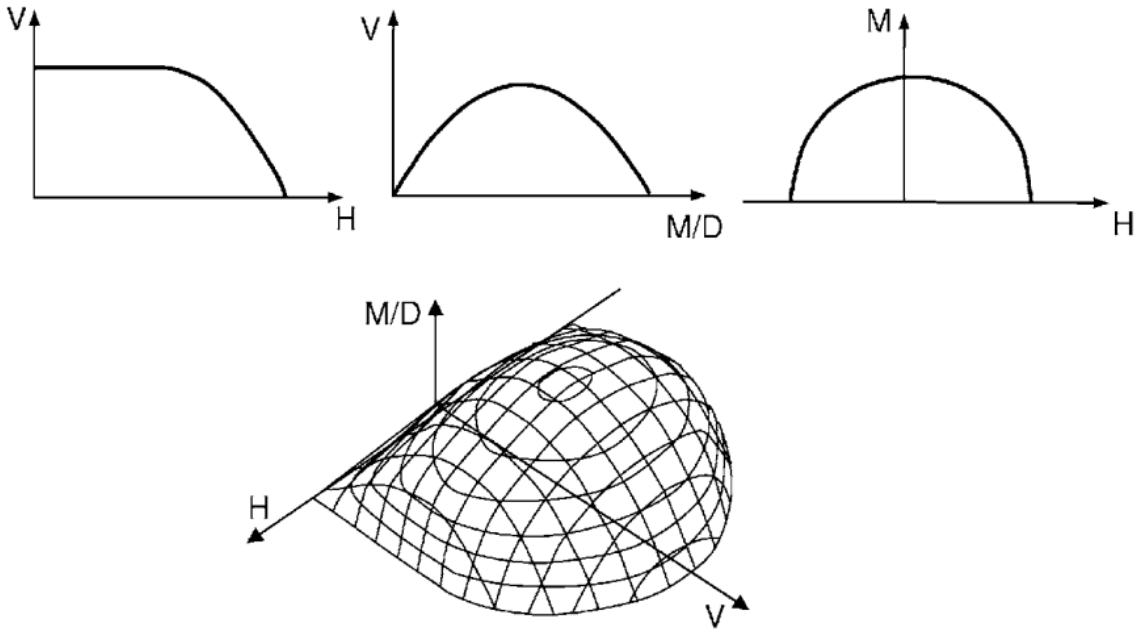

Figure 2.27. Interaction diagrams for inclined loading and moments (Randolph and Gourvenec 2011).

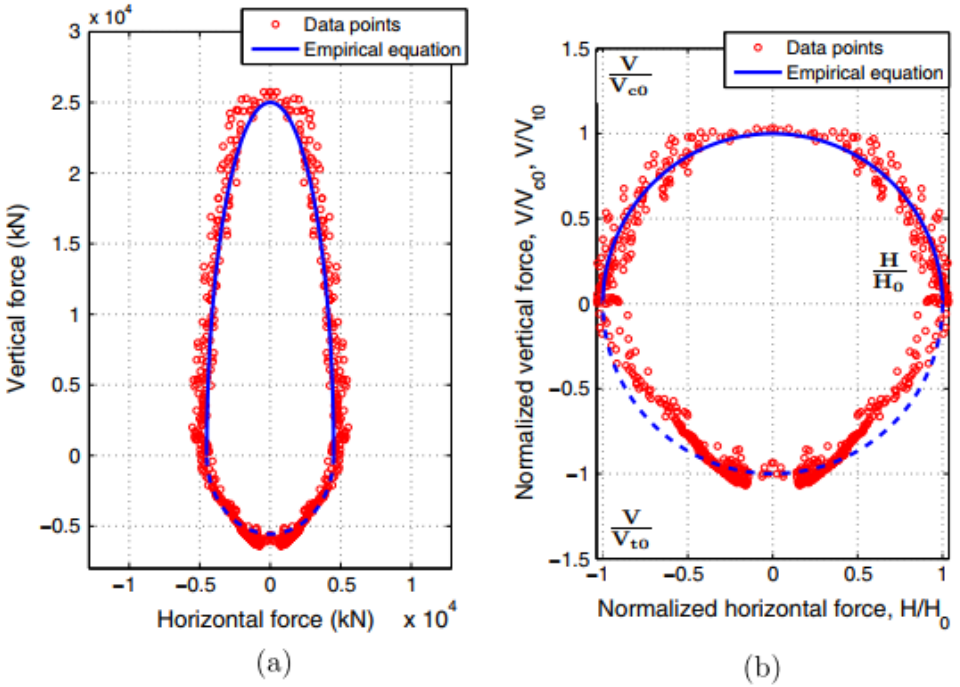

Figure 2.28. Total a), and normalized b) failure envelopes obtained by Li et al. (2014)

2.2.1.4 Cyclic Loading

Among the limitations of the current design procedures of helical anchors it is found that these procedures are based on onshore applications (i.e., wind turbines, communication towers, power poles) (International Code Council 2009; Perko 2009) where recommendations about the dynamic behavior are based on wind or seismic cyclic loading for different return periods. For helical anchors located on open offshore sites, this dynamic behavior in multiple directions is expected most of the time, thus understanding and assessing its behavior under this loading scenario it is demanding. The next paragraphs present a summary of some of the studies aimed to predict the post cyclic behavior of helical anchors under vertical, lateral and inclined loading, where predominantly it is said that the cyclic loads increase the helical anchors resistance.

On the axial load case, Perko (2009) suggests that when cyclic loadings are expected, the ultimate load capacity should be one such the dynamic load stays in a 25% of this, meaning that if a factor of safety of 2 is used, the cyclic load should stay on the 50% of the working load. Narasimha Rao and Prasad (1991) and Prasad and Narasimha Rao (1994a) based on physical testing on soft marine clays found that when cyclic pullout loading is preserved under a 50% of the ultimate load, the capacity increased with a reduction in displacement. This behavior can be explained as a stiffening of the soil during the cyclic loading. Cerato and Victor (2009) also found an increase in the ultimate load capacity after dynamic loading based on field testing, however, high variability in the soil conditions and a non-direct comparison was done in this research to predict that behavior. Abdelghany (2008) reported field testing of helical piles before and after cyclic compression loading in clayey soils. Helical piles were 3.6 and 5.2 m deep ($H/D \approx$12 and 19) and loaded up to 50% of its ultimate capacity, and then subjected to 15 loading cycles changing the loads from 25 to 50% of Pu every 30 min. After this cyclic loading, piles were unloaded and loaded again to obtain the resistance at the same displacements. Results indicate that in the shallower pile, there was not a reduction or increase in the resistance after cyclic loading, and in the deeper pile, there

was a 30% in the capacity. Based on the author's interpretation, such increase is attributed to a contact of the helices with the adjacent soil during this cyclic loading. Grouted helical anchors also reported an increase of their resistance after uplifting cyclic loading; in some cases, this increase was not significant, however, increase in stiffness was observed.

Post anchor behavior after cyclic lateral loading was studied by Prasad and Narasimha Rao (1994b) who presented a laboratory set-up to study the pull-out behavior after lateral cyclic loading on helical anchors. Prasad and Narasimha Rao (1994b) loaded the anchor with cyclic lateral loads up to 70% of the static lateral capacity and 500 cycles. It was found that there is not a reduction in the uplift resistance after this cyclic loading. Lateral deflections of 10% the shaft diameter was obtained, creating a gap in the interface soil-anchor shaft. The presence of this gap and the non-reduction of the ultimate load may indicate the low contribution in resistance by the skin shaft force. Abdelghany (2008) also reported cyclic effects on lateral capacity on grouted helical anchors. Anchors were laterally loaded to 12.5 mm pile head displacement and then loaded with 15 cycles between 50% and 100% of their lateral capacity (defined as the 12.5 mm load). Reported results indicate that grouted piles reduced their capacity between 2 to 5 times after cyclic loading. Authors attribute this behavior with the grouting cracking during cyclic loading.

For cyclic inclined loading, Dong and Zheng (2015) did not find a clear trend on the post cyclic inclined behavior of helical anchors loaded at 30 degrees. Authors compared static test results before and after 10,000 sinusoidal cycles at 5 Hz; finding that depending on the preloading ratio, the capacity could either increase or decrease.

2.2.2 Helical Anchors Installation

Installation of helical anchors onshore has a well-established method. A torsion device to drive the anchor in the soil and a HA with its respective extensions are needed in addition to some other devices. This can be performed using machinery or even human effort for a shallow purpose.

For the installation of helical anchors with machinery, a hydraulic torque motor with capacities of (6000-100000 N-m), a hydraulic machine to drive the motor with a proper alignment and position (e.g. bobcat or excavator), a torque motor connection (drive pin) and helical anchors' extensions are some of the implements needed as shown in Figure 2.29. Some steps for the installation of HA are (Perko, 2009):

1. Attach the HA with the installation motor.
2. Align the HA in the desired location.
3. Applied pressure to insert the sharp end of the HA into the ground.
4. Review how vertical is the anchor.
5. Align the motor with the vertical.
6. Start rotation of the HA
7. Review of vertical alignment.
8. Write down the torque, depth, and number of rotations.
9. Stop when the upper part of the HA is close to the ground to add an extension
10. Check vertical alignment and continue the rotation.
11. Repeat steps 9 and 10 until getting the desired depth or design torque.

Among the advantages found in the installation process are found a short installation time, ability of installation in any weather condition and noise reduction when compared with other pile foundations.

So far helical anchors are not widely used offshore, as there is not a well-established methodology to perform this anchor installation. This factor represents one of the biggest challenges to extent them offshore (Lutenegger 2017, Houlsby 2016). Different consultant companies (e.g., Hafbor n.d., FMS 2018) had proposed different practical solutions to this engineering challenge.

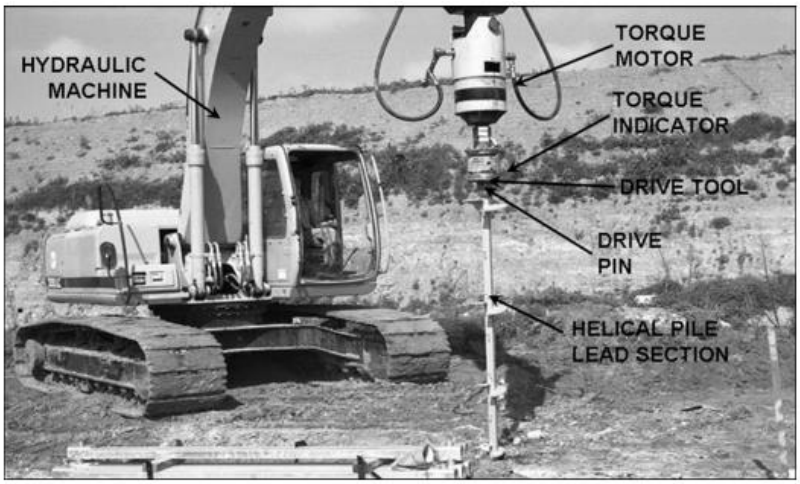

Figure 2.29. Helical anchor installation (Perko 2009).

2.2.2.1 Installation Effects

The influence of installation effects on the behavior of helical anchors has been evaluated in either clay e.g., (Weech and Howie 2012; Lutenegger, Erikson, and Williams, 2014; Bagheri and El Naggar 2015; Fahmy and El Naggar 2017;) or sand (e.g., Agudelo Pérez et al., 2018; Mosquera, Tsuha, Schiavon, and Thorel, 2015; Nagata and Hirata, 2005; Tsuha et al. 2012). In these researches it is recognized that helical anchors installation generates soil disturbance mainly due to two factors: i) shaft displacement and ii) helical plate cutting. The shaft displacement is present during the initial part of the helical anchor installation, where the shaft on the tip of the lead section is pushed into the soil, creating a gap infilled by the anchor while the soil is displaced laterally and dragged downward. Helical plate cutting is present when the helical plates are rotated while advancing in depth spirally as the anchor goes through, displacing it upward, downward, and laterally.

Weech and Howiew (2012), reported field installation effects of grouted-shaft multi-helix helical piles on sensitive soils. Detailed field instrumentation including piezometers and strain gages on the pile shaft allowed the authors to study excess pore water pressure during installation.

Excess pore water pressures radially measured from the pile edge indicates that these extended longer due to the helical plate installation than to the shaft penetration (Figure 2.30a). Weech and Howiew (2012) indicated these excess water pressure extended a distance about 10 to 12 times the plate thickness from the edge of the of the helical plate. Axial load compression test performed at 1 hour, 7 days, and 6 weeks, indicated that the higher the waiting time, the higher the load, as the remolded material was able to re-consolidate (Figure 2.30b). With the obtained load tests and strain gages measurements, the authors back calculated the mobilized shear resistance by the plates and the shaft comparing this with remolded strengths on site. Results indicate that: a) the undrained shear strength around the shaft was fully mobilized, b) around the intermediate plates the strength was partially mobilized, and c) around the bottom plate, the shear strength was equal to the intact strength.

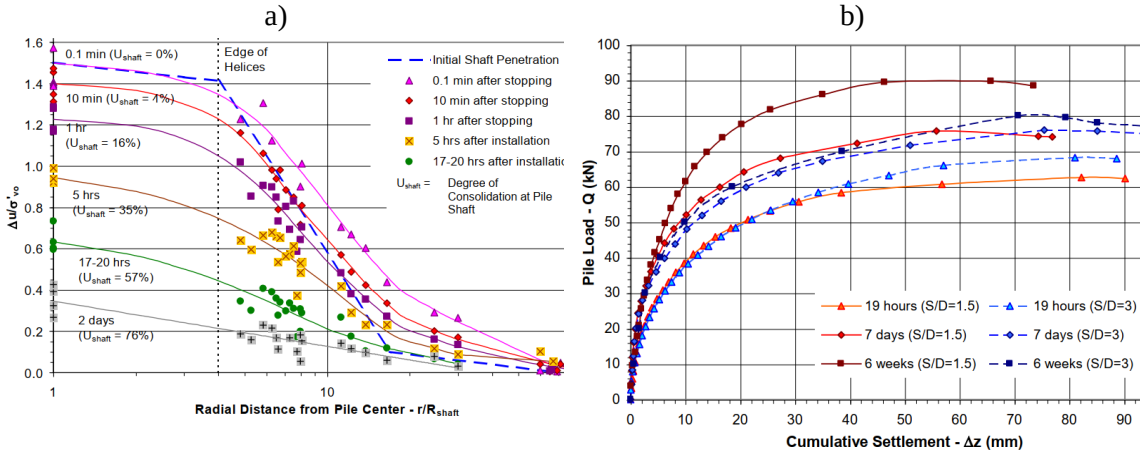

Figure 2.30. Helical anchors installation effects on sensitive soils: a) radial distribution of excess pore water pressure, b) load-settlement curves for multiple recovering times (Weech and Howie 2012)

Based on the previous observations, Bagheri and El Naggar (2015) analyzed a database of helical anchor and piles tested under tension and compression, with strain gages instrumentation in some of them. With the reported maximum load values, the authors also back-calculated undrained shear strengths and proposed a methodology to estimate the capacity helical anchor capacity including the installation effects. This methodology uses the same theory of individual bearing

plates or cylindrical shear failure, previously presented (Section 2.2.1) but modifies the undrained shear resistance values to be used. The authors said that when individual bearing capacity is calculated for all the plates or just the upper plate in the cylindrical shear approach, the undrained shear strength should be calculated using the Skempton's (1951) method as:

$$s_u = s_{up} - 0.5 \times (s_{up} - s_{ur}) \tag{2.18}$$

where s_u is the mobilized shear strength, s_{up} is the peak shear strength, and s_{ur} is the remolded or residual strength. The use of partially residual strength of the previous equation is because, during the plate bearing, the mobilized soil will include intact and remolded resistances. For the cylindrical shear zone, the authors recommend using the soil residual strength. Fahmy and El Naggar (2017), after considering the previous recommendations, studied the numerically the installation effects on large diameter helical piles under tension, compression, and lateral loading on clays with sensitivity equal 3. Results indicated the installation effects were more critical under vertical loading than under lateral loading. For vertical loading, the disturbed soil around the shaft plays a more important role than under lateral loading where the soil mobilizes resistance out of the disturbed zone. Figure 2.31 presents a summary of the obtained results when helical piles were wished in place and when they considered installation effects.

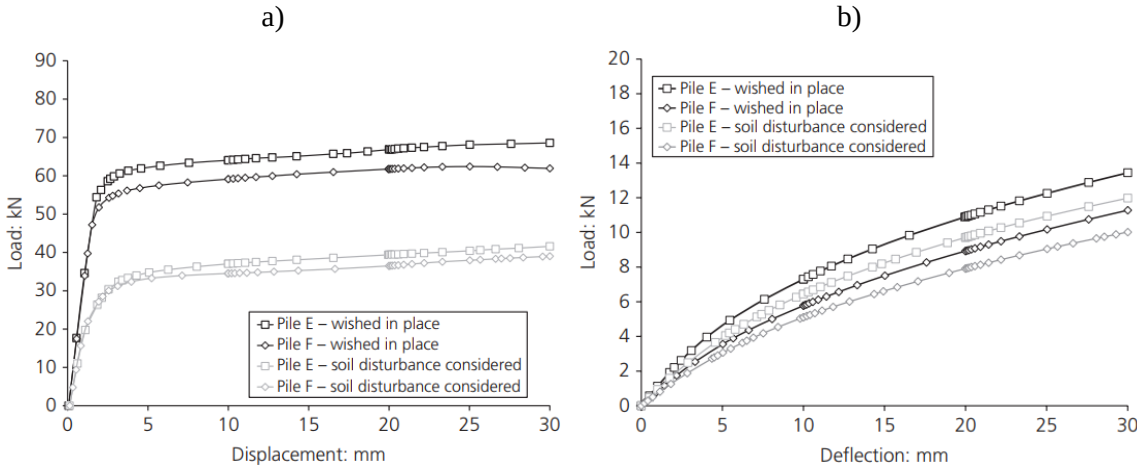

Figure 2.31. Comparison of helical simulated as wished in place and considering soil disturbance under: a) uplift loading and b) lateral loading (Fahmy and El Naggar 2017).

Agudelo Pérez et al. (2017) while studying helical anchor installation disturbance in dense sands by means of centrifuge testing, reported similar observations. Centrifuge testing allowed the determination of disturbance zones called zone 1 and zone 2 (see Figure 2.32). The cited authors performed a back-calculation analysis to determine the disturbed zones ideal parameters with a finite element approach using a MC strain softening model. Results indicated that in the zone 1, the friction angle was equal to the residual parameter and the Young modulus was 0.8 times the one of the undisturbed zone, while in zone 2 these parameters were marginally higher.

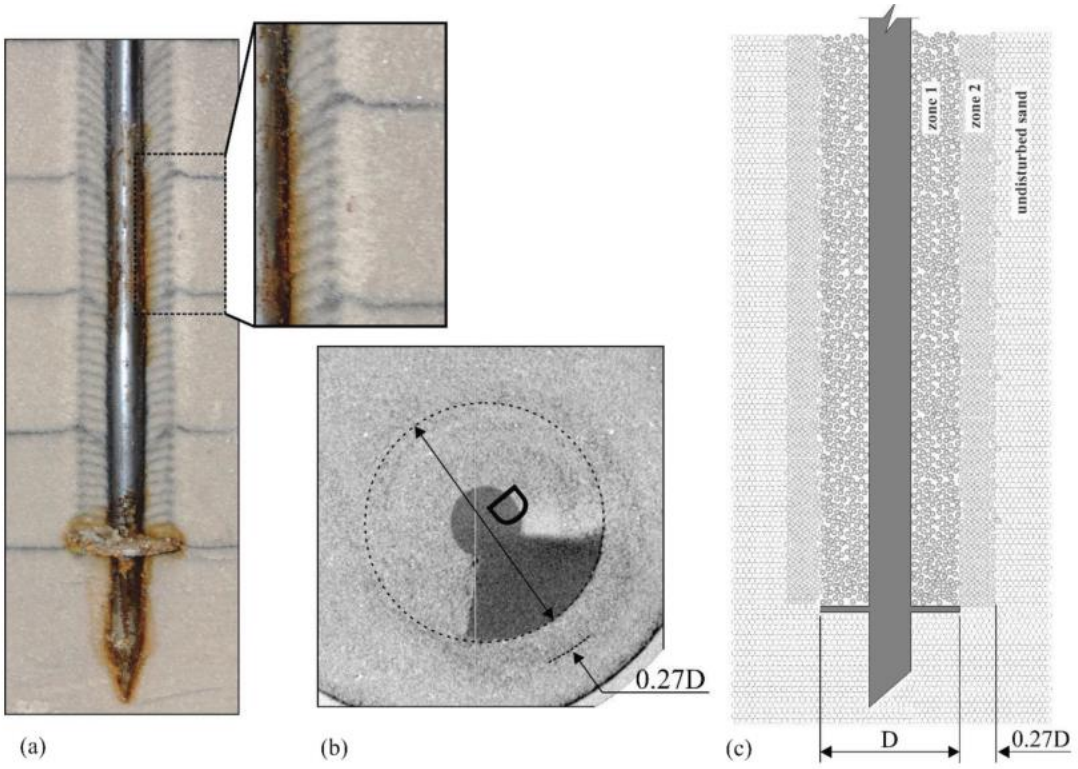

Figure 2.32. Installation disturbance zones in dense sands (Agudelo Pérez et al. 2017)

2.2.3 Helical Anchors and Aquaculture Industry

To verify if the aquaculture loads introduced in the previous Aquaculture Background section can be hold by helical anchors, Figure 2.33 presents a compilation of 140 pull-out tests presented by Perko (2009) for multiple anchor depths and number of plates in different soils. An increase in the pullout resistance is obtained when the plate diameter increases. Comparing this

figure with Figure 2.19, this anchoring technology represents a feasible solution to this sector with typically used anchor geometries. However, further studies are needed and addressed in this research to understand helical anchors behavior under specific aquaculture loading conditions.

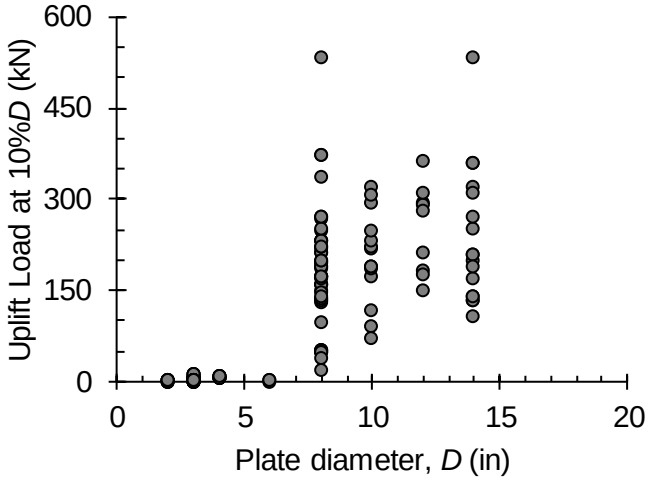

Figure 2.33. Ultimate load vs plate diameter (after Perko 2009)

.

3 NUMERICAL ANALYSIS OF HELICAL ANCHORS

The main purpose of this chapter is to study the helical anchors bearing capacity under inclined loading using 3D finite element analyses. To achieve this goal, different helical anchors geometries in different soil conditions were analyzed to:

- Validate the finite element model with previously published results for vertical pullout.
- Investigate the pure horizontal capacity of helical anchors, with specific attention given to the influence of shaft rigidity, soil strength, soil stiffness, and depth of the upper helical plate.
- Understand the effect of the helical plate for lateral loading conditions.
- Study how the capacity or ultimate line load is influenced by the inclination angle.
- Investigate the interaction between the mobilized uplift resistance generated by the plate and the lateral resistance generated along the shaft under inclined loading scenarios.
- Explore the optimum inclination loading angle and how this is influenced by shaft rigidity, soil strength, soil stiffness, and depth of the upper helical plate.

This chapter is subdivided into eight subsections where the model setup is presented initially, followed by a failure definition, and an explanation of the loading procedure. After this, a description of the helical anchors analyzed is presented, followed by the results of a parametric study for vertical, lateral and inclined loading. The chapter concludes with a summary of the analyses and findings.

3.1 3D Finite Element Model Setup

This section presents a detailed explanation of the 3D finite element model setup, presenting the elements studied, the model space, calculation procedure, constitutive model, and model limitations. Helical anchors are a foundation type with geometry that consists of a helical plate element(s) installed at depth that are attached to a vertical shaft that extends to the ground

surface. When helical anchors are loaded vertically, symmetry of the system may be simulated with a 2D axisymmetric model. However, when helical anchors are subjected to horizontal or inclined loads a 3D analysis may be used to capture the non-uniform soil resistance mobilized along the plate(s) and shaft.

3.1.1 Element Types and Purpose

Numerical simulations of helical anchors were performed by Merifield (2011) and Wang et al. (2013) using 2D axisymmetric conditions for vertical loading without consideration of shaft geometry and material properties (i.e. rigid plate). Further research was performed by multiple authors using 3D finite element modeling for vertical and lateral loading with and without consideration of the helical shape (pitch) (e.g., Kurian and Shah 2009, Al-Baghdadi et al. 2015, Al-Baghdadi et al. 2017, George et al. 2017). Kurian and Shah (2009) and George et al. (2017) concluded the influence of the helical pitch produces an increase in vertical capacity of at least 9% when compared with a flat plate. However, during those non-symmetrical models, helical anchors experienced rotations or non-uniform movements during pullout on the horizontal direction that later had to be constrained. Such constrain could lead to such increase when compared with the flat plate. Al-Baghdadi et al. (2017) stated the inclusion of the helical pitch generates small increases in vertical and lateral capacity of 5% and 1%, respectively. Computed results from these studies suggest the helical pitch has a limited influence on vertical and lateral geotechnical capacity, and do not consider installation effects associated with soil disturbance, which are likely more influential.

The procedure suggested by Al-Baghdadi et al. (2017) for model geometry was adopted to simulate helical anchors with solid and hollow shafts. For convenient processing of structural forces in the shaft, a beam element was included through the center of volume elements that are surrounded by shell elements to simulate the 3D shaft geometry and connection of the helical plate.

While structural loads may be resolved from the volume or shell elements in Plaxis 3D (Figure 3.1), it is computationally more expensive and inconvenient to process computed results. Significantly more elements (greater than 400,000 vs. 180,000 with a beam element) are required to converge to the same solution as simple beam elements. The model geometry for helical anchors is illustrated in Figure 3.1, whose element types and purposes are presented in the next paragraphs and summarized in in Table 3.1.

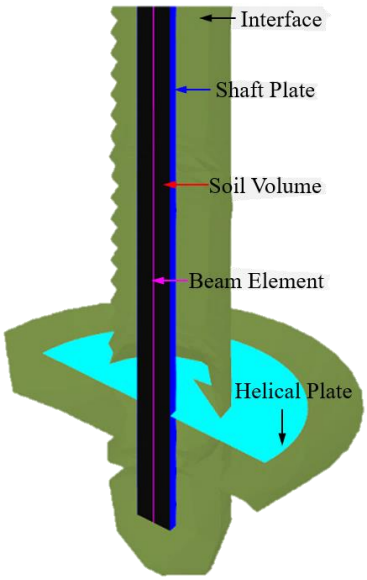

Figure 3.1. Helical anchor modeling features

- **"Soil" Volume Elements**: Following recommendations from Brinkgreve et al. (2017), this 3D volume element was chosen to simulate the bending stiffness of the shaft. Soil volumes are 10 node tetrahedral elements with 4 stress integration points. A non-porous linear elastic material was selected with stiffness and moment of inertia properties that generate an equivalent bending stiffness to the helical anchors being modeled:

$$E_{SV}I_{SV} = E_{HA}I_{HA} \tag{3.1}$$

where $E_{SV}I_{SV}$ and $E_{HA}I_{HA}$ represents the bending stiffness of the soil volume and helical anchor, respectively. Helical anchors were simulated in the same manner for square shafts.

- **Shaft Plate:** Shell elements surrounding the soil volume elements were simulated with a low equivalent bending stiffness, 1×10^{-6} less than the soil volume element, for convenient connection of the helical plate elements in Plaxis 3D, application of interface elements, and shaft geometry. This element is composed of 6-node triangular plate elements with 6 degrees of freedom, three translational and three rotational according to Mindlin's theory (Bathe 2014). Note that for hollow helical anchors this element is enough to obtain force-displacement curves as it represents real geometry and mobilization of geotechnical resistance. While it is possible to use only shell elements for the shaft, extracting structural loads is less convenient than the beam element through the center of the shaft. Figure 3.2 compares vertical and lateral force-displacement plots obtained using only soil volume elements and a plate element with actual stiffness and geometric properties to demonstrate that computed results in each case are equivalent. Soil structure interaction is simulated with an exterior interface on the shell elements.

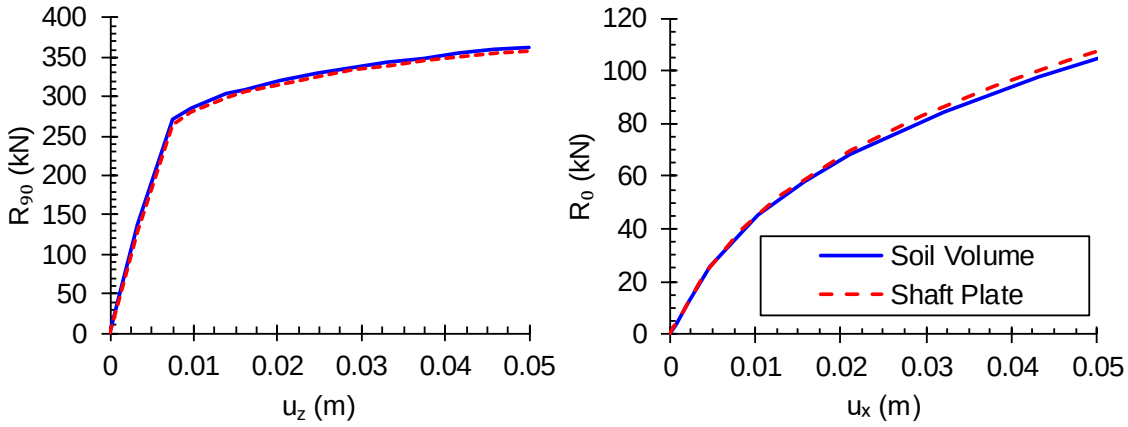

Figure 3.2. Force-displacement plots for hollow shafts helical anchors simulated using soil volume and shaft plate elements for: a) vertical uplift, b) lateral loading.

- **Helical Plate:** Helical plates were simulated as planar with the understanding that differences in capacity are small when the helical pitch is considered, as previously discussed. The actual steel properties and thicknesses were assigned to helical plates. The same 6-node element used for the shaft in this case. An exterior interface was applied to the surface.

- **Beam element:** This structural element type was introduced in the center of the soil volume element to conveniently process structural forces, such as axial load transfer and bending moment along the shaft. After meshing, a 3-node beam element with six degrees of freedom, three translational and three rotational, were used. The beam behaves according to Mindlin's theory (Bathe 2014). Linear elastic material properties were selected such that the equivalent bending stiffness is 1×10^{-6} less than the soil volume element. Note that the soil volume could also be used to extract structural forces from the element, however, the internal algorithm of this element makes an approximation of the bending stiffness dependent on the number of elements and is thus less convenient and computationally more expensive.
- **Interface:** Interface elements were used to simulate soil-structure interaction and to allow soil-anchor separation (i.e. the breakaway condition). Thus, when the anchor is subjected to pullout and/or lateral loads, the lower part of the plate or unloaded side of the shaft will not unrealistically compute excessive suction (i.e. tension) on the shaft or plates. These are 12-node elements with 6 pairs of nodes and no thickness. The interface parameters were selected to be equal to the surrounding soil with assuming a drained condition (effective stress parameters) to allow breakaway at this location and to prevent the soil from applying tension to the helical anchor.

Table 3.1. Elements parameters to simulate Helical Anchors

Element			**Soil Volume**	**Shaft Plate**	**Beam**	**Helical Plates**	**Interface**
Purpose			Simulate rigid elements inside the soil	Simulate shaft behavior and connect helical plates	Extract structural forces from the element	Simulate helical plate as planar element	Allow separation between soil and anchor
General							
Material Model			Linear Elastic	Linear Elastic	Linear Elastic	Linear Elastic	Elasto-Plastic
Drainage Type			Non-porous	-	-	-	Drained
Unit weight	γ_{sat}	kN/m^3	γ_{eq}	$\gamma_{eq} \cdot 10^{-3}$	$\gamma_{eq} \cdot 10^{-3}$	78	-
Parameters							
Young's Modulus	E	kN/m^2	E_{eq}	$E_{eq} \cdot 10^{-6}$	$E_{eq} \cdot 10^{-6}$	$200 \cdot 10^{-6}$	Surrounded soil
Possion's ratio	ν'	-	0.33	0.33	-	0.33	Surrounded soil

3.1.2 Modeling Space

Helical anchors subjected to lateral or inclined loading requires a 3D modeling technique. Symmetry of the helical anchors was taken advantage of by modeling half of the helical anchor. A summary of the model geometry is presented in Figure 3.3, where X represents the in-plane horizontal dimension in the direction of lateral loading through the center of the anchor, Y is the out-of-plane dimension, and Z is the total depth of the model space. Note that half cylindrical zone around the helical anchor denoted by D' and L', where $D' = 2D$ and $L' = 1.125L$, was set to refine the mesh around the helical anchor.

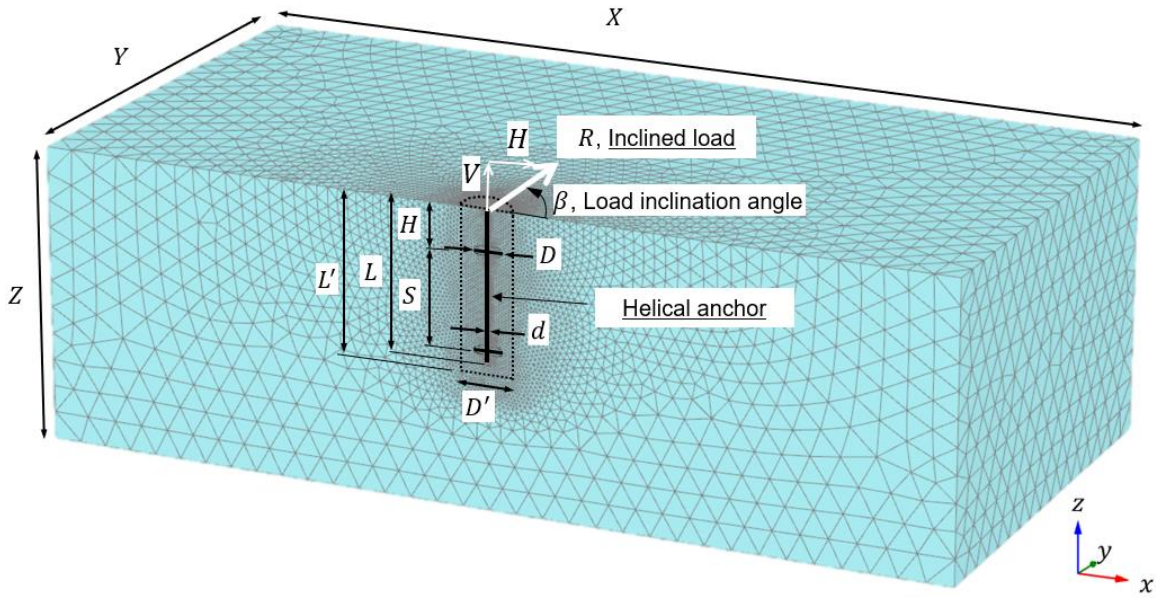

Figure 3.3. Three-dimensional finite element model dimensions and helical anchor and loading notation.

Modeling of piles or helical anchors under compression, uplift tension or lateral loading requires the model space to be sufficiently large such that boundary effects are limited. For helical anchors, finding a space normalizer (e.g., total length, helical plate diameter, shaft diameter) can be difficult, as it depends on the loading direction and relative dimensions of the shaft length and plate diameter. A summary of the normalized space dimensions used in the literature to model helical anchors or piles under compression (C), uplift tension (T), lateral (L), or inclined (I) loading

is presented in Figure 3.4. The summarized studies were performed using 3D finite element analysis, for different loading directions at different times, e.g., studies with multiple loading directions had not followed each other but started from initial equilibrium conditions. Normalized dimensions for X are between 20 to $80D$, Y ranges are typically half of the X dimension, and Z ranges between 0.5 to $2.5L$, with mean values between 1.5 to $2.0L$.

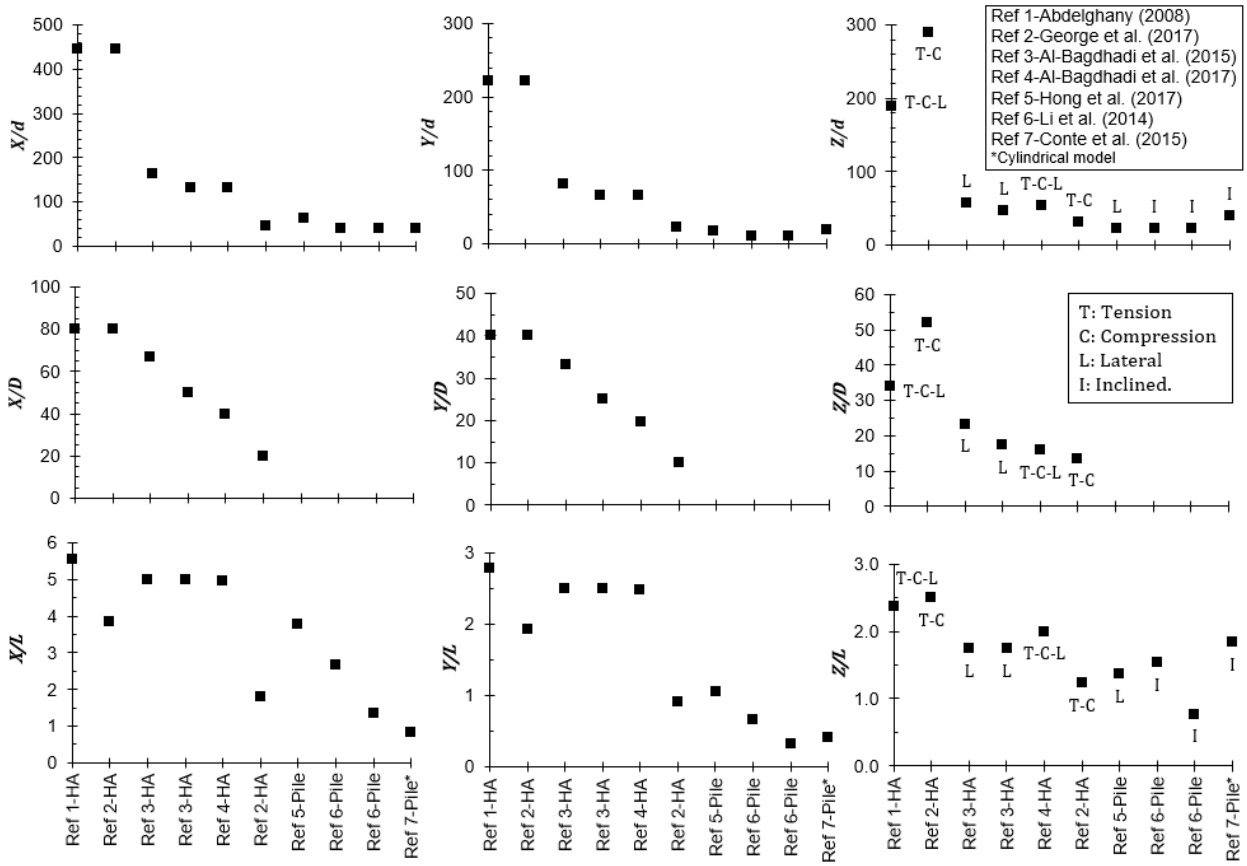

Figure 3.4. Normalized model dimensions used during 3D finite element modeling of helical anchors (HAs) or piles.

3.1.3 Mesh Independence Study

To avoid subjectivity on the determination of model dimensions, a mesh independence study (MIS) was performed, where the dependence between the number of elements and the computed response (e.g., predicted resistance) was analyzed. Two MIS were performed for models

with $X = 30D$ and $20D$, and $Z = 2L$ considering the minimum dimensions on Figure 3.4. A comparison of the obtained maximum vertical uplift and horizontal load for these model spaces with the number of elements is presented in Figure 3.5. The model dimensions influence the computed response for a similar number of elements. In this study a model of a least 180,000 elements, and dimensions $X = 20D$, $Y = 10D$, and $Z = 2L$ was used.

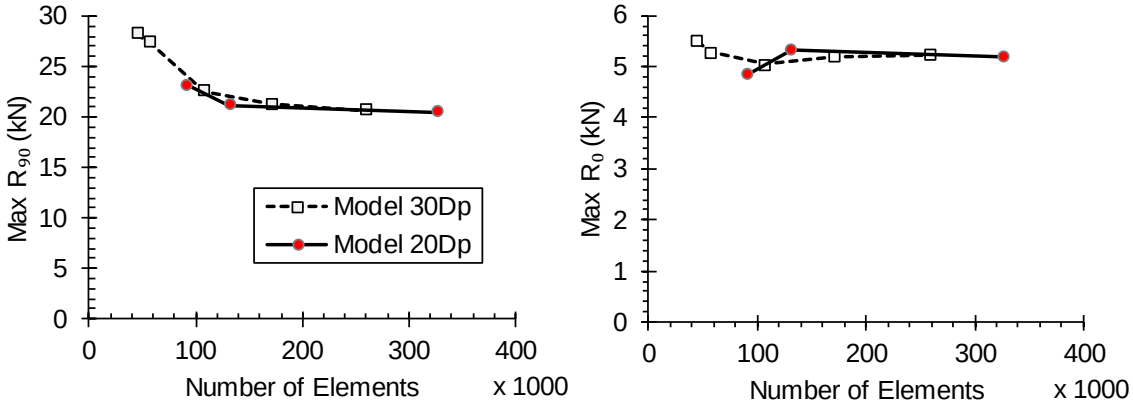

Figure 3.5. Mesh independence study for different model space dimensions: a) vertical uplift, b) lateral loading.

3.1.4 Calculation Procedure (Eulerian vs. Lagrangian Approach-Updated Mesh).

Typical finite element analyses for onshore foundations or excavations consider small deformations to define failure based on serviceability limits. For this kind of behavior, small deformations are solved for an initial constant volume, and conventional Eulerian finite element formulations are justified. For other applications where large deformations are anticipated, such as reinforced embankments (e.g., with geosynthetics) or offshore applications, especially for failure conditions examined here, Lagrangian approaches are typically adopted. PLAXIS 3D 2018 defines three key factors included in a Lagrangian Formulation, which are: i) inclusion of additional terms to the structure matrix to simulate large distortions, ii) inclusion of stress changes due to finite rotations, thus a stress rate term that includes rotation rate relationships is included in the formulation, and iii) an update of the finite element mesh, so the next deformation step will be

performed based on the current nodes locations instead of the initial condition.

Lagrangian approaches follow all the particles of the body in motion, from the beginning to the end, integrating the stiffness matrix at time $t + \Delta t$. In this formulation, large distortions are included using Green-Lagrange Strains while stress rate changes are included using Second Piola-Kirchhoff stresses. Further details of this mathematical approach are presented in Bathe (2014).

In Plaxis 2018, the Lagrangian Formulation is available by activating the updated mesh option and was adopted in this study. An example of the differences between the computed results with and without an updated mesh are presented in Figure 3.6. Small differences are observed for vertical loading. For inclined and lateral loading, the results begin to diverge at larger deformations. Therefore, interpreted capacities from numerical simulations are dependent on the failure criteria adopted. As large displacements under failure conditions are expected for lateral and inclined loading, an updated mesh analysis was performed. A drawback of this analysis is that changes in pore water pressure at the stress points are not updated.

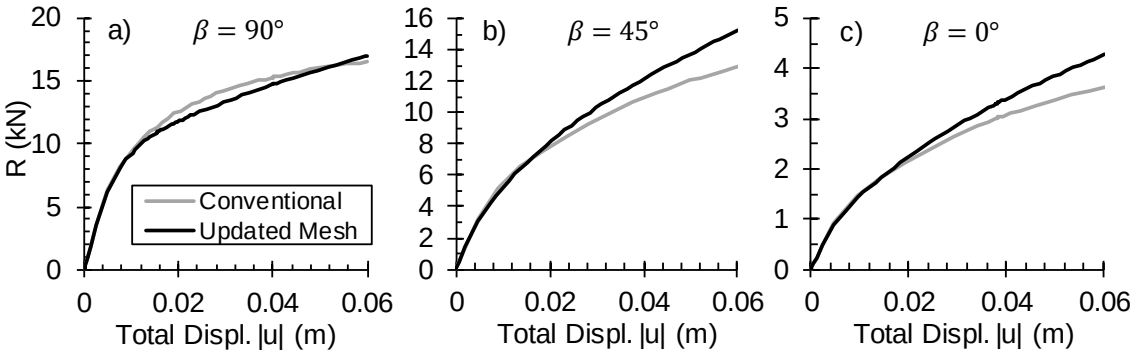

Figure 3.6. Conventional (Eulerian) analysis vs. Update Mesh Analysis (Lagrangian) during: a) vertical uplift, b) inclined 45°, and c) lateral loading.

3.1.5 Constitutive Model

An elastic perfectly plastic constitutive soil model with Tresca yielding criteria was used for the numerical simulations presented in this chapter. This model was chosen due to its simplicity,

reduced computational expense, and ability to capture yielding around the anchor, including interaction between the shaft and plates. The limitation of this model is its inability to capture stiffness degradation associated with mobilization of shear strength. Therefore, interpreted lateral pullout and vertical anchor capacities, which are dependent on deformations, are partially dependent on the simulated elastic stiffness. A parametric study is performed in this chapter to evaluate the sensitivity of the associated stiffness at yielding with interpreted capacities. Additionally, peak strength that manifests at small deformations that may occur in sensitive clays are not simulated directly. Therefore, mobilized shear strength is implicitly assumed to be that which occurs at strain levels associated with deformation-based failure criteria of the anchor (discussed in the following section). Nevertheless, this constitutive model is adequate to compare the computed capacities during inclined loading and to achieve the objectives of these numerical analyses.

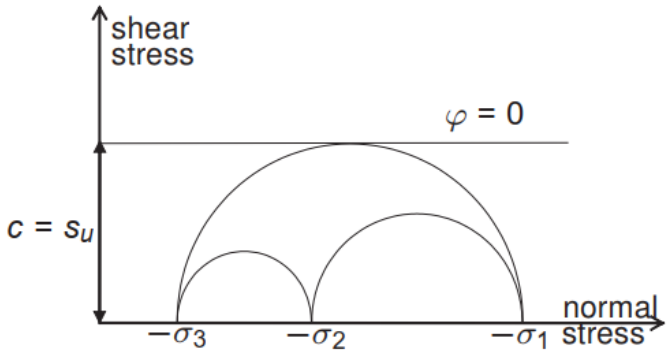

Figure 3.7. Tresca failure criterion.

3.1.6 Modeling Limitations

For the given modeling conditions, some limitations must be acknowledged. During the loading process, movement of the anchor head could modify the load inclination angle, though this movement is assumed negligible as it is dictated largely by the water depth and line length rather than anchor head displacements. Direct installation effects were not considered with regards to

disturbance of soil that is cut by the plates and displaced by the shaft. Weech and Howie (2012) and Bagheri and El Naggar (2015) showed that such effects are more influential in sensitive soils, and that reduction of the undrained shear strength to its residual value is reasonable. Thus, if the analyzed undrained shear strength is assumed to be residual, installation effects will be somehow accounted for. Pore water dissipation after installation was not accounted which can lead to some underprediction of the total capacity (Weech and Howie 2012). Immediate breakaway or separation at the anchor-soil interface under perpendicular tension loads was simulated, although in reality partial suction from this cohesive material may be present during the early stages of loading. This partial suction may increase the total resistance at small displacement, that the soil model may compensate with a constant modulus. However, such effects are not computed as failure is anticipated at large deformations.

3.2 Failure Definition

Helical anchors vertical failure mechanisms presented in Chapter 2 can form shallow or deep, with cylindrical or individual plate bearing failures when sufficiently deep, as illustrated in Figure 3.8. Helical anchors failure definition under vertical loading was considered from multiple studies where there is a general consensus that vertical displacement of 10% of the plate diameter is assumed a geotechnical failure (e.g., Lutenegger 2008; Abdelghany 2008; Perko 2009; Stuedlein and Uzielli 2014). This definition comes from the Helical anchors "analogous" foundations (i.e., piles), which assumes the ultimate soil resistance at the pile tip under compression is achieved at this displacement level. Other methods, e.g., Hansen and Decourt's, define vertical capacity as the "plunging" or yielding load from where excessive settlements proceed after a small load increment. These often coincide in soft clays. Perko (2009) discusses how Hansen and Decourt methods could predict an ultimate load that has not been reached during testing, so application of such methods could lead to overestimates of the actual resistance and 10% of the plate diameter is adopted in this study.

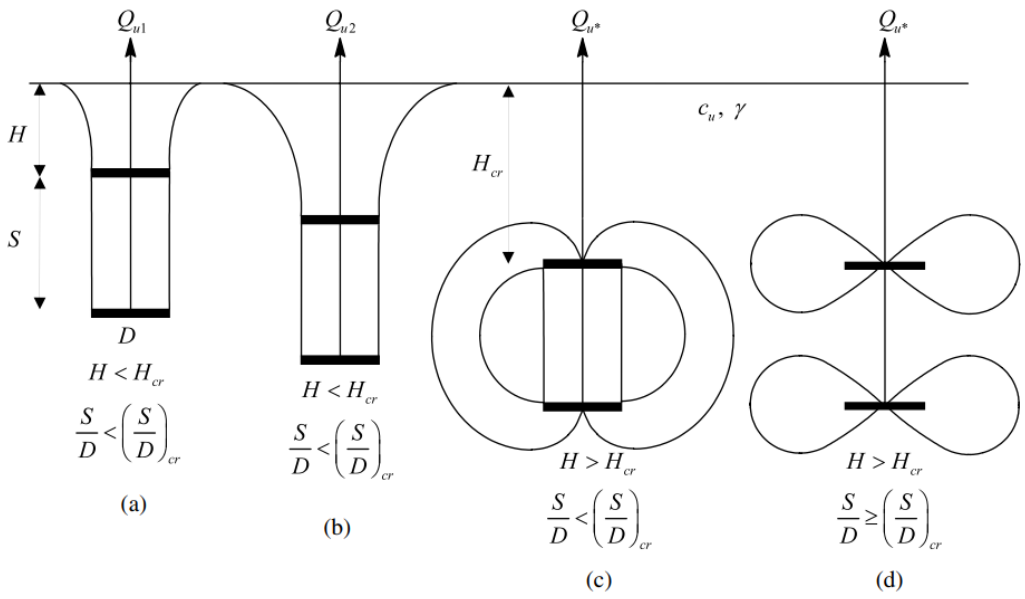

Figure 3.8. Helical anchors failure mechanism: a) shallow failure, b) deep cylindrical shear failure, c) deep cylindrical shear failure, d) deep individual plate bearing (from Merrifield 2011).

Lateral capacity of piles is often based on a serviceability limit state approach rather than ultimate geotechnical or structural resistance for "long" piles. IBC (2015) defines lateral capacity as half of the load that displaces the pile head 25 mm. For helical piles, Al-Baqhdadi et al. (2017) analyzed offshore jackup structures with two serviceability approaches: i) lateral displacement of 10% of the plate diameter or ii) 0.25 degrees rotation at the pile head, following design recommendation for offshore wind structures (to prevent structural failure of the shaft/pile). In some cases, soil failure for a pile or helical anchor under lateral loading is defined as the load where a constant slope is obtained in the force-displacement curve (e.g., Prasad and Narasimha Rao 1996; Sakr et al. 2016; Singh and Bhardwaj 2015) (Figure 3.9). However, this curve could have a positive slope, meaning that the system can sustain more load as there is only partial yielding of the soil. For individual helical anchors placed offshore for mooring purposes, movement of the anchor head itself is not a concern from a serviceability perspective, and structural limits are more relevant to define failure. Broms (1964) criterion for piles defines the failure load as that which results in development of a plastic hinge on the pile, meaning that the pile itself yields due to bending from

applied load at the anchor head. Summarized in Figure 3.9 are the failure criteria discussed. It may be observed that lateral capacity obtained with Broms (1964) criterion is higher than the others discussed because the system relies on the structural resistance of the anchor rather than yielding of the soil. Although soil may yield at depth along the shaft, there may be enough structural resistance to continue loading (Figure 3.9). Soil strength will continue to be mobilized in extension at depth along the shaft until the structure itself (i.e. shaft) yields and develops a plastic hinge. Post yielding conditions or nonlinear moment-curvature relationships are not used in this research.

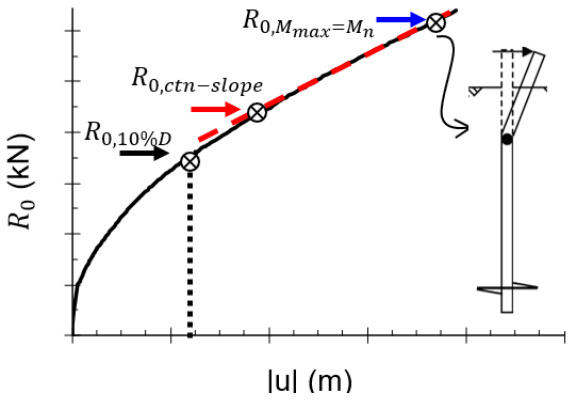

Figure 3.9. Lateral loading failure definition.

Sakr et al. (2016) and Reape and Naughton (2018) studied inclined loading of helical anchors using physical and centrifuge testing in sands, respectively. Sakr et al. (2016) used the geotechnical failure criterion for inclined loading where there is constant slope in the load-deformation behavior, where maximum and minimum "capacities" were obtained under vertical and lateral loading, respectively. Reape and Naughton (2018) used rigid shaft helical anchors without consideration of structural resistance and defined failure as the plunging or peak load in a force-displacement plot, resulting in the opposite conclusion. Figure 3.10 presents a summary of such results, where it can be seen how the inclined capacities are optimized using rigid helical anchor shafts, however, and as it is most often the case, helical anchor shafts behave as flexible or "long" piles. In this study a combined failure criterion was adopted, where the anchor will fail

either: i) structurally due to combined bending and axial loads imposed or ii) geotechnically, meaning that the anchor will have sufficient vertical movement (10% of the plate diameter) to mobilize geotechnical resistance around the plate under inclined loading (e.g., Lutenegger 2008; Abdelghany 2008; Perko 2009; Stuedlein and Uzielli 2014). Note that for combined loading the structural capacity should be determined as:

$$\frac{P_a}{P_n} + \frac{M}{M_n} < 1 \tag{3.2}$$

where P_a and M represent the axial load moment in the shaft and P_n and M_n are the nominal axial and moment capacities. However, it is noted that the axial demand typically constitutes less than 1% of the ultimate structural capacity under combined loading and bending largely controls.

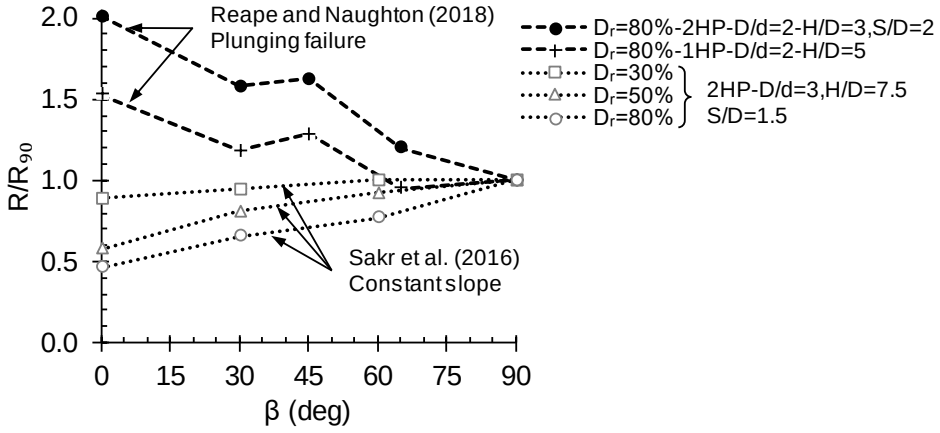

Figure 3.10. Differences of distribution of inclined loading capacities based on plunging failures and displacement or geotechnical constant slope limits.

3.3 Simulated Loading Procedure

With the proposed failure criteria, two loading procedures were followed: i) displacement control for vertical and lateral loading, and ii) force control for inclined loading to maintain a constant load inclination. Displacement-control is computationally more efficient for the simple vertical and lateral loading scenarios. For vertical loading 10% of the plate diameter was achieved.

For lateral loading, incremental displacements were imposed at 0.1D, 1d and 2d. If a plastic hinge did not develop after displacing two shaft diameters (i.e. $M_{max} = M_n$), an extrapolation of the displacement required to develop a plastic hinge was made, which appears reasonable based on linear-load deformation response at larger deformations (e.g. Figure 3.9). The load was also extrapolated from the load-displacement curve at the anchor head. Because the moment distribution is only obtained at the end of each load increment, discrete maximum moment vs. displacement curves were obtained

Force control will proceed during inclined loading to ensure that the mooring load inclination angle is constant, as expected for aquaculture loading scenarios. This force control was performed incrementally and once either the structural or geotechnical limit was reached, loading was discontinued.

3.4 Parametric Study of Helical Anchors.

The purpose of this section is to present the helical anchors analyzed to study their bearing capacity under inclined loading. A summary of their geometric properties, soil parameters, and shaft rigidity is presented in Table 3.2. Shaft rigidity depends on soil and anchor parameters and defines if under lateral loads the anchor is flexible and will bend or if is rigid and will rotate. HA1 and HA7 are anchor geometries already employed by some aquaculture farmers in Maine where low mooring loads (less than 20 kN) are expected. Mean soil properties considered have an undrained shear strength of 25 kPa and an $E/s_u = 500$. After initially exploring these two anchors placed in the mean soil properties, variations in plate depth, soil strength and stiffness were performed to gain greater insight into the generalized behavior of helical anchors under inclined loading.

As previously mentioned, anchors were simulated with a circular shaft, even if they were square, to avoid edge effects or stress concentrations at the shaft edges. A modification of the

bending properties was necessary to accommodate this simulation procedure. Table 3.3 presents the equivalent section properties of the anchors studied herein.

Table 3.2. Geometric properties and soil parameters of helical anchors analyzed

		Anchor Definition								Soil Parameters			Shaft Rigidity	
	Anchor ID	D (m)	d (m)	S (m)	H (m)	L (m)	H/D (-)	S/D (-)	L^* (m)	s_u (kPa)	E (MPa)	E/s_u (-)	$T=EI_p/E_sL^{*4}$	Type
1 Plate Helical Anchor	HA1	0.254	0.038	0	0.69	0.8	2.7	0.0	0.69	25	12.5	500	0.0124	Semi-rigid
	HA2	0.254	0.038	0	1.09	1.2	4.3	0.0	1.09	25	12.5	500	0.0020	Flexible
	HA3	0.254	0.038	0	1.49	1.6	5.9	0.0	1.49	25	12.5	500	0.0006	Flexible
	HA4	0.254	0.038	0	2.21	2.3	8.7	0.0	2.21	25	12.5	500	0.0001	Flexible
	HA5	0.254	0.038	0	2.97	3.1	11.7	0.0	2.97	25	12.5	500	0.00004	Flexible
2 Plates Helical Anchor	HA6	0.254	0.038	1.1	0.44	1.6	1.7	4.2	1.49	25	12.5	500	0.0006	Flexible
	HA7	0.254	0.038	0.8	0.69	1.6	2.7	3.1	1.49	25	12.5	500	0.0006	Flexible
	HA8	0.254	0.038	0.4	1.07	1.6	4.2	1.6	1.49	25	12.5	500	0.0006	Flexible
	HA9	0.254	0.038	0.8	0.69	1.6	2.7	3.1	1.49	25	2.5	100	0.0029	Semi-rigid
	HA10	0.254	0.038	0.8	0.69	1.6	2.7	3.1	1.49	25	25	1000	0.0003	Flexible
	HA11	0.254	0.038	0.8	0.69	1.6	2.7	3.1	1.49	50	25	500	0.0003	Flexible
	HA12	0.254	0.038	0.8	0.69	1.6	2.7	3.1	1.49	100	50	500	0.0001	Flexible

Note: L* is defined as the depth to the lower plate, when one-plate HA, L* = H. T equation proposed Poulos and Hull (1989) defines rigid (T>0.208) and flexible piles (T<0.0025).

Table 3.3. Real square and equivalent circular properties of the helical anchor simulated.

Property	Symbol	units	Square	Circular
Diameter/side	d	(m)	0.038	0.038
Cross sectional area	a	(m^2)	0.00144	0.00113
Inertia	I	(m^4)	1.76E-07	1.02E-07
Section modulus	Z_{real}	(m^3)	9.242E-06	
Section modulus after corrotion	Z^*	(m^3)	8.700E-06	
Yield stress	F_y	(MPa)	385	385
Youngs modulus	E	(GPa)	200	343
Nominal moment	$M_n = M_y$	(kN m)	3.35	3.35
Bending stiffness	EI	(kN m^2)	35.1	35.1

Property		units	Value
Helical Plate thickness	t	(m)	0.01
Helical Plate diameter	D	(m)	0.0254

3.5 Vertical Uplift Loading Results

The objectives of this section are to validate the accuracy of the finite element model predicting capacities of helical anchors subject to vertical uplift loading, and to introduce the differences in capacities predicted when soil and anchor properties are modified. This latter result will be helpful in the following sections when results of vertical and lateral loading are integrated together predicting inclined loading capacities. Table 3.4 summarizes the vertical uplift capacities whose load-displacement plots are presented in Figure 3.11. In summary, the uplift capacity increases: i) as the plate depth increases (e.g., HA1 to HA5), ii) as the undrained shear strength increases (e.g., HA7, HA11 and HA12), iii) as the soil stiffness increases (e.g., HA9, HA7, HA10), and iv) as the plate spacing S/D approaches the optimum value of three recommended by Merifield (2011) (e.g., HA6, HA7, and HA12). Note in this last conclusion that HA6 and HA7 have different resistances because the anchor HA6 presents a shallow failure.

Table 3.4. Summary of computed helical anchors capacities during vertical uplift loading.

	Anchor ID	**R_{90} (kN)**	**u_z (m)**
One-Plate Helical Anchor	HA1	15.5	0.025
	HA2	18.2	0.025
	HA3	21.6	0.025
	HA4	23.9	0.025
	HA5	27.0	0.025
Two-Plates Helical Anchor	HA6	32.9	0.025
	HA7	35.6	0.025
	HA8	30.1	0.025
	HA9	27.6	0.025
	HA10	37.5	0.025
	HA11	68.2	0.025
	HA12	130.9	0.025

Uplift capacities obtained during previous analyses were validated by comparing the computed bearing capacity factor N_c with the correlations already available in the literature (e.g., Merifield et al. 2003; Wang et al. 2010; Young 2012). This factor is computed as:

$$N_c = \frac{P_{plate}}{A_p s_u} + \frac{\gamma' H}{s_u} \tag{3.3}$$

where P_{plate} is the effective load carried by the plate after subtracting the anchor weight, A_p is the effective plate area without consideration of the shaft (also assumed by others), and all other terms as previously defined. The load at the plates was obtained from the Axial Load Transfer (ALT) at the depth of the plate. Figure 3.12 illustrates the computed ALT for anchors HA3, HA6, HA7, and HA8. This illustrates the importance of: a) the effect of a deep plate anchor, b) how inclusion of an upper plate with a S/D ratio greater than 3 does not reduce the available resistance of each plate but reduces total resistance because a cylindrical shear failure develops for the upper plate, c) how an optimum S/D where plates are sufficiently deep to generate a general bearing failure produces the greatest resistance, and d) shows the reduction in resistance from interaction of two plates spaced closely together at depth.

Bearing capacity factors are presented in Figure 3.13. Computed values for two-plates anchors are observed to be within the range of the ones back-calculated by Young in different soil conditions and anchor geometries. one-plate anchors values are similar to the ones computed by Wang et al. (2012) using numerical simulations for “rough” plates, here considered with an interface with R = 1.0, but with a trend that aligns better with Merifield et al. (2003) equation. Though computed capacities are in the upper part of the real computed values, the numerical approach presented here still is useful to study the helical anchors inclined capacity and interaction between vertical and horizontal loading demand.

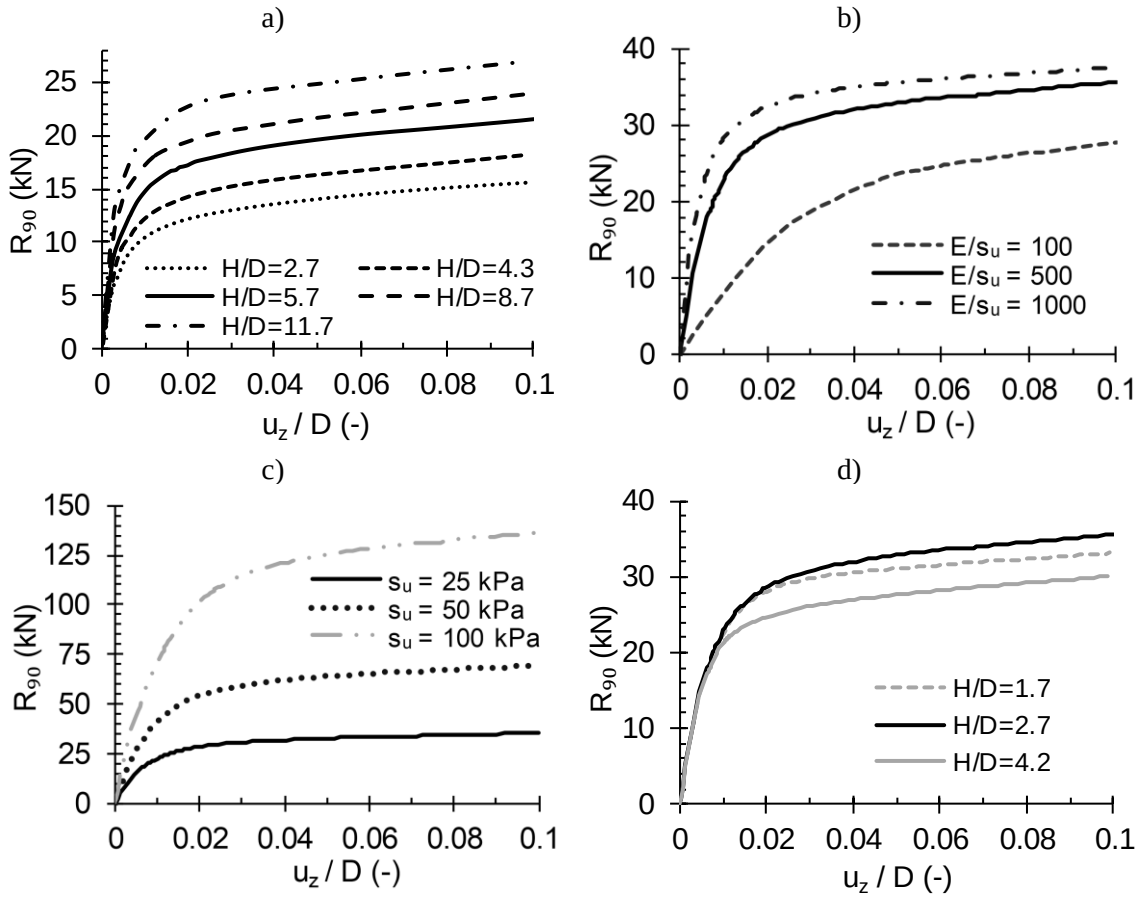

Figure 3.11. Vertical uplift load vs. normalized vertical displacement for: a) one-plate helical anchors at different depths (HA1 to HA5), b) two-plates helical anchors changing E/s_u for s_u = 25kPa, c) changing s_u for E/s_u = 500 constant (HA7, HA11, HA12), and d) changing second upper plate location (HA6, HA7, HA8).Note: H/D = 1.7 has a combined depth and spacing effect.

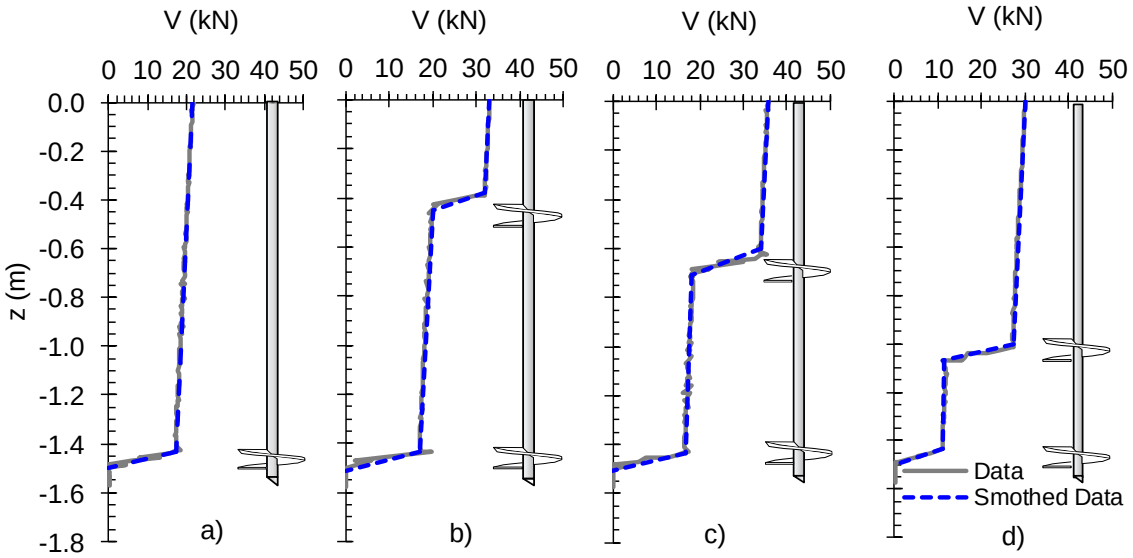

Figure 3.12. Axial Load Transfer of anchors: a) HA3, b) HA6, c) HA7, d) HA8.

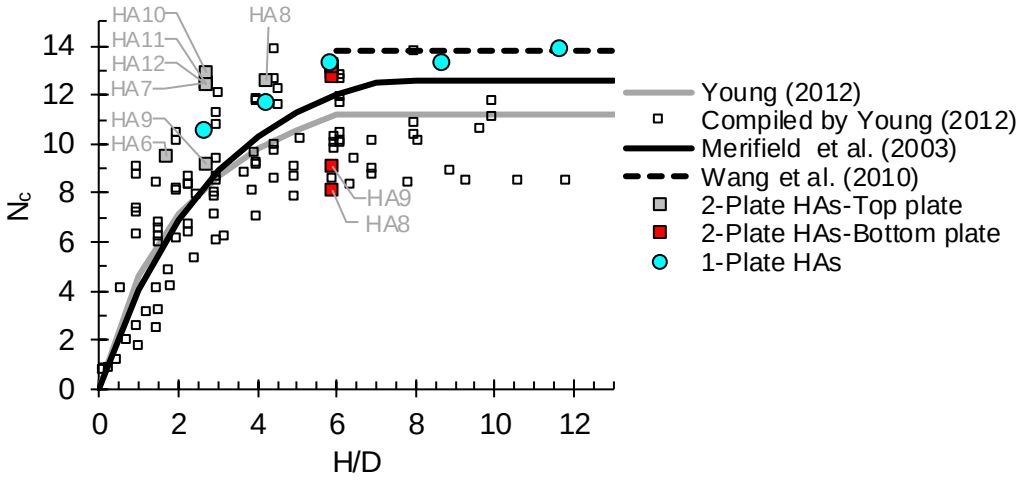

Figure 3.13. Comparison of the obtained Nc factors with the reported in literature

3.6 Lateral Loading

This section addresses the second and third objectives of this chapter that are: i) to investigate the pure horizontal capacity of helical anchors, with specific attention given to the influence of shaft rigidity, soil strength, soil stiffness, and depth of the upper helical plate, and ii) to understand the effect of the helical plate for lateral loading conditions. The knowledge gained in this section, articulated with the previous one, will help to understand and reconcile the anchors capacities in the inclined direction. Load- and maximum moment- displacement curves of each anchor are presented in Figure 3.14 and summarized in Table 3.5 at failure conditions. A sample of the deformed shape and moment diagrams is also presented in Figure 3.15. In summary it is observed that: i) HA1 and HA2 behave as "rigid" anchors (i.e. where nominal bending capacities are never reached), ii) capacity does not change once the anchor is considered long or flexible (e.g., HA3 to HA5), iii) increase in soil stiffness does not result in a significant increase in lateral capacity, but a lower displacement is needed to reach failure, and iv) increase on the undrained shear strength increases the lateral capacity and reduces the amount of movement to obtain failure (for the same stiffness). Details of these observations are given in the following paragraphs.

Results for one-plate helical anchors are presented in Figure 3.14a and b and Figure 3.15a.

Short helical anchors (H/D <= 4.3) behave as rigid elements, never reaching a moment failure and rotating instead of bending. Though recalling Table 3.2 these anchors were classified as semi-rigid and flexible, the flexible one is close to the upper bound limit, meaning that the observed result is reasonable. Note also that HA1 hardens at a displacement of 0.8d. Such hardening is explained by the contribution of the plate that once there is enough rotation, it starts to mobilize uplift resistance lowering the moment distribution with an axial behavior. Although the last three anchors have the same force-displacement behavior, maximum moments are different, with a less "steep" curve for H/D = 5.7 that allows it to develop more displacement before failing structurally. This means that increasing the depth of the anchor does not necessarily increases its capacity. At the plate locations, a reduction of the moment is presented due to the pair developed by these, even when this one is at a depth H/D = 8.7.

Table 3.5. Summary of computed capacities during lateral loading.

	Anchor ID	**R_0 (kN)**	**u_x (m)**	**M_{max} (kN m)**
1 Plate Helical Anchor	HA1	3.9	0.078	0.63
	HA2	7.8	0.078	1.82
	HA3	14.9	0.126	3.35
	HA4	11.1	0.077	3.35
	HA5	11.5	0.080	3.35
2 Plates Helical Anchor	HA6	12.9	0.077	3.35
	HA7	10.9	0.065	3.35
	HA8	11.3	0.078	3.35
	HA9	11.4	0.134	3.23
	HA10	10.8	0.057	3.35
	HA11	12.5	0.032	3.35
	HA12	16.5	0.024	3.49

Note: M_{max} is the maximum value on the moment distribution along the helical anchor shaft and M_n is the nominal or yield moment of the section equal to 3.35 kN m.

Results for different soil stiffnesses, E/s_u ratios and constant s_u = 25 kPa, are presented in Figure 3.14c and d and Figure 3.15b. In a displacement limit criterion, the helical anchor HA9 (E/s_u = 100) has a lower capacity when compared with the other 2 anchors, and as the soil ratio

improves, the capacity improves. However, in the yielding control criteria, HA9 being more rigid can sustain more capacity than the other 2 anchors before breaking apart (if it does, at all). As presented in the previous paragraph, the rigidity of the anchor allows it to develop more displacement before reaching the yielding moment, thus allows it to mobilize more resistance.

Undrained shear strength effects were analyzed in two different ways, leaving $E/s_u = 500$ constant or leaving E = 25MPa constant. For the first case, results are drawn in Figure 3.14e and f and Figure 3.15c. Here a higher undrained shear strength will also imply a higher soil stiffness. The stiffer and stronger the soil, the higher the capacity, and the more flexible is the pile behavior predicting higher moments close to the surface. For the second case, anchors HA10 (s_u = 25 kPa) and HA11 (s_u = 50 kPa) are compared (see Table 3.5), finding that doubling the undrained shear strength increases the lateral capacity 1.16 times. If failure was considered as a displacement limit, such change could be 1.6.

Results for different plate locations and constant soil parameters are presented in Figure 3.14g and h and Figure 3.15d. From the results is observed that: i) the higher the upper plate, the higher the load obtained at a displacement control, as the contribution to the reduction in curvature is observed in the early stage of loading when this plate gets involved, ii) as the loading process continues, the location of the upper plate near the maximum moment (i.e. HA7 with H/D 2.7) the maximum moments are increased because the plate introduces partial fixity at this location, and iii) the lower the second plate, the lower the contribution as the plate does not get very involved in developing partial fixity at shallower depth, yet the same displacement is imposed at the anchor head.

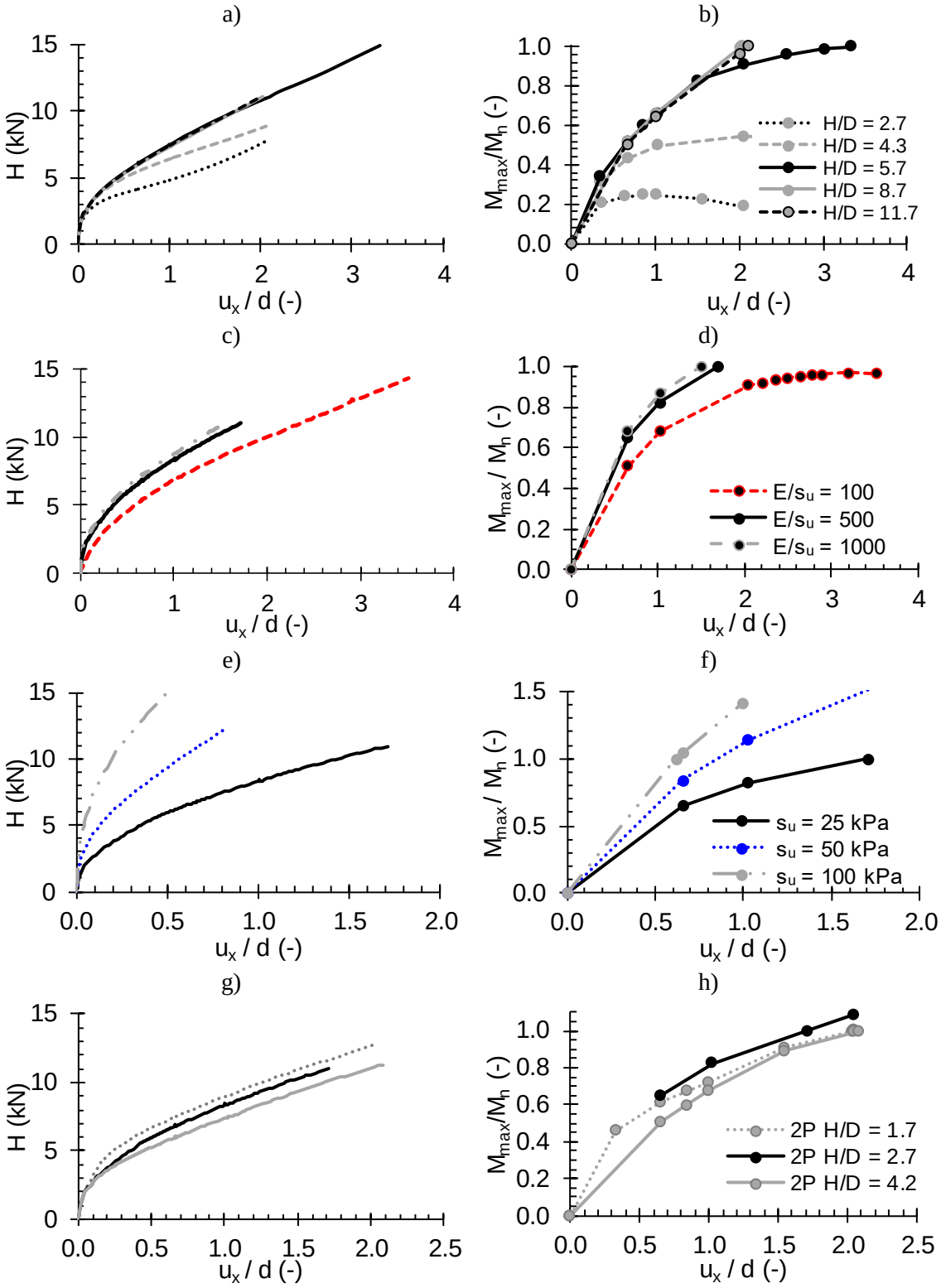

Figure 3.14. Computed force and normalized maximum moment vs. normalized displacement for: a) - b) one-plate helical anchors [HA1 to HA5], c) - d) two-plates helical anchors for different E/s_u ratios and s_u = 25 kPa [HA7, HA9, HA10], e) and f) different undrained shear strength and E/s_u=500 [HA7, HA11, HA12], and g) - h) different upper plate locations [HA6, HA7, HA8].

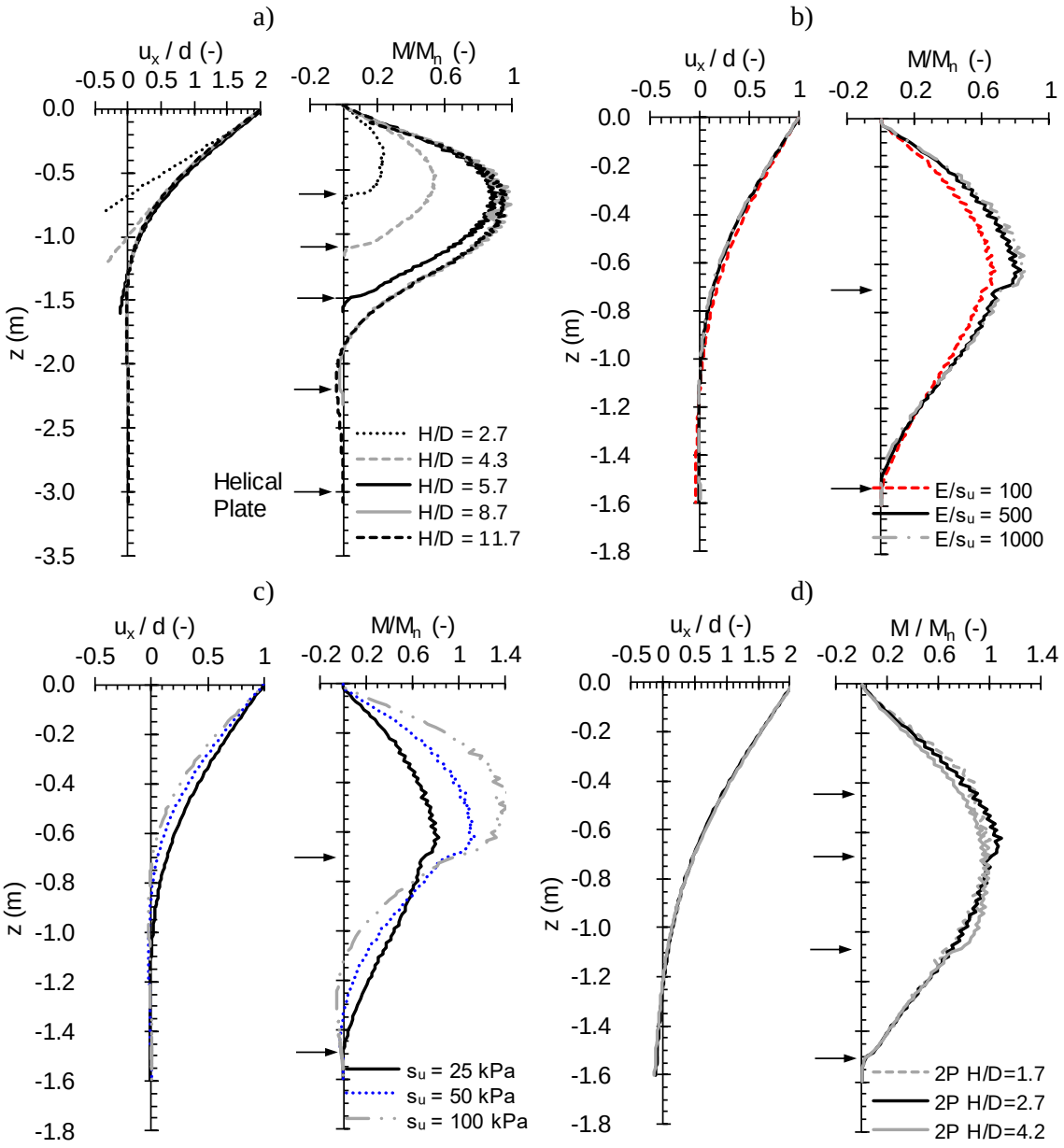

Figure 3.15. Normalized deflection and moment distribution with depth for: a) one-plate helical anchors [HA1 to HA5], b) two-plates helical anchors for different E/s_u ratios and s_u = 25 kPa [HA7, HA9, HA10], c) different undrained shear strength and E/s_u=500 [HA7, HA11, HA12], and d) different upper plate locations [HA6, HA7, HA8]..

3.7 Helical Plate Effect on Lateral Loading

To reconcile the effect of a helical plate under lateral loading, piles with the same properties than the helical anchor's shafts were analyzed. Load- and maximum moment- displacement results

for the helical anchor HA3 are presented in Figure 3.16. At this depth both helical anchor and pile have similar horizontal capacities for the same displacement, however, the presence of the helical plate increases the moment distribution. Such increase is discerned in Figure 3.17a where it is observed that the plate creates fixity at the bottom, reducing rotation, and increasing curvature, thus increasing the moment along the section. Figure 3.17b shows that when the plate is located deeper, the plate effect vanishes. A similar recommendation in this aspect was presented by Puri et al. (1984) where it was said that helical anchors with deep plates locations can be analyzed as piles.

Further analysis for the rest of the helical anchors are presented in Figure 3.18. If fixity is reconciled as the dept that a pile needs to have to behave as flexible (i.e. structurally fails during bending-$M_{max} = M_n$), it can be concluded that when helical anchors are used, the lower plate helps the anchor to develop fixity, by reducing the required pile length. From the results, the depth required to develop fixity, is between 5.5 H/D and 6 H/D. Note that the anchor HA3 (H/D = 5.7), reached failure. However, large displacements were required to develop the plastic hinge compared to those of HA4 and HA5

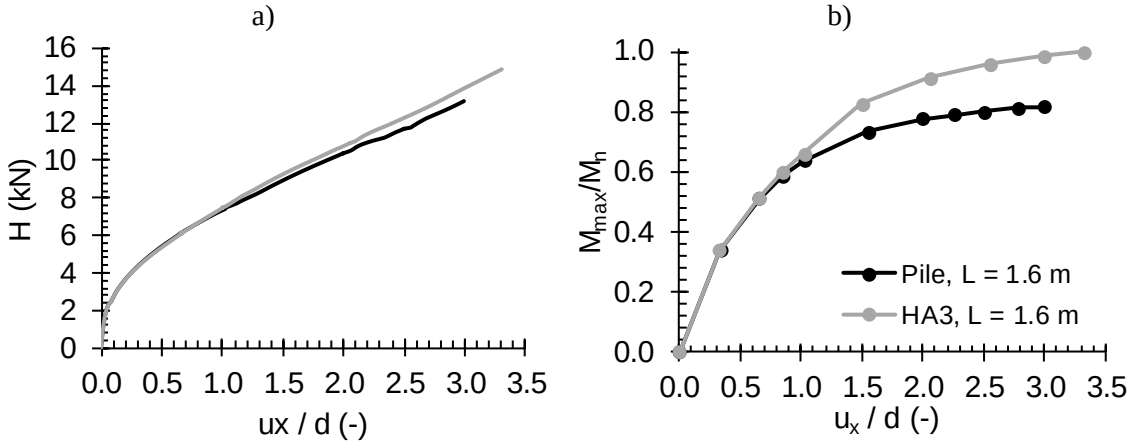

Figure 3.16. Computed lateral loading capacities for one-plate helical anchor and a pile of equal length: a) force- normalized lateral head displacement curve, and b) normalized maximum moment-normalized lateral head displacement.

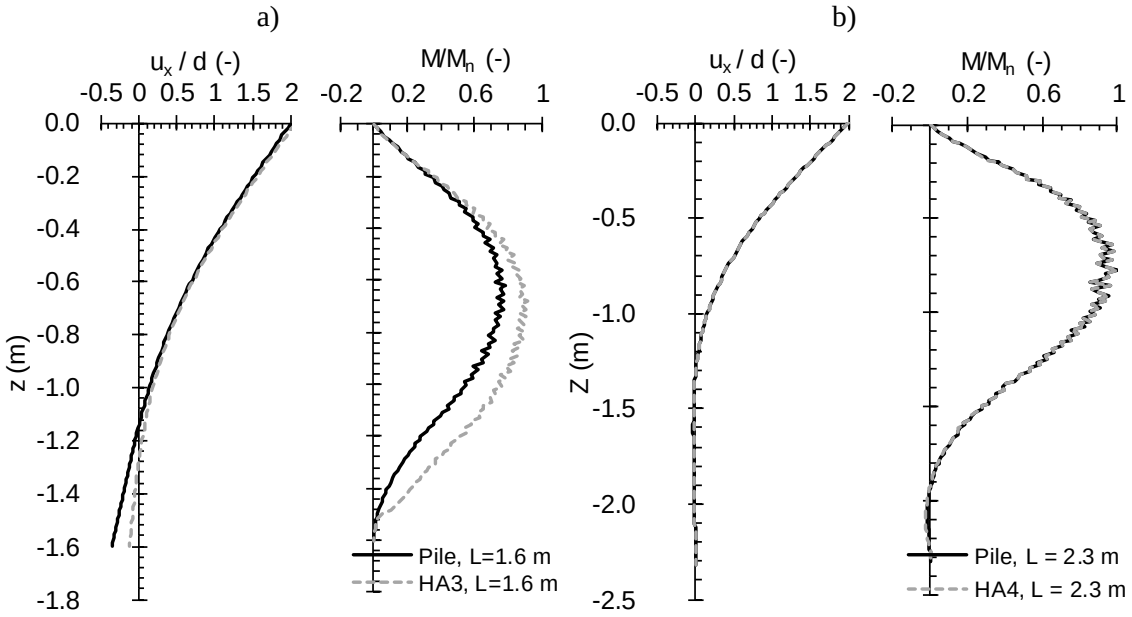

Figure 3.17. Normalized deflection and moment distribution with depth for a one-plate helical anchor and pile of equivalent shaft properties for anchors: a) HA3, L = 1.6 m, and b) HA4- L = 2.3 m.

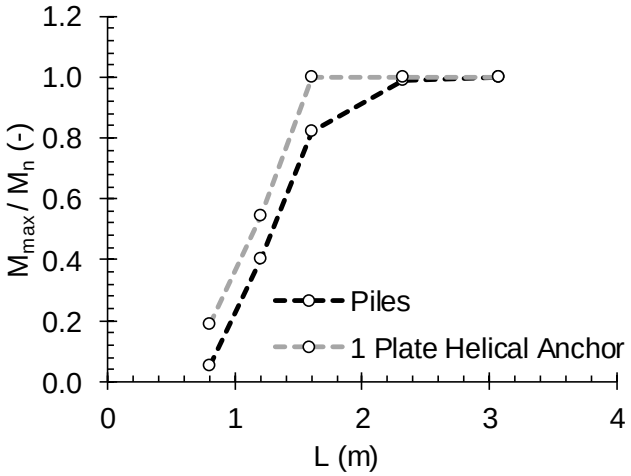

Figure 3.18. Variation of fixity with depth for HA1 to HA5 in the same soil type.

3.8 Interaction of Mobilized Resistance from Uplift and Lateral Loading.

The objectives of this section are to: i) quantify inclined loading resistances, ii) study the interaction effect of the mobilized shear strength during plate uplift and lateral loading, iii) identify

how to predict inclined capacities, and iv) study the optimum inclination angle that combines both structural and geotechnical failure criteria and study how this change with soil properties and anchor geometry.

3.8.1 Inclined Loading Resistances

A summary of the computed inclined loading resistances and failure mode (geotechnical [G] or structural [S]) for the studied anchors is presented in Figure 3.19. Complete details of the load-displacement curves and maximum moment at each load inclination angle are presented in Appendix B. From results, it is observed that: i) Helical anchors have higher capacities at steeper angles than at lower angles as the anchor develops more geotechnical resistance from the plate, ii) long one-plate helical anchors (HA4 and HA5) have higher inclined capacity than short helical anchors (HA1and HA3) at angles close to vertical uplift ($\beta \geq 75°$), but similar capacities at angles lower than this, such behavior is explained with the gain in capacity with a deeper plate, but at the same time the gain in slenderness of the shaft and thus a reduction of structural capacity; iii) two-plates helical anchors present similar inclined capacities when a structural failure mode dominates but different when the geotechnical failure mode does, being higher at higher stiffness, undrained shear strength, and optimum plates spacing as explained in the previous section for vertical loading.

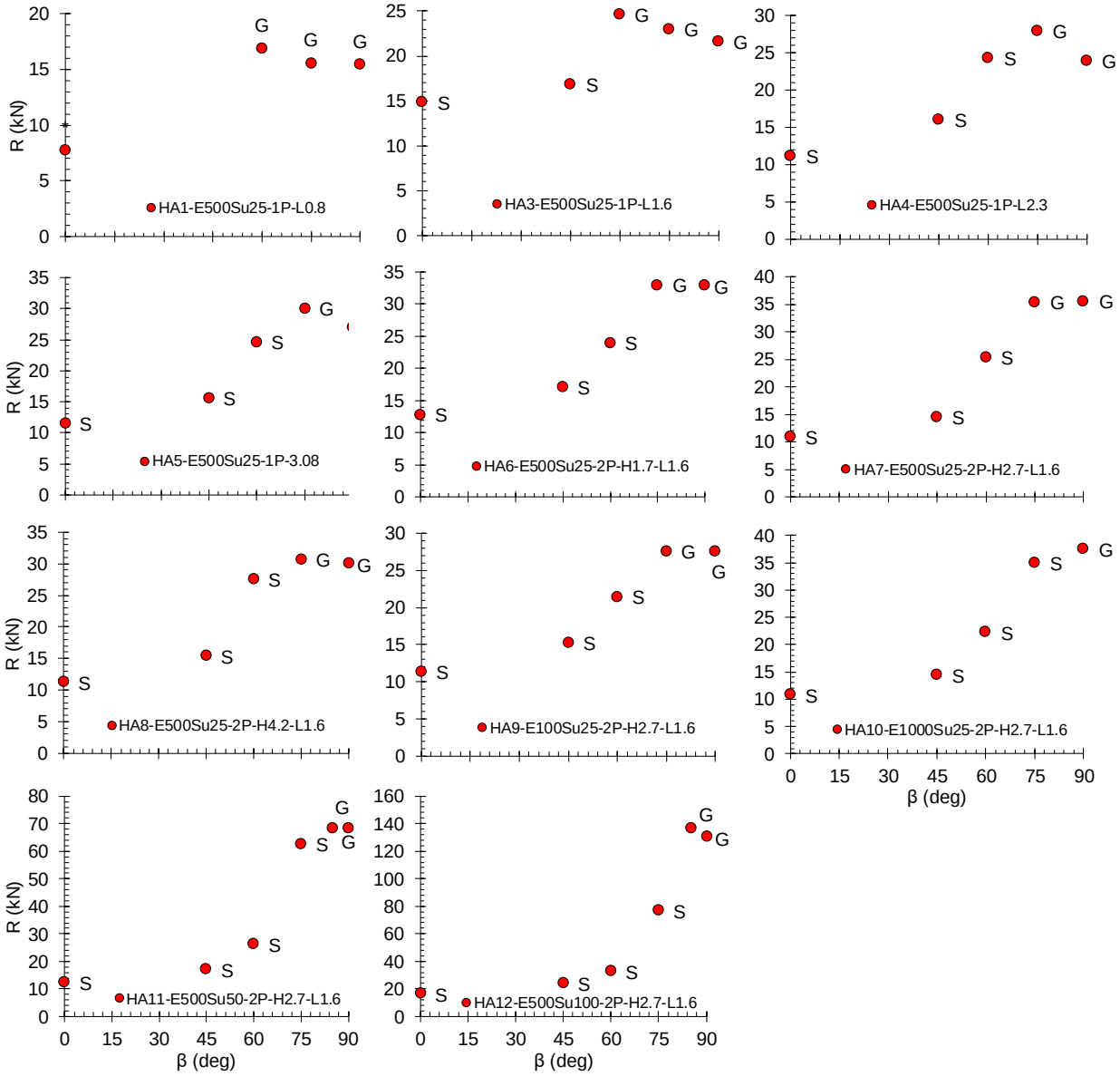

Figure 3.19. Failure modes for inclined behavior. Note G: Geotechnical, S: Structural, failure modes.

3.8.2 Interaction of the Helical Plate and Shaft Under Inclined Loads

The objective of this discussion is to study the interaction between the mobilized resistance by the helical plate and shaft during inclined loading. Mobilized undrained shear strength during inclined loading for HA3 is presented in Figure 3.20. Two mechanisms can be differentiated, the mobilization of the soil above the plate, and the mobilization of a wedge next to the shaft during

lateral loading. With the interaction of such zones, it may be reasonable to consider an influence of one on the other during inclined loading. Two ways will be used to analyze this are: i) looking at the load displacement curves for different plate locations and shaft stiffness, and ii) analyzing the capacities for the failure criterion used in this research.

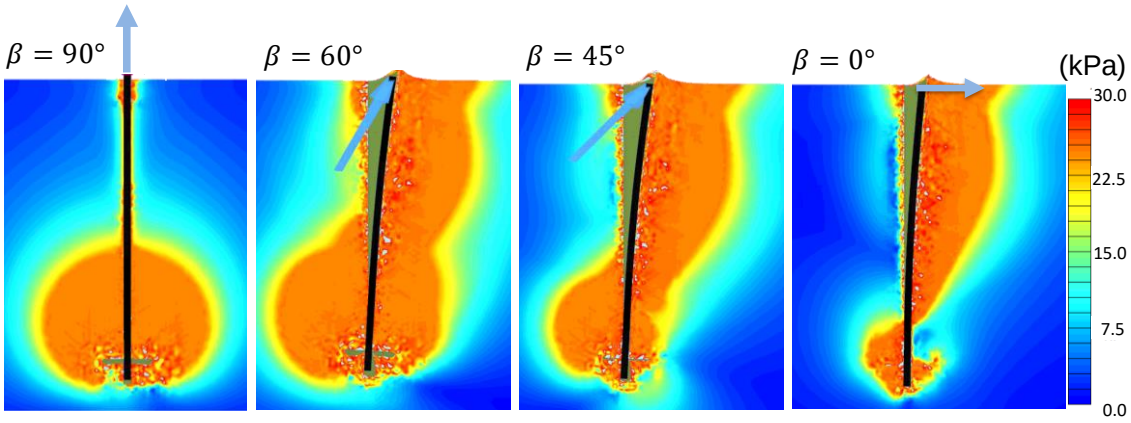

Figure 3.20. Mobilized undrained shear strength during inclined loading

Decomposed vertical and lateral load-displacement curves of the inclined load for the one-plate shallow, intermediate, and long helical anchors (HA1, HA3, HA5) are presented in Figure 3.21. Results indicate that: i) for the shallow HA1 the loading components at any inclined angle are lower than for pure horizontal or pure vertical, due to the overlap between both mechanisms reducing the available resistance at a prescribed displacement; for the intermediate and long anchors, such influence is lower, especially for the long anchor HA5, where the force and displacement components are almost homogeneous. Note in the behavior of the anchors HA3 and HA5 that at 75 degrees, where the failure mode is geotechnical, the horizontal component of the force tends to differ from pure horizontal, and *vice versa* for the 45 degrees case. Such behavior indicates that at angles where both criteria are close, interaction occurs. A comparison between the most rigid (HA9) and most flexible (HA12) two-plates helical anchors is also presented in Figure 3.22. Similar behavior of what it was shown before for different plate locations is shown, however,

the mechanism is dependent not in the depth of the plate but on the anchor shaft stiffness. Similar results were reported by Achmus et al. (2009) for a 2-meter diameter, 10 and 30 meters long concrete piles on sands, were horizontal and vertical loading interaction was more critical for short rigid piles than for long flexible piles.

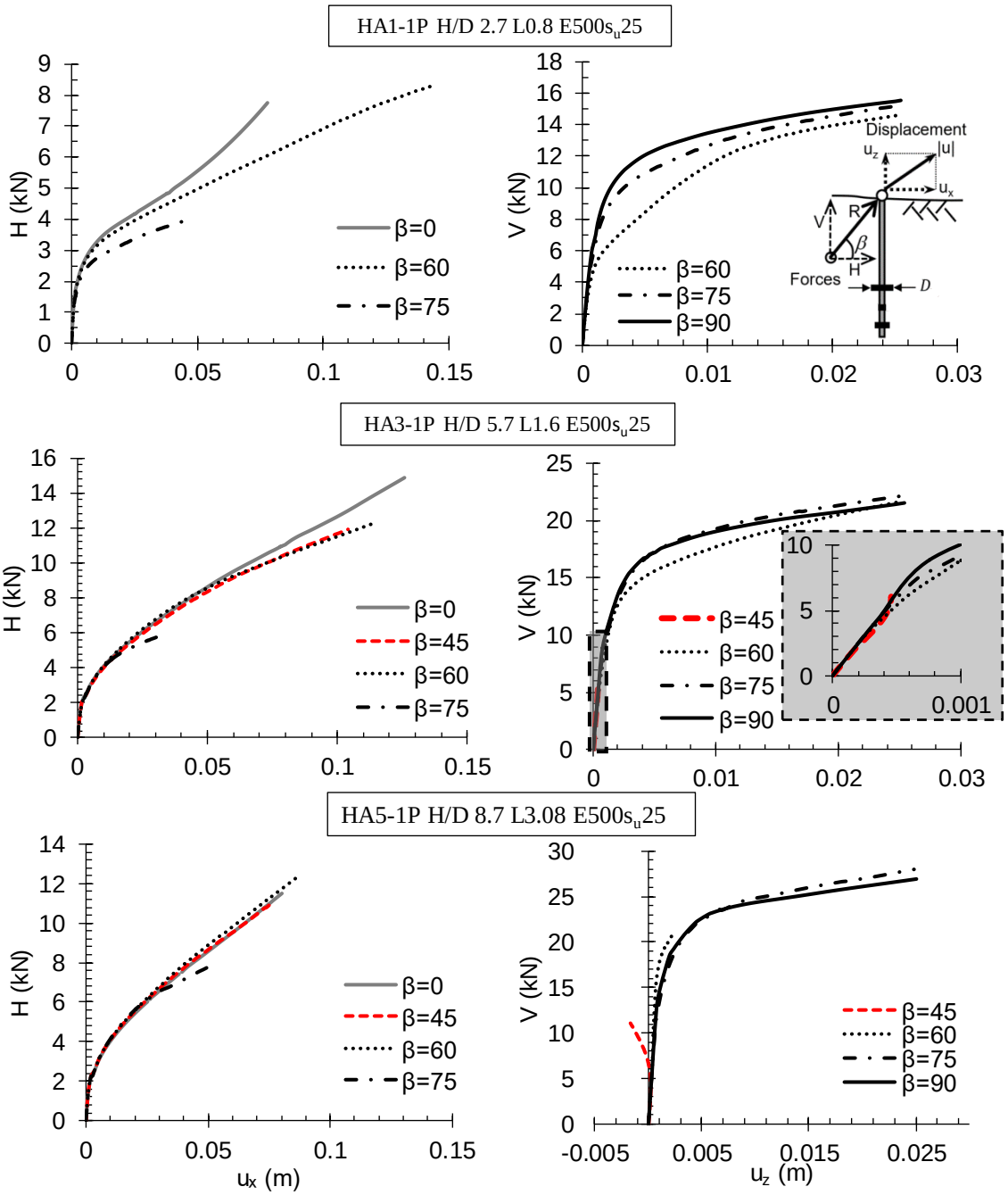

Figure 3.21. Interaction between vertical and lateral components of loading

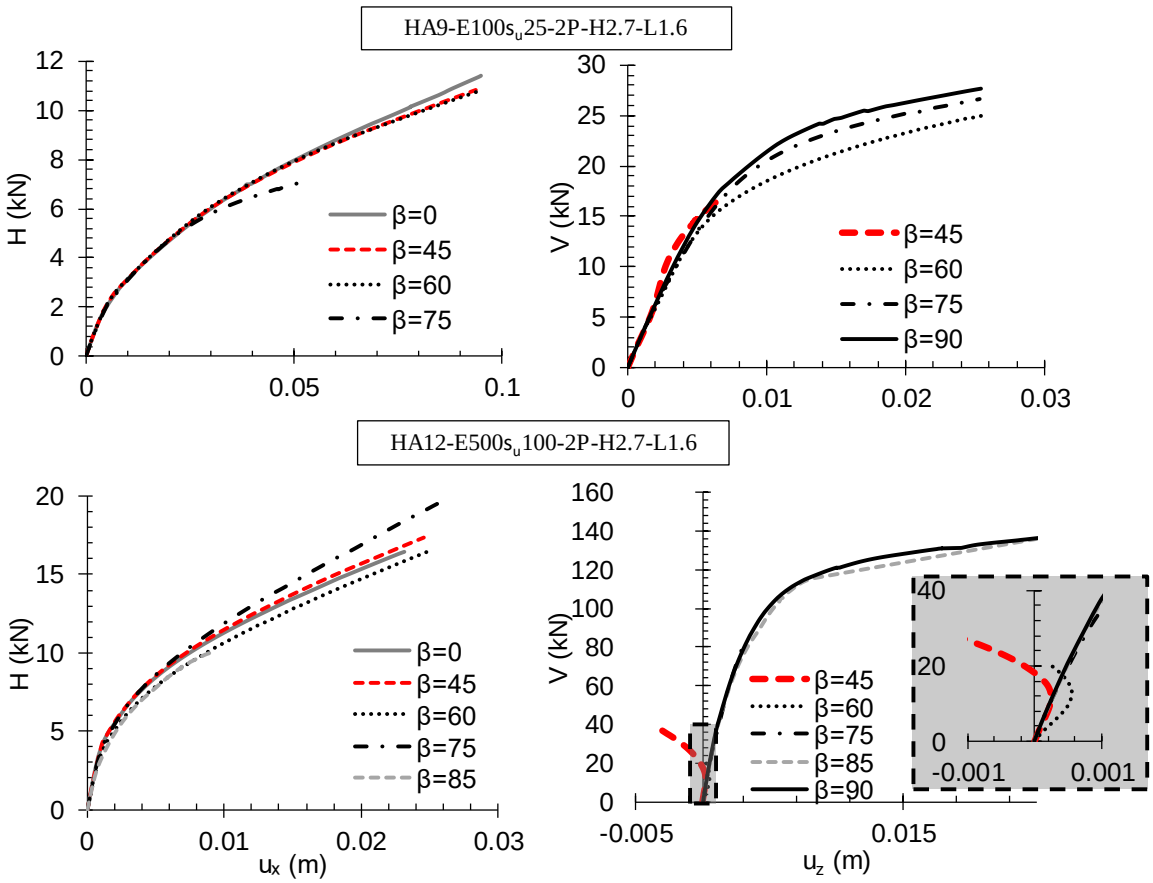

Figure 3.22. Inclined influence on the most rigid (HA9) and the most flexible (HA12) helical anchors.

Another way to check the interaction of the helical plate and shaft under inclined loads is by comparing these with the pure vertical and horizontal resistances at the end of loading. A summary of the normalized vertical and horizontal components of the failure loads computed Figure 3.19 is presented in Figure 3.23. Scatter among the data is due to differences in soil parameters and geometries, and intrinsic solver used by Plaxis during the loading procedure. When geotechnical failure was present at inclined directions, similar capacities to that of pure vertical were observed meaning that not interaction was present. When the structural failure was developed at low angles, no interaction was observed either, however, when more vertical capacity was developed around the plate, the horizontal force incremented. Such behavior can be explained by checking the horizontal load- and maximum moment- displacement curves of the anchors HA4,

HA7, HA8 and HA11 presented in Appendix B. Lateral load-displacement curves at all angles is almost the same for all these anchors, however, moment-displacement curves are less steep at larger angles, allowing more displacement before approaching the yielding moment. The reduction of the moment happens because as the plate fails the soil above and next to the shaft, the shaft is less restricted and can rotate and displace instead of bend, reducing the curvature and moment along the section.

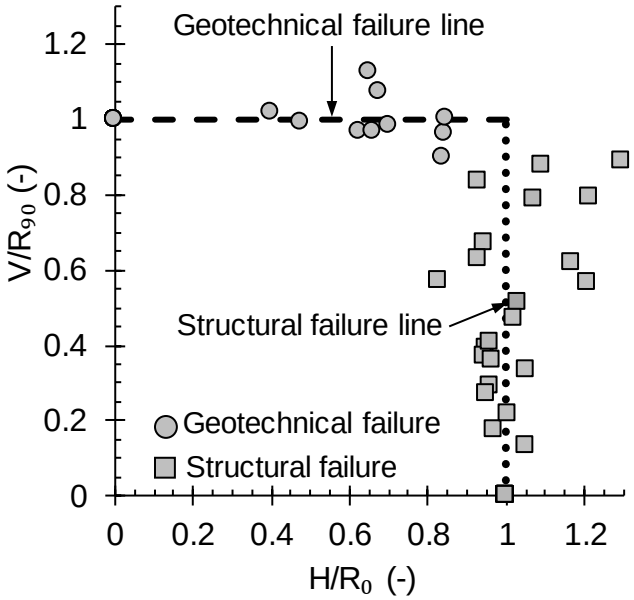

Figure 3.23. Normalized failure envelope for all the studied anchors.

3.8.3 Generalized helical anchor capacity for inclined loading

The objective of this discussion is to provide a generalized equation to predict the helical anchor inclined capacity and study the changes of the optimum inclination angle. In Figure 3.23, approximate geotechnical and structural failure lines can be introduced, so capacities in the inclined spectrum can be represented by the following equations:

Structural failure line:

$$R_{str} = \frac{R_0}{\cos(\beta)} \tag{3.4}$$

Geotechnical failure line:

$$R_{geot} = \frac{R_{90}}{\sin(\beta)} \tag{3.5}$$

and the resistance at any β inclination angle will be:

$$R = \min\left(\frac{R_0}{cos(\beta)}, \frac{R_{90}}{sin(\beta)}\right) \tag{3.6}$$

The previous equations are presented in Figure 3.24, where the failure envelope is the minimum value of both criteria at each angle. A comparison between the predicted capacities and the ones computed before is presented in Figure 3.25. A good agreement is observed among the data with some exceptions nearby the optimum inclination angles where both geotechnical and structural capacity are equal. Note that although the proposed equation is an approximation, it represents a powerful tool to understand the reliability of the entire system being able to predict the capacity at any inclined angle just using the vertical and lateral resistances.

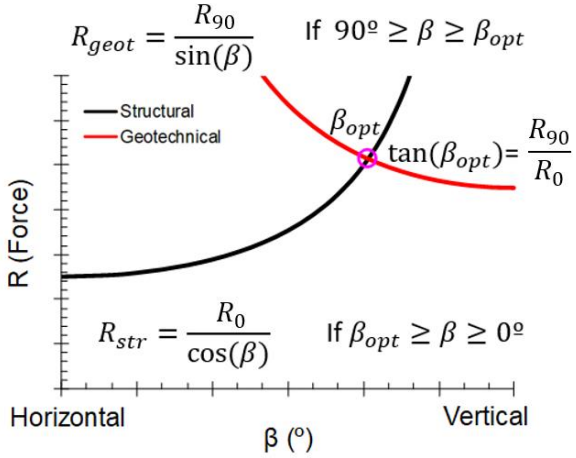

Figure 3.24. Proposed failure envelope equations.

A summary of the changes of the optimum inclination angle for each helical anchor studied is presented in Figure 3.26. From results it is noted that: i) optimum inclination angles are between 60 and 90 degrees, ii) the deeper the one-plate helical anchor, the higher the optimum inclination angle, iii) the more resistant or stiff the soil, the closer to vertical the optimum inclination angle is, iv) the stiffer the helical anchor shaft (higher T), the closer to horizontal the inclination angle is, or the more flexible the shaft, the higher the angle. To summarize, long flexible anchors (or "weak" anchors on stronger soils) have optimum angles near the vertical direction while rigid shafts helical anchors ("strong" anchor in weak soil) have optimum angles near the horizontal direction.

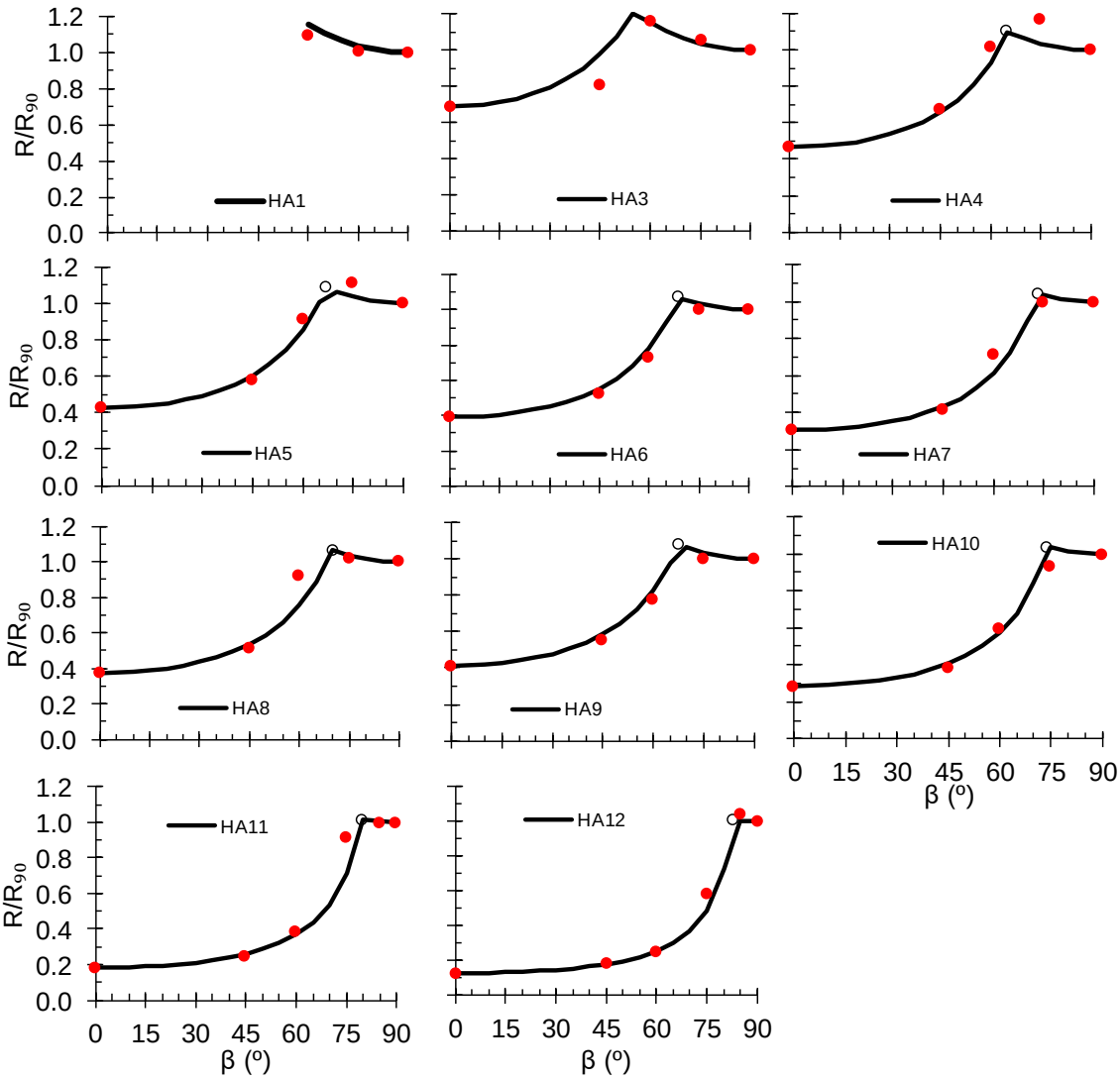

Figure 3.25. Comparison between predicted and computed inclined capacities

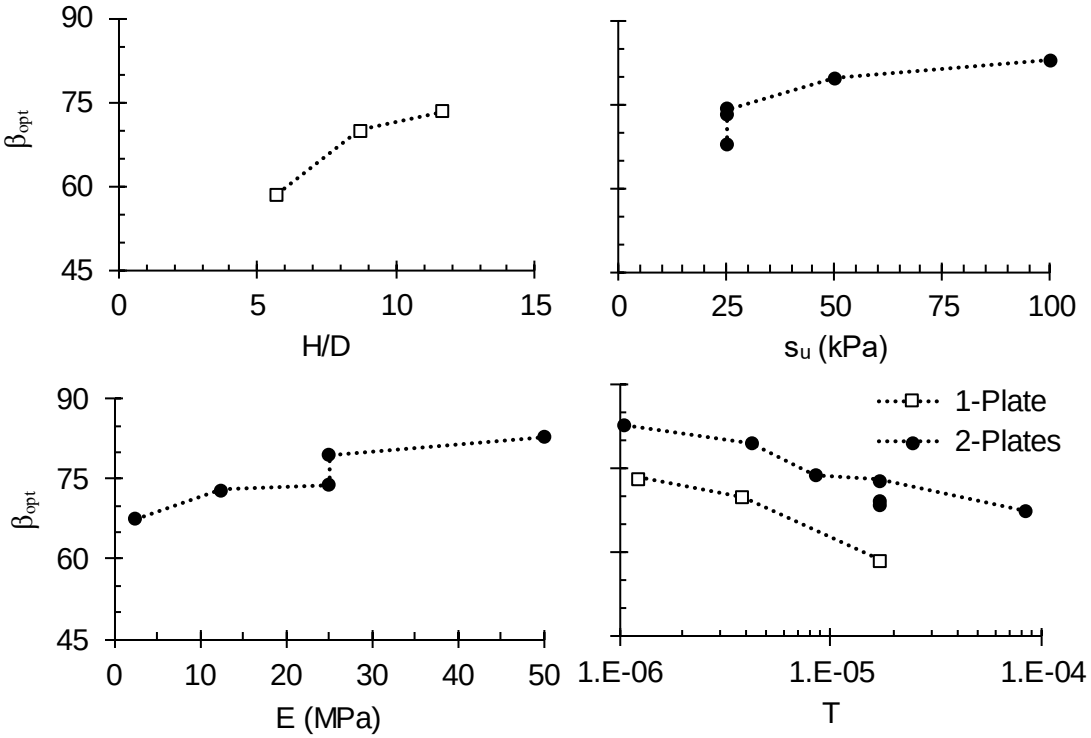

Figure 3.26. Changes of the optimum inclined load angle with geometry and material properties.

3.9 Summary and Conclusions

This chapter presented 3D finite element simulations to investigate the capacity of helical anchors under different load inclinations. The objectives of these numerical analyses were: i) to validate the finite element model with previously published results for vertical pullout; ii) to investigate the pure horizontal capacity of helical anchors, with specific attention given to the influence of shaft rigidity, soil strength, soil stiffness, and depth of the upper helical plate; iii) to understand the effect of the helical plate for lateral loading conditions; iv) to study how the capacity or ultimate line load is influenced by the inclination angle; v) to investigate the interaction between the mobilized uplift resistance generated by the plate and the lateral resistance generated along the shaft under inclined loading scenarios; and vi) to explore the optimum inclination loading angle and how this is influenced by shaft rigidity, soil strength, soil stiffness, and depth of the upper helical plate. The following observations and conclusions were drawn:

- Based on the assumed failure criteria for pure vertical loading, the pullout capacity increases with depth of the upper plate, soil stiffness, undrained shear strength, and increased plate spacing (up to $S/D = 3$) for multi-plate anchors.
- For lateral loading of helical anchors simulated in this study with H/D < 5.7, a plastic hinge does not develop at any deformation. For the anchors simulated in this study with H/D $\geq$ 5.7, helical anchors transition from rigid to flexible elements such that a plastic hinge develops and structural capacity of the anchor controls.
- The presence of a plate creates greater fixity and increases the curvature and moment. With such increase in moment, the plate reduces the required depth to achieve fixity compared with a "pile" having equivalent shaft dimensions. When the plate is located deep enough to achieve fixity and the anchor is considered flexible, the lateral capacity of the helical anchor remains unchanged regardless of the plate depth.
- Mobilized lateral resistance increases at the same deformation when a helical anchor is embedded in soil with lower ratios of E/s_u for the same undrained shear strength.
- For inclined loading the mobilized resistance increases with increasing load inclination as there is greater mobilization of soil shear strength around the plates (i.e. approaches maximum geotechnical capacity).
- An optimum inclination angle, which describes the load inclination where the greatest resistance is achieved based on the combined failure criterion, is achieved at angles between 60 and 90 degrees for helical anchors simulated in the numerical analyses. Shafts with greater rigidity (i.e. bending stiffness, EI) have a lower optimum angle while anchors with a more flexible shaft have a higher optimum angle. Note that this does not imply this is the optimized (i.e. best) line load inclination for an aquaculture system (discussed in the following chapter), but the optimal angle to simultaneously mobilize both the geotechnical and structural capacity.

- For inclined loading there is the potential for interaction of mobilized zones near the plate and along the shaft due to vertical uplift and lateral loading, respectively. An initial concern was that interaction of these zones may reduce the total available capacity. However, interaction between vertical and horizontal loading was found to be present for the short (H/D < 2.7) one-plate helical anchors where the plate influences the horizontal resistance as it mobilizes soil resistance adjacent to the shaft during lateral loading and rotation, causing these mobilized zones to overlap. However, the influence of this interaction decreased significantly for deeper plates with H/D > 5.7.
- When the most rigid and most flexible two-plates helical anchors were compared, it was found that the interaction of the inclined loading was more important for the rigid anchor than for the flexible. This result is similar to the results presented by Achmus et al. (2009) for concrete piles.
- When the interaction was analyzed at ultimate levels, it was found that at angles closer to optimum, the overlap of the soil yielding above the plate and the one mobilized by the shaft increased the total capacity. This positive impact because the soil loose reaction against the anchor allowing it to reduce its curvature and moment, making it yield at higher displacements that allows more shear strength mobilization.

4 PREDICTING THE FAILURE ENVELOPE AND RELIABILITY OF HELICAL ANCHORS SUBJECT TO INCLINED LOADING

In the previous chapter the relationship between the lateral and vertical capacity of helical anchors to the failure envelope under inclined loading was demonstrated with 3D finite element analyses. Based on these findings it is possible to construct a failure envelope for inclined loading computing pure vertical and lateral resistances. Studies of helical anchors vertical pullout have shown that the individual plate bearing or cylindrical shear theories predict reasonable pullout capacities. However, predicting lateral capacity is more complex. Lateral load-deflection (*p*-*y*) analyses are an alternative approach to fully 3D finite element analyses to predict lateral capacity and are computationally less expensive than more advanced numerical techniques. Although the helical plate is not explicitly considered with such analyses, the computed results from finite element analyses indicate that helical anchors behave similar to piles when the plate is substantially deep to develop fixity at or above the plate location (see section 3.7). The objectives of this chapter are to:

- Present a methodology to predict the combined failure envelope that considers both structural and geotechnical resistance of an anchor using the well-established *p*-*y* method for estimation of lateral capacities and analytical methods for estimation of vertical pullout capacity. The goal is to create an easily transferrable approach with methodologies familiar to geotechnical engineers that may be applied to design of helical anchors.
- Introduce a framework to evaluate the reliability of helical anchors under inclined loading by means of an optimization technique with the Hasofer-Lind method (Ditlevsen 1981, Madsen et al. 1986).
- Demonstrate the methodology to assess reliability of a helical anchor for an oyster aquaculture farm in the Damariscotta River, Maine, where mooring loads and their inclination angles were documented as part of the SEANET project at University of Maine.

This chapter is subdivided into six subsections, starting with a comparison between the finite element simulations and the *p-y* analysis, followed by presentation of a simplified methodology to construct the failure envelope via p-y analyses and analytical estimation of the vertical pullout resistance. Reliability concepts are then introduced and a framework to evaluate reliability of helical anchors subject to inclined loading is presented. Finally, a reliability assessment for a real oyster aquaculture farm is performed followed by a summary and conclusions from findings reported in this chapter.

4.1 Finite Element Simulation vs. *p-y* Analysis to Predict Lateral Capacity

The main purpose of this section is to compare resistance computed from finite element calculations with *p-y* analyses to justify a simplified approach to predict lateral capacity (i.e. yielding of the anchor) that can be conveniently embedded within a reliability framework presented in the following sections of this chapter. The *p-y* method is used for the analysis of buried piles that experience lateral loads or moments by using a 2D finite difference analysis. Such analysis discretizes the pile into a series of segments joined by nodes, where the soil reaction is simulated by series of nonlinear springs. The structure is defined with its flexural stiffness while the soil reaction is simulated with linear, bilinear, or nonlinear *p-y* (e.g., load-deflection) curves at each depth. A graphical representation of this analytical method is presented in Figure 4.1. Different *p-y* curves are assigned to different nodes to better predict the increase in soil resistance and stiffness with depth. Ultimate reaction forces (p_u) are usually related to the soil resistance (i.e. s_u), while the stiffness, k_{sec}, is a linear or nonlinear spring constant, usually related to the soil modulus E. The finite difference method solves the 4th order differential Equation (4.1) as a function of the displacement y_i of each node at each depth.

$$E_p I_p \frac{d^4 y}{dy^4} + k_{sec} y = 0 \tag{4.1}$$

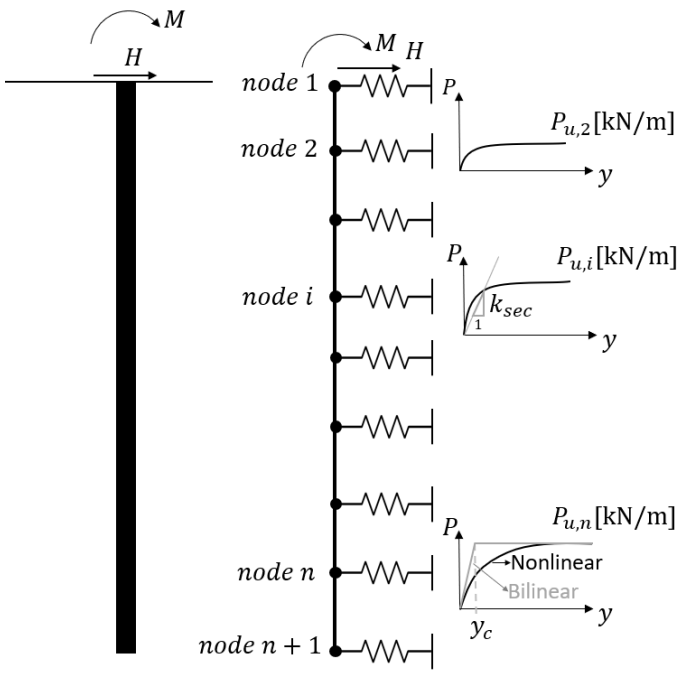

Figure 4.1. Analytical model for *p-y* analysis.

A comparison between the force-displacement curves, deflected shape, and bending moment diagrams computed with the 3D Finite Element (FE) model and the *p-y* method using RSPile (Rocscience 2018) for the helical anchor with a 3.1 m length are presented in Figure 4.2 and Figure 4.3, respectively. Note that "y" from *p-y* analysis is equivalent to the lateral displacement u_x analyzed during FE simulations. A bilinear *p-y* curve (Figure 4.1) with an ultimate resistance, $p_u = 10s_u(d)$, at a yield displacement, $y_c = 0.02(d)$, was used for this comparison. The ultimate resistance of clay soils is typically (8 to 12)$s_u(d)$ and 10 was selected as the average value. The value of y_c is the deflection at which the soil yields, chosen to generate an equivalent modulus of subgrade reaction for soil with $E = 12{,}500\ kPa$ in the finite element analyses. The *p-y* prediction of mobilized resistance (Figure 4.2) shows good agreement with computed results from 3D finite element analyses when a non-updated mesh (NUM) analysis is applied. There is still good agreement during the initial stages of loading (smaller displacements) when an updated mesh (UM) analysis is used for “large” displacements, though higher capacities are predicted with computed

results from the FE analysis at larger displacements. Regardless, the deflected shape and the moment distribution when the helical shaft yields show relatively good agreement, though *p-y* analyses tend to predict larger displacements for the same depth above the fixity point (Figure 4.3).

The greatest difference in the computed responses are between the FE analyses using a non-updated mesh (Eulerian) and the updated mesh (Lagrangian) technique to resolve displacements and stresses in both the soil and structural elements at large displacements. However, as previously mentioned, yielding of the shaft (of concern here) is predicted at similar loads for the Eulerian technique and the *p-y* method. While the Lagrangian approach has been applied by several researchers (e.g., Wang et al. 2013; Wang et al. 2010; Wang et al. 2006) to simulate vertical pullout with the finite element method, which requires relatively large displacements, structural resistance is more relevant here. Structural resistance associated with lateral loading occurs at relatively small displacements compared with a geotechnical bearing failure. Therefore, it may be concluded that *p-y* methods are a reasonable approach to estimate the lateral capacity of helical anchors, which is needed to develop the combined structural and geotechnical failure envelope.

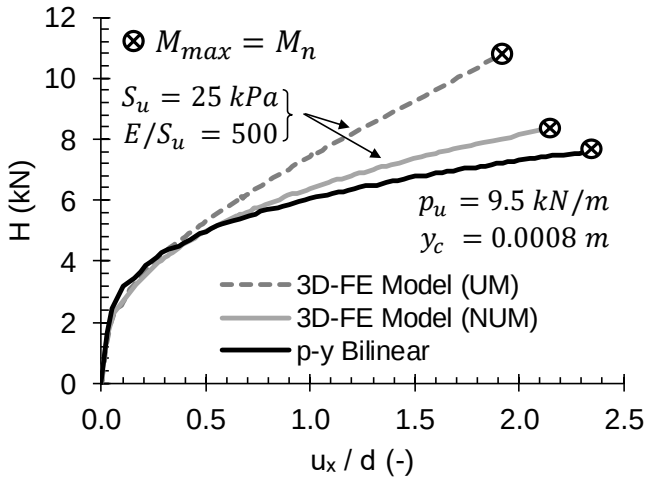

Figure 4.2. Force-displacement comparison between linear finite element and linear *p-y* analysis.

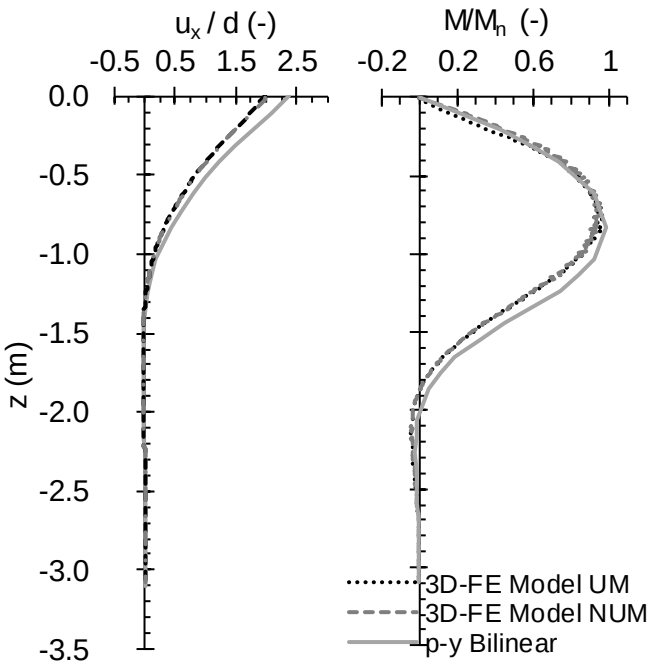

Figure 4.3. Comparison between displacements and moments distributions between FEM and *p-y* linear analyses for laterally loaded helical anchors.

As demonstrated in Chapter 3, the failure envelope may also be constructed from *p-y* analyses in combination with the analytical techniques to estimate the vertical capacity as shown in Figure 4.4. Horizontal capacities can be estimated with the *p-y* method bearing in mind the accuracy of this for long elements. Vertical capacities can be predicted using previously reported bearing capacity factors for helical plates considering the embedment depth.

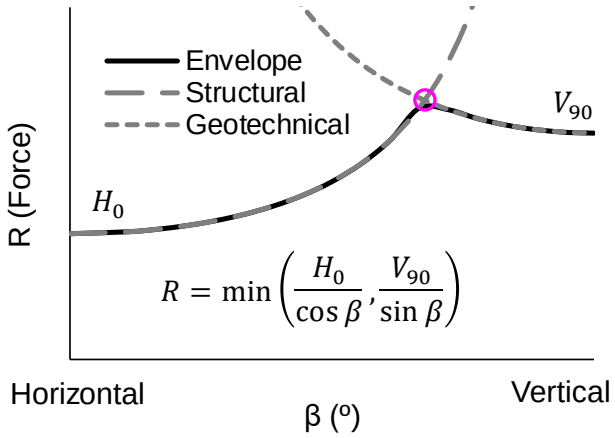

Figure 4.4. Failure envelope determined from horizontal capacity from (*p-y* analysis) and vertical capacity from analytical methods.

Several reaction-displacement *p-y* curves have been developed for different soils based on full-scale instrumented pile load tests (e.g., Matlock 1970; Reese et al., 1975; Welch and Reese, 1972). The nonlinear soil response and for some cases, deflection-dependent strength degradation is incorporated. Use of *p-y* curves is the industry standard for analysis of laterally loaded deep foundations, which are akin to laterally loaded helical anchors, although helical anchors shaft diameters are typically smaller than most piles. A typical normalized curve used for soft clay is presented in Figure 4.5. Soil resistance is normalized with respect to an ultimate resistance, p_{ult}, which changes with depth. Soil stiffness is accounted for in the determination of a critical deflection, e.g., y_{50}, represented in terms of an equivalent strain parameter, ϵ, or percentage of the shaft diameter. The secant modulus or modulus of subgrade reaction is not constant and degrades as displacements increase. Therefore, it may be observed that computed resistance with the nonlinear *p-y* curve generates lower resistances when compared with 3D FE simulations that incorporated a linear elastic perfectly-plastic constitutive model; i.e. the *p-y* curve can result in lower resistances at a given displacement than 3D FE simulations because the equivalent soil modulus degrades more during loading. This is illustrated in Figure 4.6, where it is noted that: i) the FE model with the same undrained shear strength but different stiffness gives a lower resistance for lower values of Young's modulus, and ii) the lower the elastic modulus, the closer the solution is to the nonlinear *p-y* curve for soft clays, implying the equivalent secant modulus of subgrade reaction at p_{ult} for the *p-y* curve is similar to lower values of Young's modulus used in 3D FE analyses. As soil yields along the length of the shaft, smaller displacements are required to mobilize the same resistance in stiffer material. Once the size of a wedge of *yielding* soil along the shaft is similar (e.g. near depth of fixity), growth of the load-displacement curves become similar at larger displacements because rigidity of the shaft itself largely controls deflections once the soil has yielded.

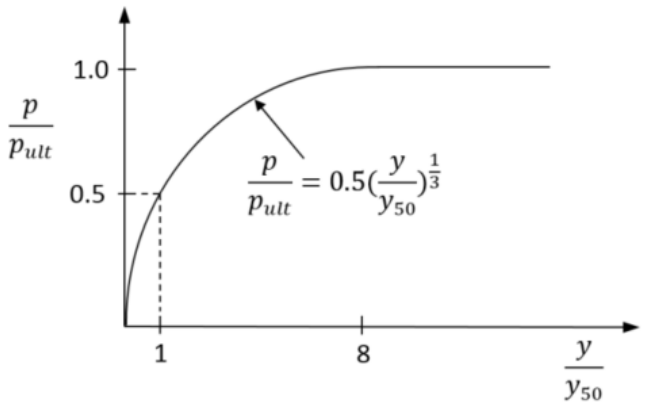

Figure 4.5. *p-y* curve for soft clay (Matlock, 1970).

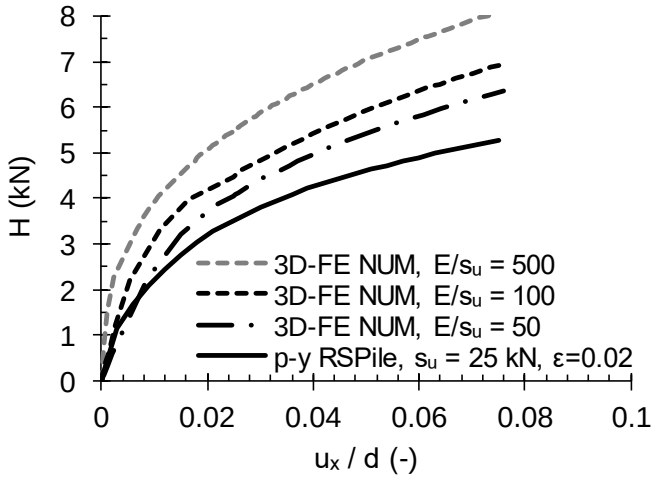

Figure 4.6. Nonlinear *p-y* analysis vs. linear FE simulations of helical anchors with same undrained shear strength.

FE simulations using a linear elastic constitutive model were necessary to reconcile how the interaction of mobilized resistance around the plate affects resistance mobilized along the shaft, as well as how the plate contributes to "fixity" of the anchor at depth when subjected to inclined or lateral loads. Such FE simulations also provided unique insight into construction of a failure envelope defined by the limiting structural or geotechnical resistance and load inclination angle. However, these 3D analyses were limited by the use of a linear elastic perfectly-plastic constitutive soil model. While this model does capture yielding of the soil, it does not simulate the non-linear response of the material at smaller deformations, which is more important for more realistic

determination of deflections and mobilized structural resistance. Non-linear *p-y* curves provide a more realistic constitutive soil response when evaluating lateral capacity. If more advanced non-linear constitutive models were adopted for 3D FE analyses, which would be computationally expensive, greater similarity in the simulated load-deformation response might be found when compared to *p-y* analyses incorporating non-linear soil springs. Recall that when a *p-y* analysis was performed using a linear elastic perfectly-plastic soil spring (i.e. bilinear spring), there was good agreement with the FE model. This is important to bear in mind when considering the adequacy of *p-y* analyses to predict lateral capacity, which is largely dependent on the simulated response of the soil. Non-linear response of the soil is expected under lateral and inclined loads, and use of non-linear soil springs developed for the appropriate soil type (e.g. soft clay model by Matlock 1970) is justified for prediction of the lateral capacity used to generate the failure envelope that incorporates both structural and geotechnical resistance of the anchor (Equation (3.6) presented in Chapter 3).

4.2 Alternative Methodology to Estimate Lateral Loading Capacity with *p-y* Analysis.

As explained before, *p-y* analysis is a conventional methodology to predict lateral capacity of "deep" piles. The methodology has been implemented in multiple commercial finite element and finite difference codes, which typically use published *p-y* curves that capture the constitutive response of soil in different materials. These programs are generally accessible and regularly used by geotechnical engineers for lateral analysis of deep foundation systems. However, one objective of this research is to use the simplified methodology presented here to predict capacity of the anchor in a reliability framework. Therefore, it was more convenient to conduct *p-y* analyses outside commercially available software packages. Low et al. (2001) introduced a methodology to evaluate lateral loading using a spreadsheet solver that iterates the bottom nodes lateral displacements until moment and shear forces equilibrium are reached (Figure 4.7). The Low et al. (2001) methodology was originally implemented in Microsoft Excel, but herein it was implemented in Matlab (The

MathWorks 2018) for convenience in this study. The problem optimization routine for structural failure condition is presented in Table 4.1 using the equations (4.2) to (4.7). The computed response with the Low et al. (2001) methodology is compared with results from commercial software (Rocscience 2018) in Figure 4.8 to validate and to demonstrate adequacy of the approach. There is negligible difference in the simulated load deformation response from the method implemented in Matlab when compared with computed results from commercially available code. Details regarding the Matlab code are presented in Appendix C.

$$y_i = y_{i+1} + \left(\frac{\Delta Z_{i+1}}{\Delta Z_{i+2}}\right)^2 (y_{i+2} - y_{i+1}) - \Delta Z_{i+1}\left(1 + \frac{\Delta Z_{i+1}}{\Delta Z_{i+2}}\right) y'_{i+1} \tag{4.2}$$

$$p_i = -k_{sec}\, y_i d \tag{4.3}$$

$$Q_i = Q_{i+1} - 0.5(p_{i+1} + p_i)(z_{i+1} - z_i) \tag{4.4}$$

$$M_i = M_{i+1} - Q_{i+1}(z_{i+1} - z_i) + 1/6\,(z_{i+1} - z_i)^2(2p_{i+1} + p_i) \tag{4.5}$$

$$y'_{n+1} = (y_{n+1} - y_n)/(z_{n+1} - z_n) \tag{4.6}$$

$$y'_i = y'_{i+1} - 0.5\left(\frac{M_{i+1}}{E_p I_p} + \frac{M_i}{E_p I_p}\right)(z_{i+1} - z_i) \tag{4.7}$$

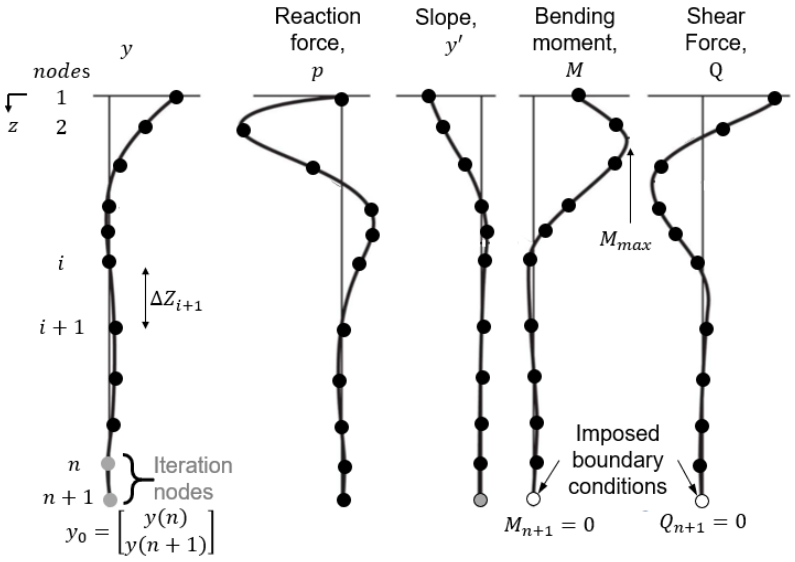

Figure 4.7. Low et al. (2001) formulation to compute displacements, soil reaction, pile rotations, bending moments and shear forces along the pile length.

Table 4.1. Framework in Matlab using the Low et al. (2001) methodology for *p-y* analysis of laterally loaded piles and helical anchors at the limiting bending condition.

Optimization task:

$$minimize[Capacity\ (y_0)]$$

where capacity is the objective function given by:

$$Capacity = \sqrt{\left(max\left(\vec{M}\right) - M_y\right)^2}$$

subject to:

$$\vec{M}_1 = 0$$

where M_y is the shaft yield moment, $\vec{M}$ the moment distribution with depth, and M_1 is the moment at the anchor head (= 0 for free head with no eccentricity above seabed). This optimization will be satisfied when $Capacity$ equals zero by changing the displacement y_0 at the bottom (tip) two nodes of the pile. The moment vector in the shaft is computed via the following steps:

$y_0 = [y_n, y_{n+1}]$	**Step 1:** Define initial values for the bottom two iteration nodes where n is the number of segments in the z vector.
$p_{(n,n+1)}$ from Equation (4.3)	**Step 2:** Compute soil reaction force normal to pile on the initial values using a *p-y* curve.
$Q_{n+1} = 0$ (enforced boundary condition) Q_n from Equation (4.4)	**Step 3:** Compute shear forces at the bottom two nodes at the capacity condition, and with an assumed trapezoidal distribution integrate the soil reaction.
$M_{n+1} = 0$ (enforced boundary condition) M_n from Equation (4.5)	**Step 4:** Compute bending moments at the node above the bottom at the capacity condition to find the reaction force distribution.
y'_{n+1} from Equation (4.6) y'_n from Equation (4.7)	**Step 5:** Compute the rotation at the bottom nodes from applying direct slope between the last two nodes and first moment area theorem to relate moments and rotation. E_pI_p is the pile bending stiffness, which can also be variable if non-linear moment-curvature relationships are used.
y_i p_i Q_i M_i y'_i	**Step 6:** Perform a *For* loop from $i = n - 1$ to $i = 1$ (i.e. moving up the shaft), repeating steps 2 through 5 after computing the new lateral displacement with a quadratic curve fitting.
del convergence tolerance (e.g., 0.0001) $Maxiter$ max number of iterations (e.g., 100) While $iter<maxiter$ and $Maxdiff>del$ If $i = 1$, $y_{prev} = 0.0001$ else, $y_{prev} = y_i$ Run $Equilibrium$ to find y_i $Maxdiff = max\left(\lvert y_{prev} - y_i \rvert\right)$ End while	**Step 7:** Run the $Capacity$ routine by iterating displacements of the bottom nodes (n, n+1) and verify that the computed deflections converge by comparing the max difference in deflections until a threshold tolerance is achieved.

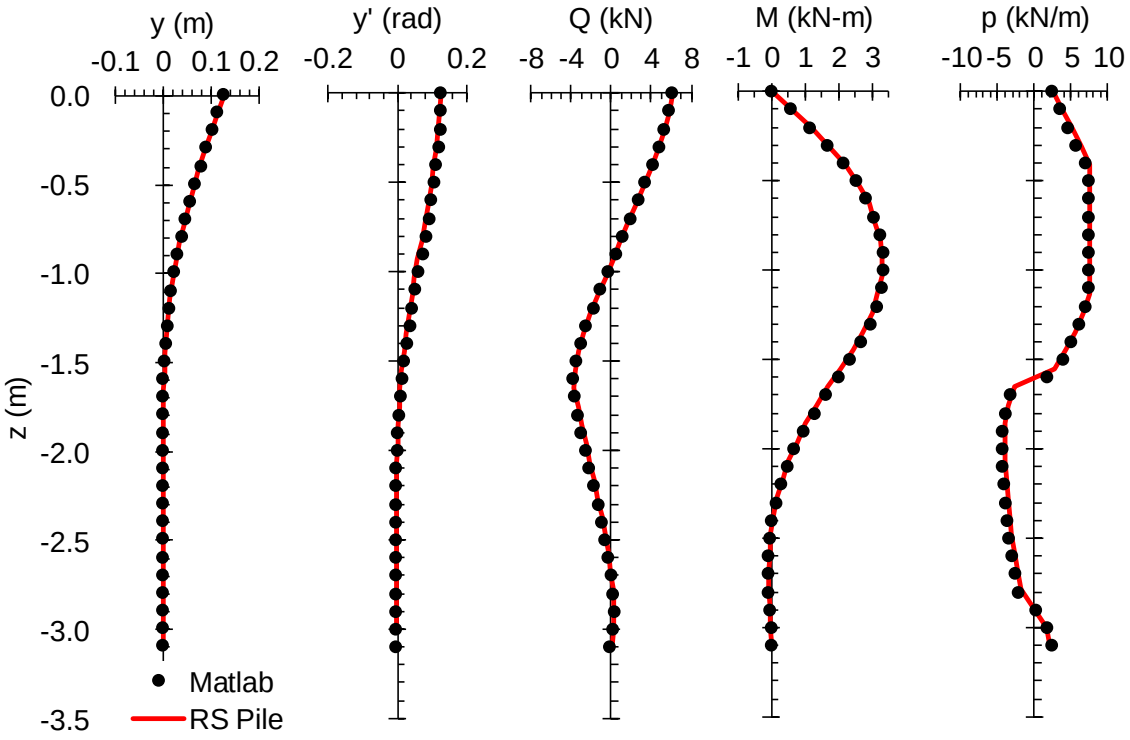

Figure 4.8. *p-y* analysis results from a commercial software (RSPile) and the one computed in Matlab using Low et al. (2001) methodology.

4.3 Reliability Analysis

Reliability analysis in civil engineering applications is an important tool that allows designers to evaluate how reliable the design condition will be, and to evaluate the sensitivity of designs to inherent uncertainties (e.g. soil and/or structural strength and stiffness, loading, etc.) associated with deterministic approaches to design (e.g., factors of safety). Additionally, it can be used to identify parameters and assumptions that are more influential on the performance of a system. The reliability index (β_R) is most often used to define the number of standard deviations, σ_g, a performance function (e.g. g= Capacity – Demand) is from the mean value, μ_g, to failure (Figure 4.9). Note that the subscript R on β is to differentiate the reliability index from the inclined loading angle. The probability of failure is computed using the reliability index as shown in Equation (4.8).

$$P_f = 1 - \Phi(\beta_R) \tag{4.8}$$

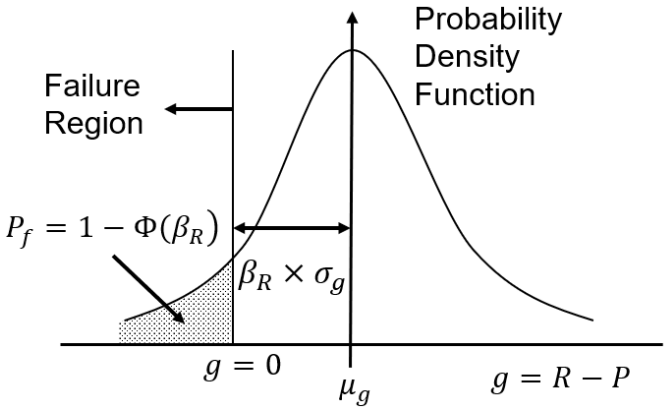

Figure 4.9. Representation of reliability Index with probability density function.

Multiple methods exist to evaluate β_R, Phoon and Ching (2015) presented some of them as Monte Carlos simulations, Taylor Series approximations, the Point-Estimate Method (PEM), and the Hasofer-Lind method. Each method has advantages and disadvantages, such as more rigorous and tedious calculations, or precision of the results. The use of the Taylor series is convenient with closed form solutions and the variance of the performance function can be easily evaluated using a series expansion. However, closed form solutions are not always available, thus the use of the other methods are preferred. The Hasofer-Lind method (Ditlevsen 1981, Madsen et al. 1986) computes the reliability index as:

$$\beta_R = \min_{x \in \mathrm{F}} \sqrt{(x-m)^T C^{-1} (x-m)} \tag{4.9}$$

or

$$\beta_R = \min_{x \in \mathrm{F}} \sqrt{\left(\frac{x-m}{\sigma}\right)^T \boldsymbol{R}^{-1} \left(\frac{x-m}{\sigma}\right)} \tag{4.10}$$

where x is a vector containing random variables, m is a vector of the mean values, C represents the covariance matrix, F represents the failure region, σ is the vector of standard deviations, and $\boldsymbol{R}$ is

the correlation matrix. The reliability index is interpreted as the shortest distance fro an origin of normalized (or transformed) variables to the failure region. Low and Tang (1997) assessed Equation (4.9) in the original coordinate space of random variables, interpreting the reliability index from an ellipsoid that effectively represents contours of a probability density function. When random variables are correlated, the ellipsoid is rotated. If a positive or negative correlation, ρ, between variables exists, the size of the ellipsoid decreases, as illustrated in Figure 4.10. With this elliptical approach, the reliability index is represented as the minimum β_R value between the center of the ellipse and the failure region (Figure 4.11). Low and Tang (1997) introduced a convenient approach to evaluate reliability using a built-in spreadsheet solver algorithm that minimizes the reliability index with constraints that enforce the performance function (i.e., the difference between resistance and capacity) to equal zero, which is representative of the ellipsoid being tangent to the failure region. Note that this approach has the potential to assess reliability in a multidimensional space where the elliptical shape is converted to an ellipsoid with multiple planes of variables.

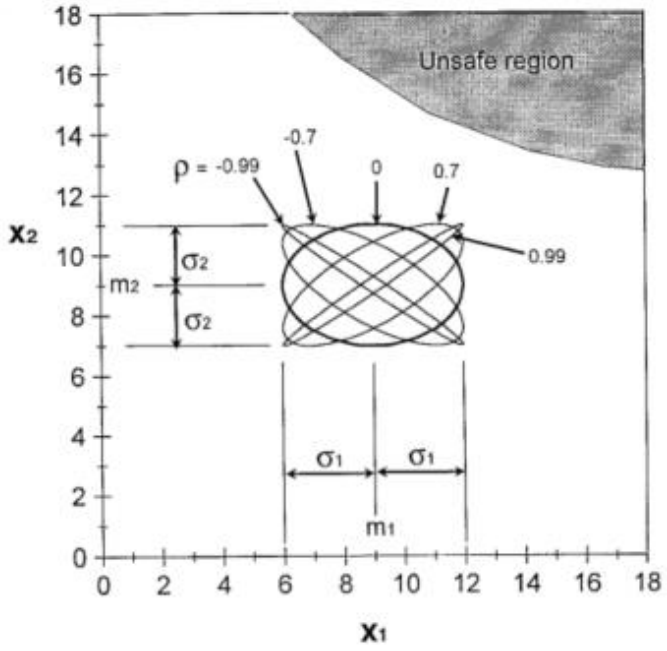

Figure 4.10. Low and Tang elliptical shape approximation and variation with the correlation coefficient (Low and Tang 1997).

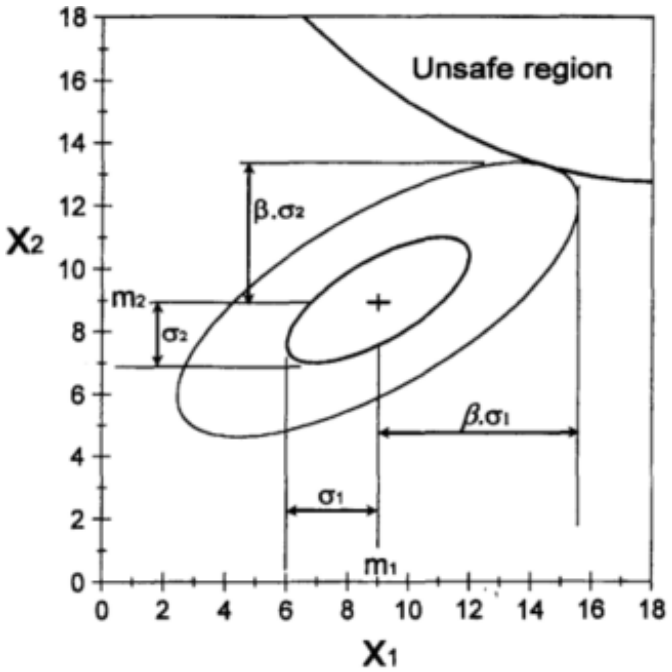

Figure 4.11. Low and Tang approximation to reliability using the Hasofer-Lind method using a positive correlation coefficient (Low and Tang 1997).

4.4 Reliability for Inclined Loading Conditions

The finite element analysis results presented in Chapter 3 provided insight to conveniently estimate the capacity of helical anchors at any inclined loading angle when the pure horizontal and vertical capacities are known (Figure 4.4). With this approach from Chapter 3 it is possible to conveniently assess the reliability of helical anchors for inclined loading that may be applied by an aquaculture mooring line. This section introduces a framework to apply the Hasofer-Lind method with an optimization tool presented by Low et al. (2001), considering random variables that may exist for both capacity and demand.

First, a performance function must be defined by Equation (4.11):

$$g(\boldsymbol{x}) = R(x_1, x_2, \dots, x_k) - P(x_1, x_2, \dots, x_j) = 0 \tag{4.11}$$

where R represents the capacity, and P represents the demand, both of which depend on a vector of random variables $\boldsymbol{x}$. Some variables (but not necessarily all) may influence both resistance and demand, as implied by Equation (4.11). A summary of possible random variables for both capacity

and demand are presented in Table 4.2 for helical anchors in soft clay. On the left-hand side the variables discussed in Chapter 3 are presented while on the right-hand side the demand variables discussed in Chapter 2 are presented. It is recognized by both geotechnical engineers and marine hydrodynamics engineers that for estimation of both capacity and demand, epistemic uncertainties associated with the capability of the calculation models to predict real behavior exist. However, it is still hard to quantifying these uncertainties, and beyond the scope of this work. This chapter focuses on developing a framework that may be used by practitioners when uncertainties associated with evaluation of capacity and demand are known or can at least be reasonably estimated.

Table 4.2. Possible random variables to consider in capacity and demand of helical anchors in soft clay for aquaculture applications.

Capacity, *R*	**Demand, *P***
Depends on internal random variables influenced by soil/anchor properties. Soil random variables could be: • Undrained shear strength, S_u. • Undrained stiffness modulus, E • Effective unit weight, γ' • Preconsolidation pressure, σ_p' • Anchor yielding stress, f_y. • Change in section properties of the anchor (e.g. corrosion). • Load rate. • Morphologic changes and bathymetry (e.g. seabed erosion)	Depends on environmental (metocean and geologic) and structural properties influencing the mooring system and morphologic changes that may modify the load inclination angle, β. Some of these random variables are: • Wind velocity, direction and frequency • Current velocity, patterns, and distributions (e.g, mixing) • Wave height, period, frequency and direction. • Temporal tidal fluctuations. • Aquaculture species (e.g., seaweed, shellfish, finfish). • Aquaculture farming systems (e.g., cages, longlines, rafts) • Net biofouling. • Boat wakes. • Morphologic changes and bathymetry (e.g. seabed erosion)

As mentioned, quantifying all the uncertainties associated with inputs to estimate capacity and demand is beyond the scope of this work. A simplified set of random variables for capacity and demand are assumed to demonstrate their potential influence on the reliability (probability of failure) of a helical anchor and the framework in which they are considered. These variables include the undrained shear strength s_u, the magnitude of the load P, and the load inclination angle β. Here random variables are assumed to be normally distributed with mean μ and standard deviation σ. The associated vectors and matrices appear as:

$$\boldsymbol{x} = \begin{bmatrix} P \\ s_u \end{bmatrix}, m = \begin{bmatrix} \mu_P \\ \mu_{s_u} \end{bmatrix}, \sigma = \begin{bmatrix} \sigma_P \\ \sigma_{s_u} \end{bmatrix}, \boldsymbol{R} = \begin{bmatrix} 1 & 0 \\ 0 & 1 \end{bmatrix}$$

where the capacity is computed as presented in Equation (3.6), considering the p-y analysis for lateral capacity and the bearing capacity factors for vertical capacity (e.g., Merifield 2011).

Low et al. (2001) computed the reliability of piles under pure lateral loading, minimizing the reliability index by changing the capacity and demand random variables until satisfying a limiting condition (e.g., force or displacement) that can be used to develop a performance function. For inclined or lateral loading where horizontal capacity controls, this is a complex optimization process where nonlinear constraints are present and depend on a secondary optimization process (*p-y* analysis) to determine lateral capacity. Thus, Matlab's built-in solvers were used for optimization, and accuracy was addressed by enforcing the performance function and the sub-optimization routine to meet specified tolerances (e.g., $g(\boldsymbol{x}) < tol$). A schematic representation of the code chart flow is presented in Figure 4.12.

Table 4.3. Optimization framework to obtain reliability index using Hasofer-Lind Method.

$$minimize\ \beta_R(\boldsymbol{x}) \begin{cases} Subjec\ to: \\ g(x) = R(s_u, \beta) - P = 0 \end{cases}$$ By changing random variables: $$\boldsymbol{x} = \begin{bmatrix} P \\ s_u \end{bmatrix}$$
Objective function: $$\beta_R = \sqrt{\left(\frac{x-m}{\sigma}\right)^T R^{-1} \left(\frac{x-m}{\sigma}\right)}$$ where: $$m = \begin{bmatrix} \mu_P \\ \mu_{s_u} \end{bmatrix}, \sigma = \begin{bmatrix} \sigma_P \\ \sigma_{s_u} \end{bmatrix}, \boldsymbol{R} = \begin{bmatrix} 1 & 0 \\ 0 & 1 \end{bmatrix}$$
Performance function: $$g(\boldsymbol{x}) = R(s_u) - x_1$$

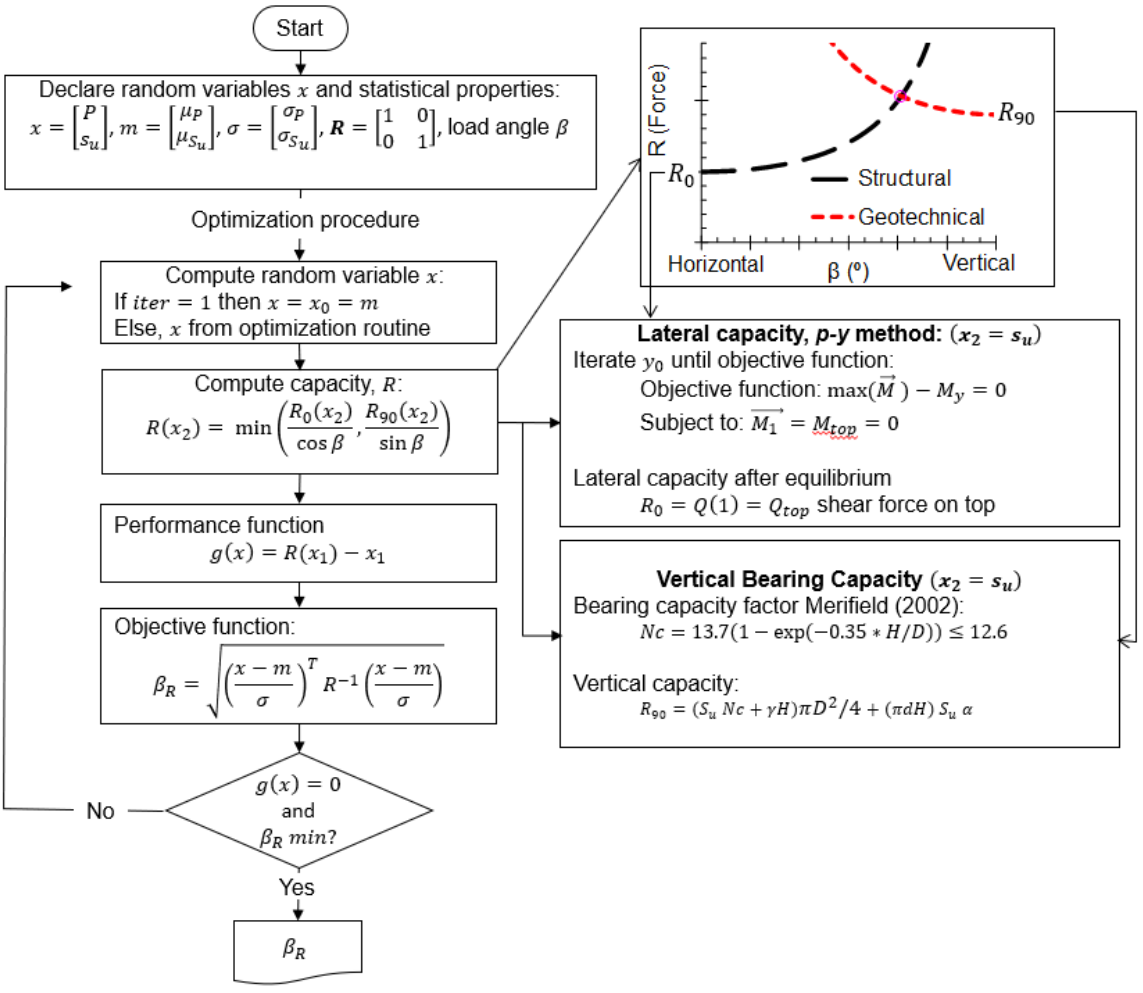

Figure 4.12. Flow diagram of the optimization code to compute the Hasofer-Lind reliability index for a helical anchor with random variables demand P and soil undrained shear strength s_u at a given load inclination angle.

4.5 Helical Anchor Reliability Assessment for an Oyster Aquaculture Farm

In this section, the reliability of an oyster farm, where mooring lines loads were measured by Nguyen et al. (2019) are used herein as an example to demonstrate the reliability framework previously presented. A summary of the farm layout and geologic profile is presented in Figure 4.13. The farm is located in the Damariscotta River estuary in Maine, where the tides influence load applied to taught mooring lines. The farm layout is presented by Nguyen et al. (2019), which had dimensions 94.5 m long and 140 m wide, from where 24 longlines (94.5m length), and 45 cages were attached to two main lines (140 m length). The mooring system of the main lines is composed of three 16 m length mooring ropes at each end and 3 intermediate ropes along the lines, to total 18 anchoring points. The mean water depth across the farm is approximately 2.5 m (Chandler, 2017), with variations of 1.0 and 1.5 m (Liu and Huguenard 2018 cited by Nguyen et al. 2019). Sediment near the farm location corresponds to cohesive Holocene and Pleistocene materials with thickness that varies between 2 and 7 m with some bedrock outcrops (Chandler, 2017).

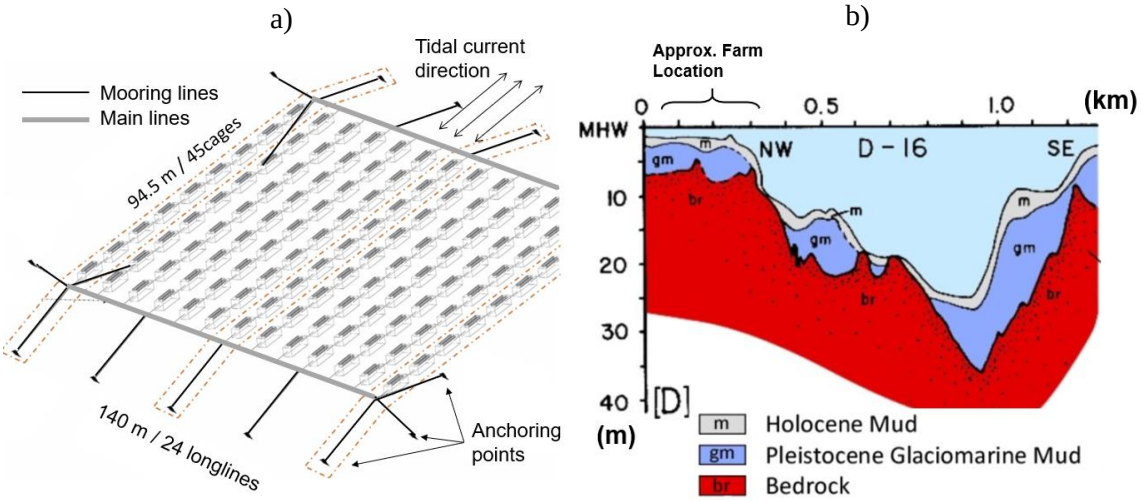

Figure 4.13. Aquaculture oyster farm in Damariscotta River Estuary, Maine: a) schematic representation (after Nguyen et al. 2019) and b) seabed geologic subsurface profile (after Chandler 2017).

4.5.1 Loading conditions:

Nguyen et al. (2019) studied the integrity of the mooring system under tidally influenced currents. They also evaluated extreme environmental conditions via development of a model to assess greater forces that may be imposed on the system. A sample of the measured loads is presented in Figure 2.17 (Chapter 2). After a complete analysis of the environmental forces acting on every farm component, Nguyen et al. (2019) calibrated their model to predict maximum mooring loads changing geometric properties and environmental metocean conditions. The predicted change in mooring load with changes in the mooring line length was also considered, as shown in Figure 4.14. Using the 2.5 m mean water depth to compute the load inclination angle, the relationship between the load and the angle can be developed and is presented in Figure 4.15. The maximum measured tensile mooring line load was $P = 3\ kN$, with a load inclination angle, $\beta = 9°$. Assuming that the anchors are helical anchors of 3.1 m length studied before in Figure 4.8 ($L = 3.1\ m$, $H = 3.0\ m$, $D = 0.254\ m$, $d = 0.038\ m$, $M_n = 3.35\ kN - m$, $EI = 35.12\ kN - m^2$) the reliability could be computed considering variability in soil resistance and loading conditions.

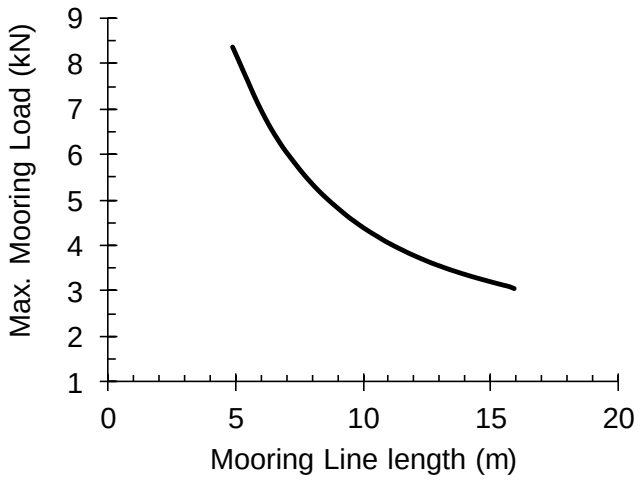

Figure 4.14. Estimated mooring loads vs. length of mooring line for an oyster aquaculture farm in the Damariscotta River Estuary (after Nguyen et al. 2019)

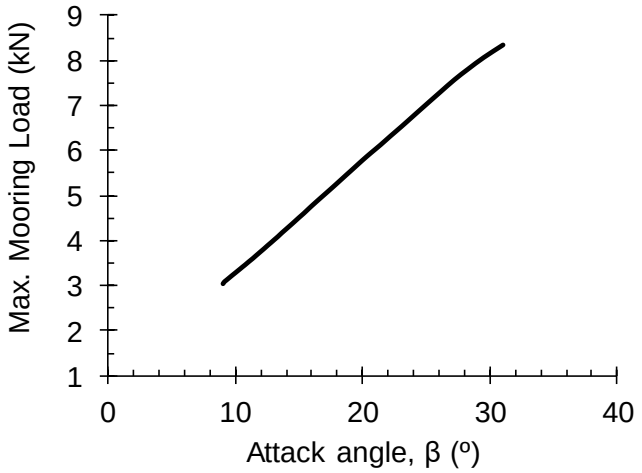

Figure 4.15. Estimated mooring loads vs. load inclination angle for an oyster aquaculture farm in the Damariscotta River Estuary interpreted from Nguyen et al. (2019)

4.5.2 Factor of Safety and Reliability at Current Working Conditions.

This subsection evaluates the factor of safety, reliability index and probability of failure of the studied example under the current maximum forces measured during Nguyen et al. (2019) deployment.

4.5.2.1 Current Factor of Safety

The factor of safety for the monitored working conditions for Nguyen et al. (2019) was evaluated using the anticipated demand and inclined angle, and a typical undrained shear strength (25 kPa) for these cohesive sediments. With this inclination angle the horizontal (structural) resistance controls capacity. As shown in Figure 4.8, the horizontal resistance is $R_0 = 6.15$ kN, which corresponds to a total resistance $R = 6.21\ kN$ at an inclination angle of 9º. Thus, the factor of safety for the current condition using Equation (4.12) is 2.1, which is within the values that may be relied on for some applications.

$$FS = \frac{R}{P} \tag{4.12}$$

4.5.2.2 Reliability

The factor of safety is a deterministic approach that does not consider uncertainties associated with available resistance and demand (P) on the anchor. The reliability and the probability of failure of the helical anchor is explored via a parametric study of assumed parameters and uncertainties. To compute the reliability index, the framework outlined in Table 4.3 is applied. A summary of the assumed initial mean values and coefficients of variation for the variables is presented in Table 4.4. The coefficient of variation COV for the load was determined based on the data presented by Nguyen et al. (2019) using the 3σ rule (Dai and Wang 1992) with Highest and Lowest Conceivable Values of $HCL = 3\ kN$ and $LCV = 1\ kN$, respectively. The chosen coefficient of variation for the undrained shear strength represents the mean value of this parameter reported by Phoon and Kulhawy (1999). The capacity and demand variables are assumed to be uncorrelated.

Table 4.4. Random variables analyzed during reliability assessment of helical anchors for Oyster aquaculture applications in the Damariscotta River Estuary, Maine.

Random variable	Mean, μ	COV
P (kN)	3	0.2
s_u (kPa)	25	0.2

Note: COV: Coefficient of variation σ/μ.

With these variables Equation (4.10) was optimized. As a result, a reliability index $\beta_R = 3.04$ was obtained, for which the probability of failure is P_f=0.0012. The results are on the lower limit target β_R values typically sought for deep foundations, which are 2.33 and 3.00 for redundant and non-redundant systems, respectively (Paikowsky et al. 2004).

4.5.3 Influence of Random Variables Mean Values on the Factor of Safety and Reliability

In this section the previous reliability example is assessed by changing factors that influence

demand and resistance of the anchor. The mean values of the mooring line load and the load inclination angle are changed based on the values presented in Figure 4.15, but the same COVs associated with variables considered in this analysis are maintained.

The factors of safety associated with the load inclination angle (mooring line length) and load applied at the anchor head are presented in Figure 4.16, where a critical loading condition (failure at $FS = 1.0$) is approached at load inclination angles greater than 22 degrees. Note that the horizontal load applied to the oyster farm itself, which is a function of environmental conditions (e.g., currents, tides, etc.), is unchanged. Changes in the mooring line length affect the magnitude and inclination of the load, which affects capacity or available resistance of the anchor. Though the total resistance of the anchor does increase with the load inclination angle (e.g., Figure 4.4), increases in the mooring line load are greater, and result in lower values of factor of safety. This illustrate the importance of considering mooring line inclination in combination with available resistance from the anchor.

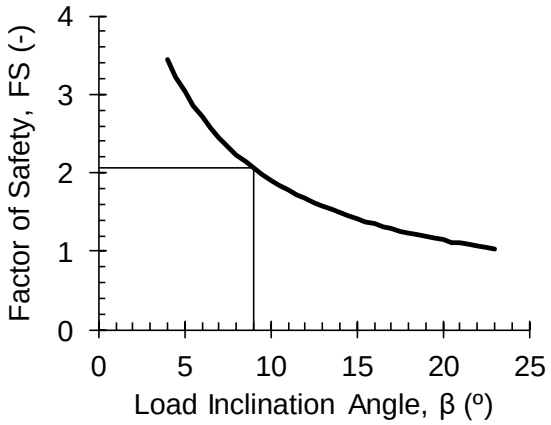

Figure 4.16. Change in factor of safety by changes in load inclination angle and load magnitude for a 3.1 m helical anchor on an oyster aquaculture farm in the Damariscotta River Estuary, Maine.

The reliability index for different load inclination angles is presented in Figure 4.17. At a load inclination angle greater than 9.5 degrees, $\beta_R < 3$, which is below targeted values under

normal working conditions are typically achieved for foundations. For the condition where factors of safety approaches one, the probability of failure is approximately 50%. During the numerical optimization process there were a few instances where the numerical algorithm did not converge to a solution. The optimization routine in combination with Matlab's solver can be sensitive to initial inputs (e.g. assumed initial deflections in the *p-y* analysis, or initial values of random variables considered in optimization of β_R). However, the optimization routine regularly converged in most instances to achieve a broad illustration of the effect of the load inclination angle (and other parameters evaluated later) have on the reliability index and associated probability of failure.

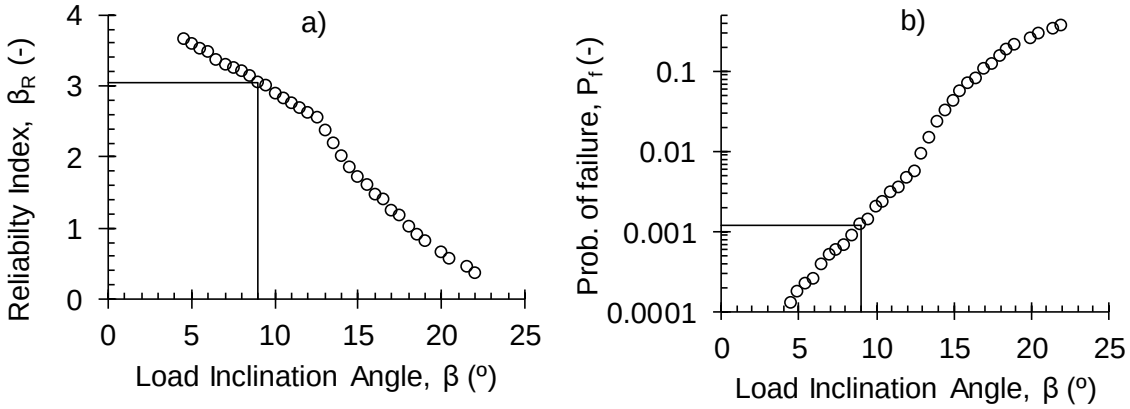

Figure 4.17. Effects of changes of the load inclination angle and the demand in: a) the reliability index, and b) probability of failure, for a 3.1 m helical anchor on an oyster aquaculture farm in the Damariscotta River Estuary, Maine.

The influence of undrained shear strength was evaluated by decreasing the assumed best estimate (mean value) to a value where the factor of safety equals 1. For this analysis, the load inclination angle remains at 9 degrees (appropriate for the farm monitored by Nguyen et al. 2019) and the same COV values are assumed. Figure 4.18 illustrates the changes in the factor of safety with undrained shear strength, where a limiting value of 9 kPa results in failure via deterministic predictions of the anchor capacity (i.e. $FS = 1.0$). In soft cohesive material the undrained shear strength is low and the anchor behaves as a "rigid" element and geotechnical capacity controls (i.e. plunging failure). When s_u increases, the anchor transitions to a "flexible" element as greater lateral

resistance is provided by the soil, and structural resistance of the anchor controls available resistance. This transition may be observed by the break in the curve shown in Figure 4.18.

Changes in the reliability index and probability of failure with undrained shear strength are presented in Figure 4.19. The lowest target reliability value is obtained when the mean value of undrained shear strength is below 19 kPa and target reliability index less than 3 is observed below a mean undrained shear strength of 20 kPa. This illustrates the importance of soil on reliability of a helical anchor performance within the mooring system.

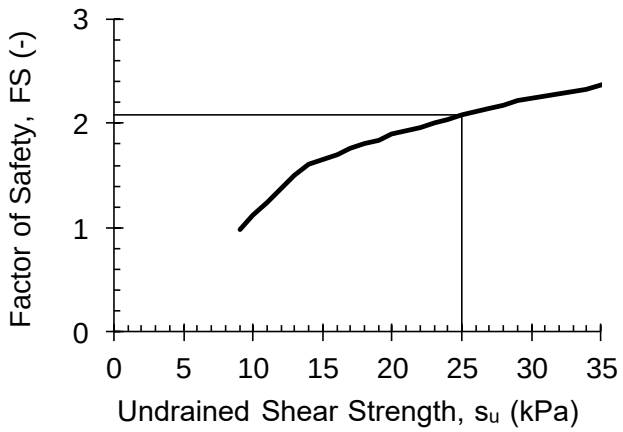

Figure 4.18. Change in factor of safety by changes in soil undrained shear strength for a 3.1 m helical anchor on an oyster aquaculture farm in the Damariscotta River Estuary, Maine.

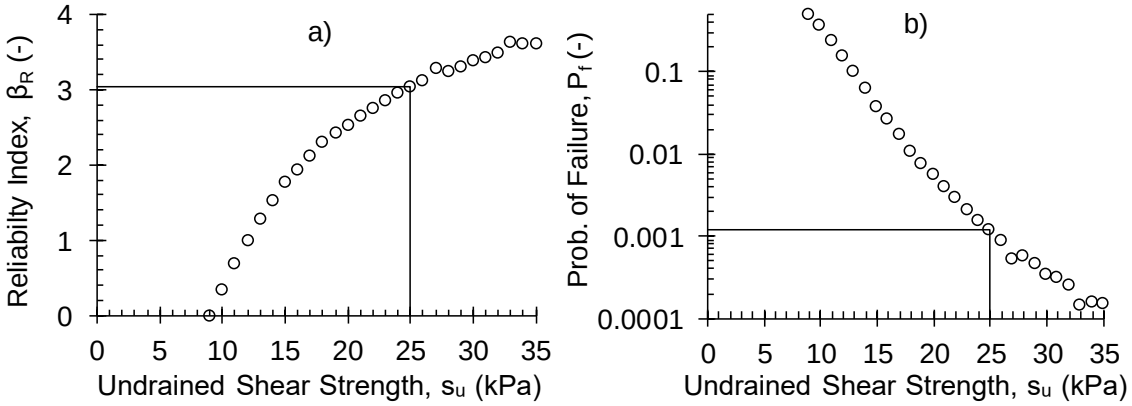

Figure 4.19. Effects of changes of soil undrained shear strength in: a) the reliability index, and b) probability of failure, for a 3.1 m helical anchor on an oyster aquaculture farm in the Damariscotta River Estuary, Maine.

4.5.4 Influence of uncertainty (COV) on the reliability of an anchoring system

The previous section was intended to illustrate the importance that certain changes in the mean value of random variables can play on reliability of the anchoring system. The sensitivity of uncertainty (using initial mean values) and its role in the evaluation of reliability to an aquaculture system is numerically investigated to demonstrate those random variables that have the greatest influence. The best estimates values (i.e., mean) presented in Table 4.4 are used and COV is varied. Knowing that the load inclination angle is a variable that can be reasonably controlled through design of an aquaculture system, its best estimate value of 9 degrees is used. Uncertainty of one variable is changed at a time while the others remain unchanged. Results are presented in Figure 4.20, which shows that uncertainties in undrained shear strength are much more critical to the system than the uncertainties in the demand load for the studied load inclination angle. This result gives an insight to the farmers where to increase the reliability of helical anchors for aquaculture farms, understanding the subsurface conditions is crucial.

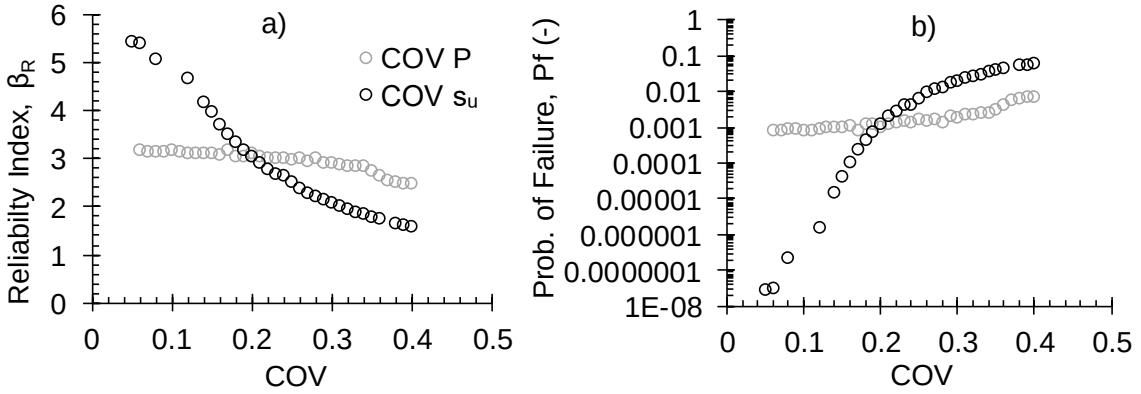

Figure 4.20. Effects of random variables uncertainties in the: a) reliability index, and b) probability of failure, of a 3.1 m helical anchor on an oyster aquaculture farm in the Damariscotta River Estuary, Maine.

4.6 Extending Reliability to a Broader Scenario

In the previous section, a reliability assessment example was addressed considering the demand load and the soil undrained shear strength as statistical variables for different constant inclined loading angles (i.e., statistical variability of this parameter was not included). The previous analyses considered demand load measured during working operation conditions in absence of extreme events. Extreme conditions as storm tidal or waves are scenarios that could be present in return periods in the order of decades, although a farm during its operation time may or may not experience such events. During these extreme conditions, changes in the demand load will occur as expected based on what it was presented in Chapter 2, as well as changes in the capacity due to multiple factors as seabed erosion, or the effect of a low frequency loading cycle in the soil undrained shear strength and stiffness degradation. With the methodology presented in section 4.4 such variables could be considered, by incorporating closed form solutions or numerical simulation results that relate metocean conditions to demand load, and by the modification of the pile eccentricity or soil parameters as part of the helical anchors analysis. Such analyses will need of both marine hydrodynamics and geotechnical background and perhaps the epistemic variabilities could be hard to consider as well. Thus, extended reliability analyses could be helpful to understand and evaluate critical variables during the mooring system and design of aquaculture farms.

4.7 Summary and Conclusions

A comparison between the 3D finite element calculations with a linear elastic soil and a simplified *p-y* analysis where soil nonlinearity is captured was presented for lateral loading. Such comparison allowed to perform a transition between the results from previous chapter and the alternative method presented to reconcile the failure envelop. A methodology to compute a *p-y* analysis without commercial software was presented and compared against this to demonstrate adequacy of the approach. Implementation of this methodology was important to conveniently perform reliability calculations of helical anchors. The *p-y* method was embedded within a

framework to compute the reliability index using the Hasofer-Lind method in a similar manner presented by Low et al. (2001). This method allows evaluation of multiple random variables Using this architecture the methodology was used to compute the reliability of a commercial anchor for an oyster aquaculture farm whose loads and bathymetry conditions were previously assessed. Though strength data for these sediments were unavailable, reasonable soil shear strengths and COVs were assumed from geologically similar sediments. Results indicated that: i) under the current loading conditions and the assumed anchor and soil properties, the anchoring system has a factor of safety equal 2 with a reliability index of 4.1, meaning that the probability of failure is very low, ii) when a combination of the load inclination angle the demand produced a factor of safety of 1.5, the system gets a target reliability value ($\beta_t = 3$) from where it is said that these foundations systems start being unreliable; iii) mean values of undrained shear strength lower than 20 kPa reduces the anchoring resistance to an unreliable level; and iv) uncertainties in the soil undrained shear strength are more critical than the uncertainties on the load value.

5 SUMMARY AND CONCLUSIONS

5.1 Summary

Aquaculture is an important industry in Maine looking to achieve more efficient mooring designs that will help accommodate and facilitate growth as this industry continues to mature. Helical anchor technology has the potential to resist lateral or inclined loading anticipated from aquaculture systems, and may be installed and decommissioned more efficiently than other anchors. Challenges include implementation of this efficient anchoring method in a reliable manner. This study was motivated by the paucity of performance data and design guidance available for lateral and inclined loading of helical anchors. Helical anchors consist of helical plates installed at depth. These plates are screwed into the ground and connected to a shaft element that extends to the surface of the seabed. These anchors generate resistance in soil via vertical movement of the plates and lateral movement of the shaft into the soil when inclined loads are applied. As soil around the shaft yields the structural capacity of the shaft is relied to resist the lateral component of inclined loads, especially at larger deformations.

Background on aquaculture systems was provided to understand the elements (e.g., finfish cages, mussel socks, oyster cages), farms arrangements, and mooring systems that are typically used in this industry. This provided a reference to anticipated loads helical anchors are required to resist. Multiple methods to predict the maximum mooring load were presented. A summary of the different mooring loads reported in the literature were also presented.

A review of the helical anchors was also provided, where previous studies and their performance under vertical, lateral and inclined loading were summarized. This chapter also introduced gaps in the knowledge base.

Chapter 3 presented a 3D finite element simulation of pullout for helical anchors to understand their capacity under inclined tensile loads. The influence of plate location, plate depth,

and soil properties were varied to: i) compare vertical capacities with values reported in the literature, ii) compute and understand lateral capacities and the effect of the shaft rigidity and the helical plate on capacity, iii) understand the interaction between mobilized soil resistance around the helical plate and the anchor shaft under inclined loads, and iv) investigate how the optimum inclination angles with changes in the soil properties and anchor geometry.

Chapter 4 introduced a framework to compute helical anchor reliability for inclined loading while computing lateral capacities with nonlinear p-y analysis. The use of this latter aspect allowed to perform reliability calculations in an efficient manner.

5.2 Conclusions

Based on the results and findings presented in this research, it is concluded that:

1. Vertical capacity of helical is proportional to the undrained shear strength in cohesive sediments when failure is defined by displacement criteria equal to 10% of the plate diameter. Changes in plate spacing also increase vertical capacity up to an optimum spacing ($S/D = 3$).

2. Lateral capacity of helical anchors is limited by the structural capacity due to yielding of the shaft in bending, except when the plate is installed at very shallow depths (e.g. H/D < 5.7). At shallow depths the anchor behaves as a “rigid” element and the helical plate rotates and the pullout capacity of the anchor (cylindrical shear for shallow anchors) controls

3. When lateral capacities are computed for soils with different soil stiffness but the same shear strength, at a given displacement, a higher soil stiffness represents a higher horizontal capacity. However, when compared to the shaft yielding limit, lower soil stiffness leads to lower soil reaction force, which reduces the curvature on the shaft

allowing it to develop more displacements before yielding. Such increase in displacement could lead to a higher mobilization of the anchor resistance. So even though a helical anchor in a stiffer soil could have higher lateral capacity for a certain displacement, this at the same time could have lower capacity at yielding levels when compared to a softer soil.

4. Presence of the helical plates can generate partial fixity of the element at shallower depths compared to a shaft or pile (i.e. no plate) with equivalent shaft dimensions. This partial fixity provided by the plate increases curvature in the shaft and causes it to yield at smaller displacements compared to a shaft with no plates. When the plate is substantially deep the shaft develops fixity above the plate and is considered flexible. Under these conditions the lateral capacity is not influenced by the plate and equivalent to a single pile or shaft of equivalent dimensions regardless of the plate depth.

5. During inclined loading greater resistances were simulated in the 3D finite element analyses as the load inclination angle approached vertical due to greater mobilization of geotechnical capacity at the plate.

6. An optimum inclination angle, defined as the angle where simultaneous geotechnical and structural failure is observed, was found to be between 60 and 90 degrees for the helical anchors simulated in the numerical simulations. Shafts with greater rigidity (i.e. low ratio of soil to shaft bending stiffness) have a lower optimum angle while anchors shafts that behave as a flexible element have a higher optimum angle.

7. Interaction of the mobilized resistances in the zones above the plate and along the shaft due to vertical uplift and lateral loading was found at all inclination angles for shallow ($H/D = 2.7$) helical anchors with a single plate, and at near optimum angles for the rest of the anchors. For single plate shallow ($H/D = 2.7$) rigid anchors, the overlap of

the mobilized shear strength above the plate and along the shaft reduced the vertical and lateral components of the inclined load when compared with pure vertical and horizontal capacities. For the rest of the anchors, horizontal and vertical components of the inclined load were similar, however, at yielding stages the interaction of the mentioned zones was present at angles close to the optimum. At these angles the effect of the overlap of shear zones in the shaft and the plate, softened the soil near the shaft, thus an effect as explained in the previous conclusion happened, where the soil has less reaction, thus allows the anchor to displace more before reaching yielding. Such increase in displacement is then translated as an increase in capacities.

8. The capacity at any inclined angle can by defined accurately by the failure envelope via prediction pure lateral and vertical capacities. The accuracy of this methodology is reduced when the inclined angle is close to the optimum angle but in the structural side, where the effect mentioned in the previous conclusion it is expected.

9. In a reliability analysis for a helical anchor supporting an oyster aquaculture farm in Maine, structural resistance controlled the available capacity provided by the anchor. In this simplified analysis the load magnitude, load angle, and undrained shear strength were considered random variables with some uncertainty. It was found that under operational loads, and typical soil conditions at this site, commercially available small shaft helical anchors can support in a safe and reliable manner the loads imposed from this kind of aquaculture farms. When best estimates of load inclination and soil resistance changes, it is important to verify that the anchoring system is in a safe condition. Both demand and resistance increase with the inclination angle, however, as for the studied case, the demand increases at a higher rate. It was also found that uncertainty associated with the undrained shear strength had the greatest influence on the reliability index than the mooring line load. This implies that for aquaculture

farmers have a more reliable, and thus resilient, anchoring system, it is necessary to have a more confidence on the subsurface conditions during early stages of design.

5.3 Recommendations for Future Work

1. The research performed herein intended to be thoughtful about the results obtained during the numerical simulations and additional calculations. Nevertheless, the performance of a field test on helical anchors under inclined loads will be ideal to:
    - Validate proposed failure criteria under inclined loading.
    - Validate numerical simulations of helical anchors reconciling installation effects
    - and how this will affect the proposed envelope.
    - Verify if the aquaculture cyclic loading reduces or increases the capacity, reconciling what are the effects of this type of loading on the stiffness degradation.
2. From an analytical perspective, the inclusion of rotational spring on the finite difference model will help to predict lateral capacity for inclined loading inclination angles.
3. The statistical variance of the inclined loading attack angle can also be considered in the reliability framework to address this problem in a multivariable manner. However, further uncertainties of these variables should be addressed and reconciled before.
4. Reliability assessment of helical anchors for extreme conditions could also be addressed by combining long term effects of soil reaction with external loads.

REFERENCES

Abdelghany, Y. (2008). "Monotonic and cyclic behavior of helical screw piles." PhD Thesis, The University of Western Ontario.

Abdelghany, Y., and El Naggar, H. (2016). "Helical screw piles performance – A versatile efficient foundation system alternative for rehabilitation, new unsustainable structures construction and infrastructure delivery." Second International Conference on Infrastructure Management, Assessment and Rehabilitation Techniques.

Abdelghany, Y., and El Naggar, M. H. (2010). "Monotonic and cyclic behavior of helical screw piles under axial and lateral loading." Recent Advances in Geotechnical Earthquake Engineering and Soil Dynamics, (9).

Abdrabbo, F. M., and El Wakil, A. Z. (2016). "Laterally loaded helical piles in sand." Alexandria Engineering Journal, Faculty of Engineering, Alexandria University, 55(4), 3239–3245.

Achmus, M., Abdel-Rahman, K., and Thieken, K. (2009). "Behavior of piles in sand subjected to inclined loads." 1st Int. Symp. on Computational Geomechanics (ComGeo I), 763–774.

Adams, J. I., and Klym, T. W. (1972). "A study of anchorages for transmission tower foundations." Canadian Geotechnical Journal, 9(1), 89–104.

Al-Baghdadi, T. A., Brown, M. J., Knappett, J. A., and Al-Defae, A. H. (2017). "Effects of vertical loading on lateral screw pile performance." Proceedings of the Institution of Civil Engineers - Geotechnical Engineering, 170(3), 259–272.

Al-Baghdadi, T. A., Brown, M. J., Knappett, J. A., and Ishikura, R. (2015). "Modelling of laterally loaded screw piles with large helical plates in sand." Frontiers in Offshore Geotechnics III, 978–1.

Aubeny, C. P., and Chi, C.-M. (2010). "Mechanics of drag embedment anchors in a soft seabed." J. Geotech. and Geoenviron. Eng., 136(January), 57–68.

Bagheri, F., and El Naggar, M. H. (2015). "Effects of installation disturbance on behavior of multi-helix piles in structured clays." DFI Journal - The Journal of the Deep Foundations Institute, 9(2), 80–91.

Balash, C., Colbourne, B., Bose, N., and Raman-Nair, W. (2009). "Aquaculture Net Drag Force and Added Mass." Aquacultural Engineering, 41(1), 14–21.

Bathe, K. J. (2014). Finite Element Procedures. Prentice Hall, Pearson Education, Inc.

Brinch-Hansen, J. (1963). "Discussion on hyperbolic stress-strain response: Cohesive soils." Journal of the Soil Mechanics and Foundation Division, 89, 241–242.

Brinkgreve, R., Kumarswamy, S., Swolfs, W., Zampich, L., and Manoj, R. (2017). "Plaxis 2017 manuals." Delft: Plaxis bv / Bentley systems.

Broms, B. B. (1964). “Lateral resistance of piles in cohesive soils.” Journal of the Soil Mechanics and Foundation Division: proceedings of the American Society of Civil Engineers, 90(2), 27–64.

Buck, B. H., and Bucholz, C. M. (2004). “The offshore-ring: A new system design for the open ocean aquaculture of macroalage.” Journal of Applied Phycology, 16, 355–368.

Byrne, B. W., and Houlsby, G. T. (2015). “Helical piles: an innovative foundation design option for offshore wind turbines.” Philosophical Transactions of the Royal Society A, 373, 1–11.

Cardia, F., and Lovatelli, A. (2015). Aquaculture operations in floating HDPE cages: a field handbook. FAO Fisheries and Aquaculture Technical Paper.

Catalina Sea Ranch. (n.d.). “Catalina Sea Ranch.” <https://catalinasearanch.com/> (Dec. 23, 2018).

Celikkol, B., DeCew, J., Baldwin, K., Boduch, S., Chambers, M., Fredriksson, D. W., Irish, J., Paturssonb, O., Rice, G., Swift, M. R., Tsukrov, I., and Turmelle, C. A. (2006). “Engineering overview of the University of New Hampshire’s open ocean aquaculture project.” Oceans 2006, IEEE.

Cerato, A. B., and Victor, R. (2009). “Effects of long-term dynamic loading and fluctuating water table on helical anchor performance for small wind tower foundations.” Journal of Performance of Constructed Facilities, 23(August), 251–261.

Chandler, E. A. (2017). “Sediment Accumulations Patterns in the Damariscotta River Estuary.” Electronic Theses and Dissertations. 2470. https://digitalcommons.library.umaine.edu/etd/2470.

Chari, T. R., and Meyerhof, G. G. (1983). “Ultimate capacity of rigid single piles under inclined loads in sand.” Canadian Geotechnical Journal, 20(4), 849–854.

Clark, D., Lee, K., Murphy, K., and Windrope, A. (2018). “2017 Cypress Island Atlantic Salmon net pen failure: An investigation and review.” Washington Department of Natural Resources, Olympia, WA. This.

Colbourne, D. B., and Allen, J. H. (2000). “Observations on motions and loads in aquaculture cages from full scale and model scale measurements.” Aquacultural Engineering, 24, 129–148.

Cole, A., Langston, A., and Davis, C. (2017). Maine Aquaculture: Economic Impact Report.

Conte, E., Troncone, A., and Vena, M. (2015). “Behaviour of flexible piles subjected to inclined loads.” Computers and Geotechnics, Elsevier Ltd, 69, 199–209.

Dai, S.-H., and Wang, M. O. (1992). Reliability analysis in engineering applications. Van Nostrand Reinhold, New York.

DeCew, J., Fredriksson, D. W., Bugrov, L., Swift, M. R., Eroshkin, O., and Celikkol, B. (2005). “A case study of a modified gravity type cage and mooring system using numerical and physical models.” IEEE Journal of Oceanic Engineering, 30(1), 47–58.

Decourt, L. (1999). “Behavior of foundations under working load conditions.” Proceedings of the 11th Pan-American Conference on Soil Mechanics and Geotechnical Engineering, Foz do Iguassu, Brazil, 453–458.

Ditlevsen, O. (1981). Uncertainty modeling: With applications to multidimensional civil engineering systems. McGraw-Hill, New York.

Dong, T. W., and Zheng, Y. R. (2015). “Experiment of single screw piles under inclined cyclic pulling loading.” Geomechanics and Engineering, 8(6), 801–810.

Drach, A., Tsukrov, I., DeCew, J., and Celikkol, B. (2016). “Engineering procedures for design and analysis of submersible fish cages with copper netting for exposed marine environment.” Aquacultural Engineering, Elsevier B.V., 70, 1–14.

FMS. (2018). “FIELDER MARINE SERVICES.” <https://www.fieldermarine.com/> (Dec. 23, 2018).

Fredriksson, D. W., DeCew, J. C., and Irish, J. D. (2006). “A field study to understand the currents and loads of a near shore finfish farm.” OCEANS 2006, IEEE, 1–9.

Fredriksson, D. W., DeCew, J. C., Tsukrov, I., Swift, M. R., and Irish, J. D. (2007). “Development of large fish farm numerical modeling techniques with in situ mooring tension comparisons.” Aquacultural Engineering, 36, 137–148.

Fredriksson, D. W., DeCew, J., Swift, M. R., Tsukrov, I., Chambers, M. D., and Celikkol, B. (2004). “The design and analysis of a four-cage grid mooring for open ocean aquaculture.” Aquacultural Engineering, 32, 77–94.

Fredriksson, D. W., Swift, M. R., Muller, E., Baldwin, K., and Celikkol, B. (2000). “Open ocean aquaculture engineering: System design and physical modeling.” Marine Technology Society Journal, 34(1), 41–52.

Fredriksson, D. W., Tsukrov, I., and Hudson, P. (2008). “Engineering investigation of design procedures for closed containment marine aquaculture systems.” Aquacultural Engineering, 39, 91–102.

Gagnon, M., and Bergeron, P. (2017). “Observations of the loading and motion of a submerged mussel longline at an open ocean site.” Aquacultural Engineering, Elsevier, 78(June), 114–129.

Gaudin, C., O’Loughlin, C. D., Randolph, M. F., Cassidy, M. J., Wang, D., Tian, Y., Hambleton, J. P., and Merifield, R. S. (2014). “Advances in offshore and onshore anchoring solutions.” Australian Geomechanics Journal, 49(4), 59–71.

George, B. E., Banerjee, S., and Gandhi, S. R. (2017). “Numerical analysis of helical piles in cohesionless soil.” International Journal of Geotechnical Engineering, Taylor & Francis, 1–15.

Hafbor. (n.d.). “Hafbor Offshore Anchor System.” <http://www.hafbor.is/> (Dec. 23, 2018).

Helix Mooring Systems. (2016). “Round Shaft Anchors | Helix Mooring Anchor Types.” <https://helixmooring.com/round-shaft-anchors/> (Jun. 7, 2018).

Houlsby, G. T. (2016). “Interactions in offshore foundation design.” Géotechnique, 66(10), 791–825.

Hoyt, R. ., and Clemence, S. P. (1989). “Uplift capacity of helical anchors in soil.” 12th International Conference on Soil Mechanics and Foundation Engineering, 1019–1022.

Huang, C. C., Tang, H. J., and Pan, J. Y. (2009). “Numerical modeling of a single-point mooring cage with a frontal rigid frame.” IEEE Journal of Oceanic Engineering, 34(2), 113–122.

Hubell/CHANCE. (2014). “ATLAS Technical Design Manual, Edition 3.”

IBC. (2015). “International Building Code. CHAPTER 18 SOILS AND FOUNDATIONS | 2015 International Building Code | ICC public ACCESS.” <https://codes.iccsafe.org/public/document/IBC2015/chapter-18-soils-and-foundations> (Jun. 13, 2018).

ICC-ES. (2007). “AC358 Acceptance criteria for helical pile foundations and devices.” www.icc-es.org.

International Code Council. (2009). International Building Code 2009. International Building Code, International Code Council.

Irish, J., Carroll, M., Singer, R., Newhall, A., Paul, W., Johnson, C., Witzell, N., Rice, G., and Fredriksson, D. W. (2001). WHOI-2001-15. Instrumentation for Open Ocean Aquaculture Monitoring.

Kim, T., Lee, J., Fredriksson, D. W., DeCew, J., Drach, A., and Moon, K. (2014). “Engineering analysis of a submersible abalone aquaculture cage system for deployment in exposed marine environments.” Aquacultural Engineering, Elsevier B.V., 63, 72–88.

Koumoto, T., Meyerhof, G. G., and Sastry, V. V. R. N. (1986). “Analysis of bearing capacity of rigid piles under eccentric and inclined loads.” Canadian Geotechnical Journal, 23(2), 127–131.

Kurian, N. P., and Shah, S. J. (2009). “Studies on the behaviour of screw piles by the finite element method.” Canadian Geotechnical Journal, 46, 627–638.

Lanyi-Bennett, S. A., and Deng, L. (2018). “Axial load testing of helical pile groups in a glaciolacustrine clay.” Canadian Geotechnical Journal.

Lekang, O. I. (2008). Aquaculture engineering. John Wiley & Sons.

Li, W., Zhang, D. J. Y., Sego, D. C., and Deng, L. (2018). “Field testing of axial performance of large-diameter helical piles at two soil sites.” Journal of Geotechnical and Geoenvironmental Engineering, 144(2012), 2–6.

Li, Z., Kotronis, P., and Escoffier, S. (2014). “Numerical study of the 3D failure envelope of a single pile in sand.” Computers and Geotechnics, Elsevier Ltd, 62, 11–26.

Livneh, B., and El Naggar, M. H. (2008). “Axial testing and numerical modeling of square shaft helical piles under compressive and tensile loading.” Canadian Geotechnical Journal, 45(8), 1142–1155.

Løland, G. (1991). “Current forces on and flow through fish farms (Ph.D. thesis).” University of Trondheim.

Løland, G. (1993). “Current forces on, and water flow through and around, floating fish farms.” Aquaculture International, 1(1), 72–89.

Low, B. K., and Tang, W. H. (1997). “Efficient reliability evaluation using spreadsheet.” Journal of Engineering Mechanics, 123(July), 749–752.

Low, B. K., Teh, C. I., and Tang, W. H. (2001). “Stochastic nonlinear p-y analysis of laterally loaded piles.” Eight International Conference on Structural Safety and Reliability (ICOSSAR), 17–22.

Lutenegger, A. J. (2008). “Tension tests on single-helix screw-piles in clay.” Proceedings of the second BGA International Conference on Foundations2, 201–212.

Lutenegger, A. J. (2009). “Cylindrical shear or plate bearing? — Uplift behavior of multi-helix screw anchors in clay.” Contemporary Topics in Deep Foundations, 456–463.

Lutenegger, A. J. (2011). “Historical development of iron screw-pile foundations: 1836–1900.” The International Journal for the History of Engineering & Technology, 81(1), 108–128.

Lutenegger, A. J. (2017). “Support of offshore structures using helical anchors.”

Madsen, H. O., Krenk, S., and Lind, N. C. (1986). Methods of structural safety. Prentice-Hall, Englewood Cliffs, N.J.

Magnum. (2016). “MAGNUM CATALOG 2016 Rev. 7-15-16.”

Maine Sea Grant. (n.d.). “Aquaculture Methods.” <https://www.seagrant.umaine.edu/aquaculture/resources-for-shellfish-growers/aquaculture-methods-guide> (Dec. 23, 2018).

Matlock, H. (1970). “Correlations for design of laterally loaded piles in soft clay.” Offshore technology in civil engineering’s hall of fame papers from the early years, 77–94.

Menicou, M., Vassiliou, V., Charalambides, M., Tsukrov, I., and Decew, J. (2012). “Engineering challenges for sustainable coastal cage aquaculture.” Recent researches in energy, environment and sustainable development, 150–155.

Merifield, R. S. (2011). “Ultimate uplift capacity of multiplate helical type anchors in clay.” Journal of Geotechnical and Geoenvironmental Engineering, 137(7), 704–716.

Merifield, R. S., Lyamin, A. V., Sloan, S. W., and Yu, H. S. (2003). “Three-dimensional lower-bound solutions for stability of plate anchors in Clay.” Journal of Geotechnical and Geoenvironmental Engineering, 129(March), 243–253.

Meyerhof, G. G. (1951). “The ultimate bearing capacity of foundations.” Geotechnique, 2.

Meyerhof, G. G., and Adams, J. I. (1968). “The ultimate uplift capacity of foundations.” Canadian Geotechnical Journal, 5(4), 225–244.

Meyerhof, G. G., and Sastry, V. V. R. N. (1985). “Bearing capacity of rigid piles under eccentric and inclined loads.” Canadian Geotechnical Journal, 22(3), 267–276.

Mitsch, M. P., and Clemence, S. P. (1985). “Mitsch and Clemence (1985). The uplift capacity of helix anchors in sand.” Uplift Behavior of Anchor Foundations in Soil, S. P. Clemence, ed., Detroit, Michigan, 26–47.

Mittal, S., Ganjoo, B., and Shekhar, S. (2010). “Static equilibrium of screw anchor pile under lateral load in sands.” Geotechnical and Geological Engineering, 28(5), 717–725.

Mohajerani, A., Bosnjak, D., and Bromwich, D. (2016). “Analysis and design methods of screw piles: A review.” Soils and Foundations, Elsevier, 56(1), 115–128.

Mooney, J. S., Adamczak, S. J., and Clemence, S. P. (1985). “Uplift capacity of helical anchors in clay and silt.” Uplift Behavior of Anchor Foundations in Soil, S. P. Clemence, ed., Detroit, Michigan, 48–72.

Morison, J. R., Johnson, J. W., and Schaaf, S. A. (1950). “The force exerted by surface waves on piles.” Journal of Petroleum Technology, Society of Petroleum Engineers, 2(05), 149–154.

Nagata, M., and Hirata, H. (2005). Study on Uplift Resistance of Screwed Steel Pile.

Narasimha Rao, S., and Prasad, Y. V. S. N. (1993). “Estimation of uplift capacity of helical anchors in clays.” Journal of Geotechical Engineering, 119(2), 352–357.

Narasimha Rao, S., Prasad, Y. V. S. N., and Shetty, D. (1991). “The behavior of model screw piles in cohesive soils.” Soils and Foundations, 31(June), 35–50.

Nguyen, N. Q., Thiagarajan, K., and Auger, J. (2019). “Integrity assessment of an oyster farm mooring system through in-situ measurements and extreme environment modeling.” Ocean Engineering, 172(October 2018), 641–659.

Nguyen, N., Sharman, K. T., and Auger, J. (2018). “Integrity assessment of an oyster farm mooring system through in-situ measurements and extreme environment modeling.” Journal of Ocean Engineering, Submitted.

Olanrewaju, S. O., Magee, A., Kader, A. S. A., and Tee, K. F. (2017). “Simulation of offshore aquaculture system for macro algae (seaweed) oceanic farming.” Ships and Offshore Structures, 12(4), 553–562.

Paikowsky, S. G., and et al. (2004). “Load and resistance factor design (LRFD) for deep foundations.” 126. NCHRP Rep. 507. Washington, DC: Transportation Research Board.

Papadopoulou, K., Saroglou, H., and Papadopoulos, V. (2014). “Finite element analyses and experimental investigation of helical micropiles.” Geotechnical and Geological Engineering, 32(4), 949–963.

Perko, H. A. (2000). “Energy method for predicting installation of helical foundations and anchors.” Geo-Denver: New technological and design developments in deep foundations, 342–352.

Perko, H. A. (2009). Helical piles: a practical guide to design and installation. John Wiley & Sons.

Phoon, K., and Ching, J. (2015). Risk and Reliability in Geotechnical Engineering. CRC Press.

Phoon, K., and Kulhawy, F. H. (1999). “Characterization of geotechnical variability.” Canadian Geotechnical Journal, 36, 612–624.

Poulos, H. G., and Hull, T. (1989). “The role of analytical geomechanics in foundation engineering.” Foundation Engineering: Current principles and Practices, ASCE, Reston, 2, 1578–1606.

Prasad, Y. V. S. N., and Narasimha Rao, S. (1994a). “Pullout behaviour of model pile and helical pile anchors subjected to lateral cyclic loading.” Canadian Geotechnical Journal, 31, 110–119.

Prasad, Y. V. S. N., and Narasimha Rao, S. (1994b). “Experimental studies on foundations of compliant structures-II. Under cyclic loading.” Ocean Engineering, 21(1), 15–27.

Prasad, Y. V. S. N., and Narasimha Rao, S. (1996). “Prasad and Rao (1996), Lateral capacity of helical piles in clay.pdf.” Journal of Geotechical Engineering, 122(11).

Puri, V. K., Stephenson, R. W., Dziedzic, E., and Goen, L. (1984). “Helical anchor piles under lateral loading.” Laterally Loaded Deep Foundations: Analysis and Performance. ASTM STP 835, 194–213.

Randolph, M., and Gourvenec, S. (2011). Offshore geotechnical engineering. Taylor & Francis e-Library.

Reape, D., and Naughton, P. J. (2018). “An experimental investigation of helical piles subject to inclined pullout loads.” CERI-ITRN, 235–240.

Reese, L. C., Cox, W. R., and Koop, F. D. (1975). “Field testing and analysis of laterally loaded piles in stiff clay.” Proceedings of the VII Annual Offshore Technology Conference, Houston, Texas, 2(OTC 2312), 672–690.

Rocscience. (2018). “RSPILe User Manual: Laterally Loaded Piles.” www.rocscience.com.

Rudi, H., Aarsnes, J. V., and Dahle, L. A. (1998). “Environmental forces on a floating cage system, mooring considerations.” IChemE Symposium Series No. 11, 97–122.

Sakr, M. (2010a). “High capacity helical piles-A new dimension for bridge foundations.” 8th International Conference on Short and Medium Span Bridges, 142 (1–11).

Sakr, M. (2010b). “Lateral Resistance of high capacity helical piles – Case study.” 63rd Canadian Geotechnical Conference & 6th Canadian Permafrost Conference, 405–413.

Sakr, M., Nazir, A. K., Azzam, W. R., and Sallam, A. F. (2016). “Behavior of grouted single screw piles under inclined tensile loads in sand.” Electronic Journal of Geotechnical Engineering, 21(2), 571–592.

Singh, S., and Bhardwaj, S. K. (2015). “Influence of load obliquity on pullout capacity of micropile in sand.” Indian Geotechnical Journal, Springer India, 45(June), 200–208.

Skempton, A. W. (1951). “The Bearing Capacity of Clays.” Proceedings of the Building Research Congress, 180–189.

Spagnoli, G., and Gavin, K. (2015). “Helical piles as a novel foundation system for offshore piled facilities.” Abu Dhabi International Petroleum Exhibition and Conference, (November), 9–12.

Stanier, S. A., Black, J. A., and Hird, C. C. (2013). “Modelling helical screw piles in soft clay and design implications.” Proceedings of the Institution of Civil Engineers-Geotechnical Engineering, 167(5), 447–460.

Stevens, C., Plew, D., Hartstein, N., and Fredriksson, D. W. (2008). “The physics of open-water shellfish aquaculture.” Aquacultural Engineering, 38(3), 145–160.

Stuedlein, A. W., and Uzielli, M. (2014). “Serviceability limit state design for uplift of helical anchors in clay.” Geomechanics and Geoengineering, Taylor & Francis, 9(3), 173–186.

Sulaiman, O., Kader, A., Magee, A., and Othman, K. (2015). “Mooring analysis of offshore aquaculture oceanic farming platform for seaweed.” Journal of Coastal Zone Management, 18(2).

The MathWorks. (2018). “MATLAB Optimization Toolbox.” Natick, MA, USA.

Turner, R. (2000). “Offshore mariculture: Mooring system design.” Mediterranean offshore mariculture, 159–172.

Vassiliou, V., Menicou, M., Charalambides, M., DeCew, J., and Tsukrov, I. (2012). “Cyprus ’ offshore aquaculture mooring systems: Current status and future development.” International Journal of Biological, Biomolecular, Agricultural, Food and Biotechnological Engineering, 6(7), 411–416.

Vhryhof. (2018). “Vhryhof Manual: The guide to anchoring.”

Wang, D., Gaudin, C., Merifield, R. S., and Hu, Y. (2010). “Centrifuge model tests of helical anchors in clay.” Physical Modelling in Geotechnics, 1069–1074.

Wang, D., Merifield, R. S., and Gaudin, C. (2013). “Uplift behaviour of helical anchors in clay.” Canadian Geotechnical Journal, 50(6), 575–584.

Weech, C. N., and Howie, J. A. (2012). “Helical piles in soft sensitive soils – A field study of disturbance effects on pile capacity.” VGS Symp. Soft Gr. Eng.

Welch, R. C., and Reese, L. C. (1972). “Laterally loaded behavior of drilled shafts.” Research Report 35-65-89. Center for Highway Research. University of Texas, Austin.

Young, J. (2012). “Uplift capacity of helical anchors in cohesive soil.” MSc Thesis, Oregon State University.

Zhang, D. J. Y. (1999). “Predicting capacity of helical screw piles in Alberta soils.” MSc Thesis, University of Alberta.

Zhang, Y. J., Wei, D. S., and Liang, L. (2009). “The loading translation of screw pile on pullout test under inclined loading.” Journal of Transport Science and Engineering, 25(4).

Zhao, Y. P., Bi, C. W., Chen, C. P., Li, Y. C., and Dong, G. H. (2015). “Experimental study on flow velocity and mooring loads for multiple net cages in steady current.” Aquacultural Engineering, Elsevier B.V., 67, 24–31.

APPENDIX A-AQUACULTURE LOADING ESTIMATION

Given Conditions

		[units]	
Sn	0.3	[-]	Solidity
C_{DN}	0.56	[-]	Normal Drag coefficient
C_{DP}	0.04	[-]	Parallel Drag coefficient
r	0.74	[-]	Reduction factor
ρ	1000	[kg/m3]	Water density
B	20	[m]	Cage width
l	20	[m]	Cage length
D	8	[m]	Cage depth
n	7	[-]	Cages Parallel to flow
m	1	[-]	Cages normal to flow
ML	0.2	[-]	Max Load percentage

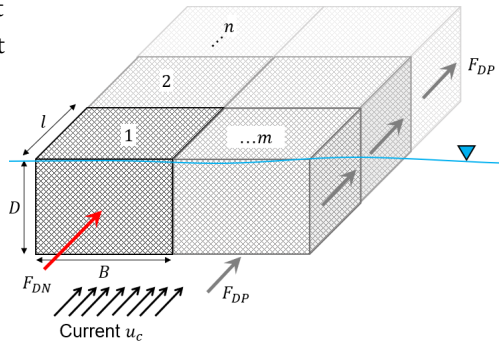

$$F_{DN} = \frac{1}{2}\rho C_{DN} u_c^2 (BD) m \left(\frac{1-r^{4n}}{1-r^2}\right)$$

$$F_{DP} = \frac{1}{2}\rho C_{DP} u_c^2 (B+2D) lm \left(\frac{1-r^{4n}}{1-r^2}\right) r^2$$

Current velocity (m/s)					$\beta = 0$	$\beta = 15$	$\beta = 45$	$\beta = 60$	$\beta = 75$
					0	15	45	60	75
u_i (m/s)	**F_{DN} (kN)**	**F_{DP} (kN)**	**P/N (%)**	**F_{Dtot} (kN)**	**Mooring load (kN)**				
0.30	9	2	18	11	2	2	3	4	8
0.40	16	3	18	19	4	4	5	8	15
0.50	25	4	18	29	6	6	8	12	23
0.60	36	6	18	42	8	9	12	17	33
0.70	49	9	18	58	12	12	16	23	44
0.80	64	11	18	75	15	16	21	30	58
0.90	81	14	18	95	19	20	27	38	74
1.00	100	18	18	118	24	24	33	47	91
1.10	121	21	18	142	28	29	40	57	110
1.20	144	26	18	169	34	35	48	68	131
1.30	169	30	18	199	40	41	56	79	153
1.40	195	35	18	230	46	48	65	92	178
1.75	305	54	18	360	72	75	102	144	278

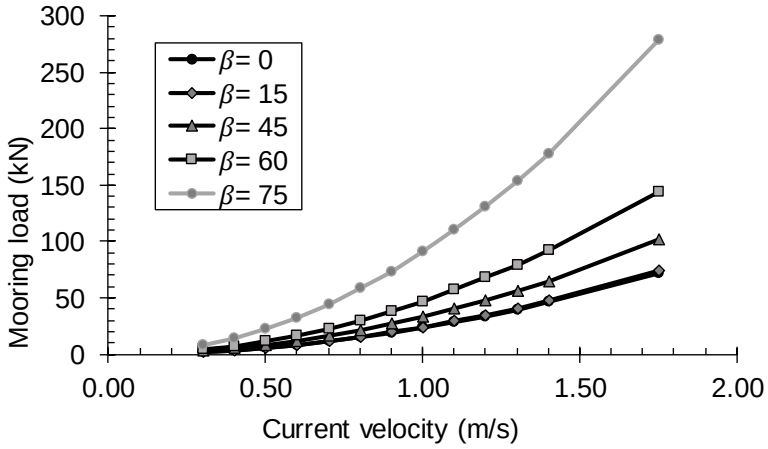

APPENDIX B-3D FINITE ELEMENT (FE) RESULTS

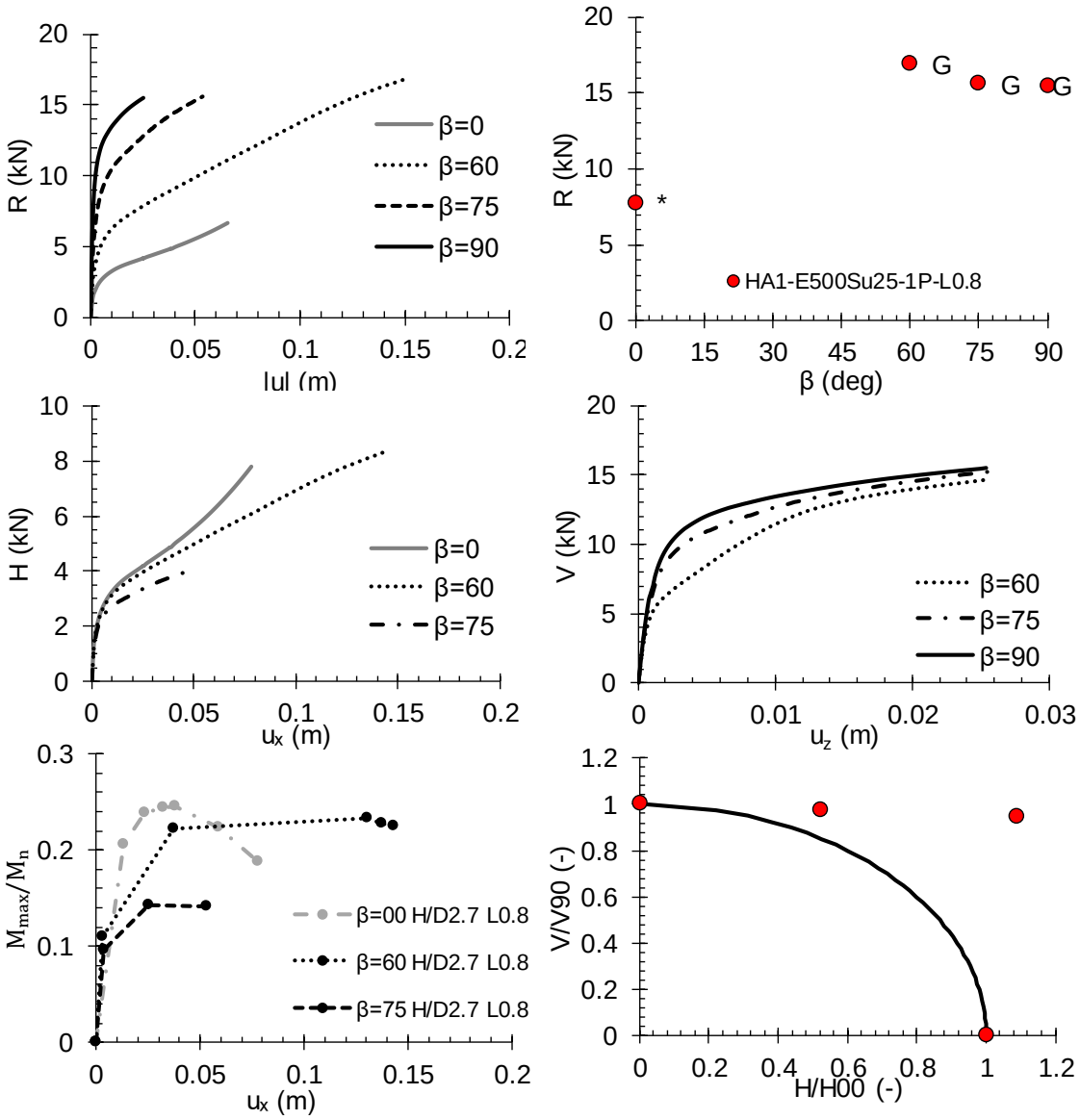

Figure B.1. FE results of one-plate helical anchor HA1-H/D 2.7 L0.8 E500Su25 L0.8. *Structural failure never reached.

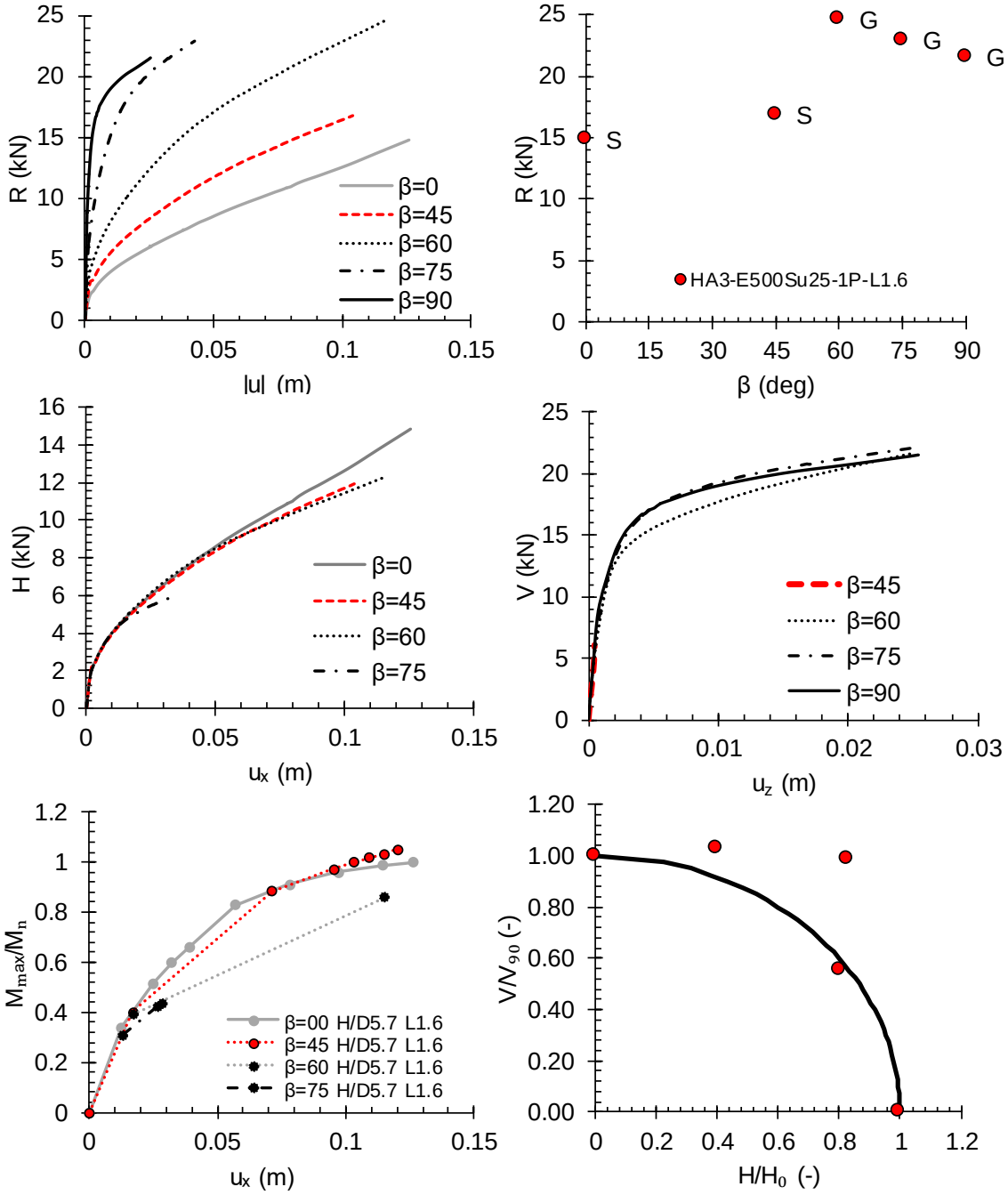

Figure B.2. FE results of one-plate helical anchor HA3-H/D 5.7 E500Su25 L1.6

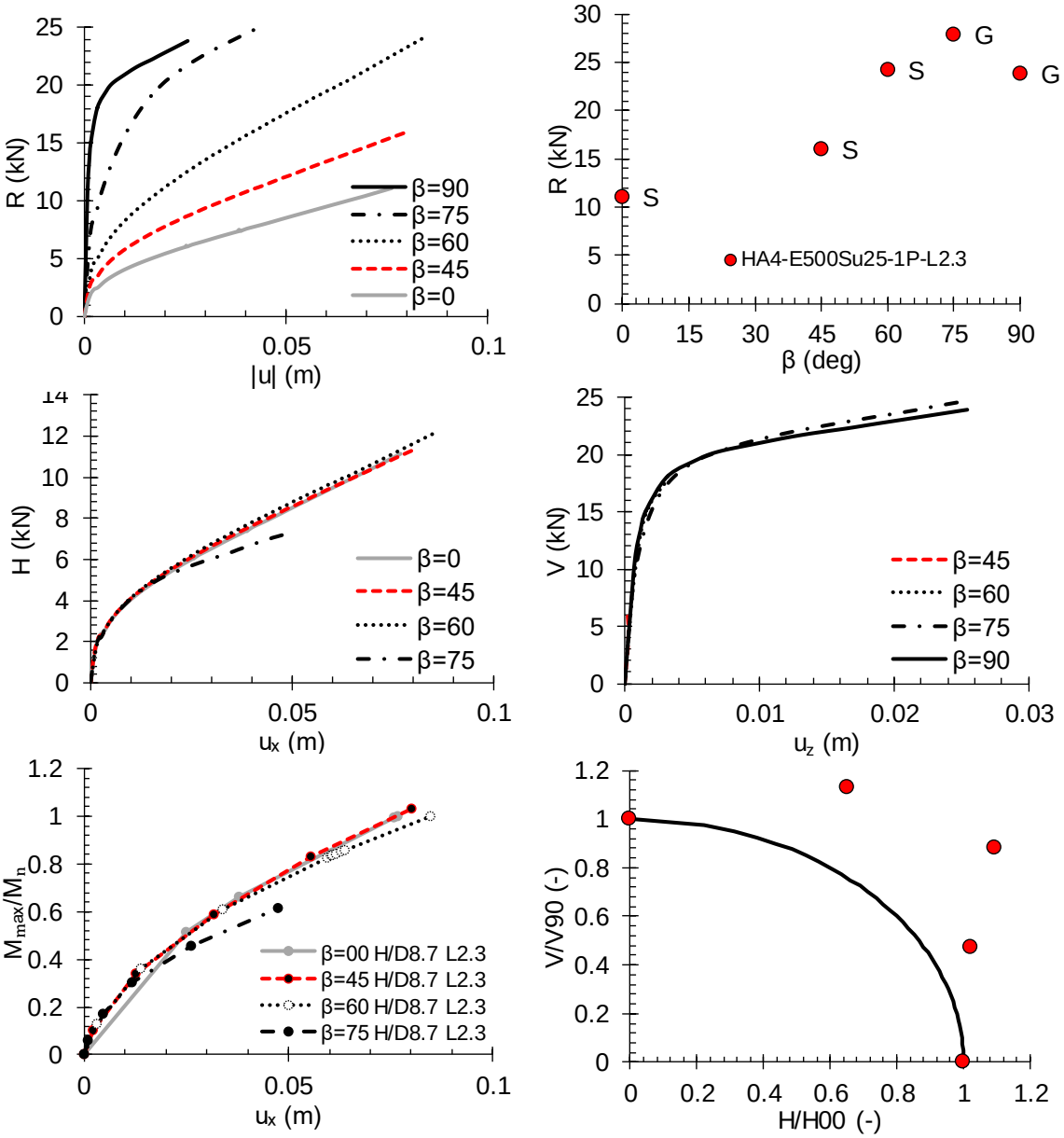

Figure B.3. FE results of one-plate helical anchor HA4-E500Su25-1P-L2.3

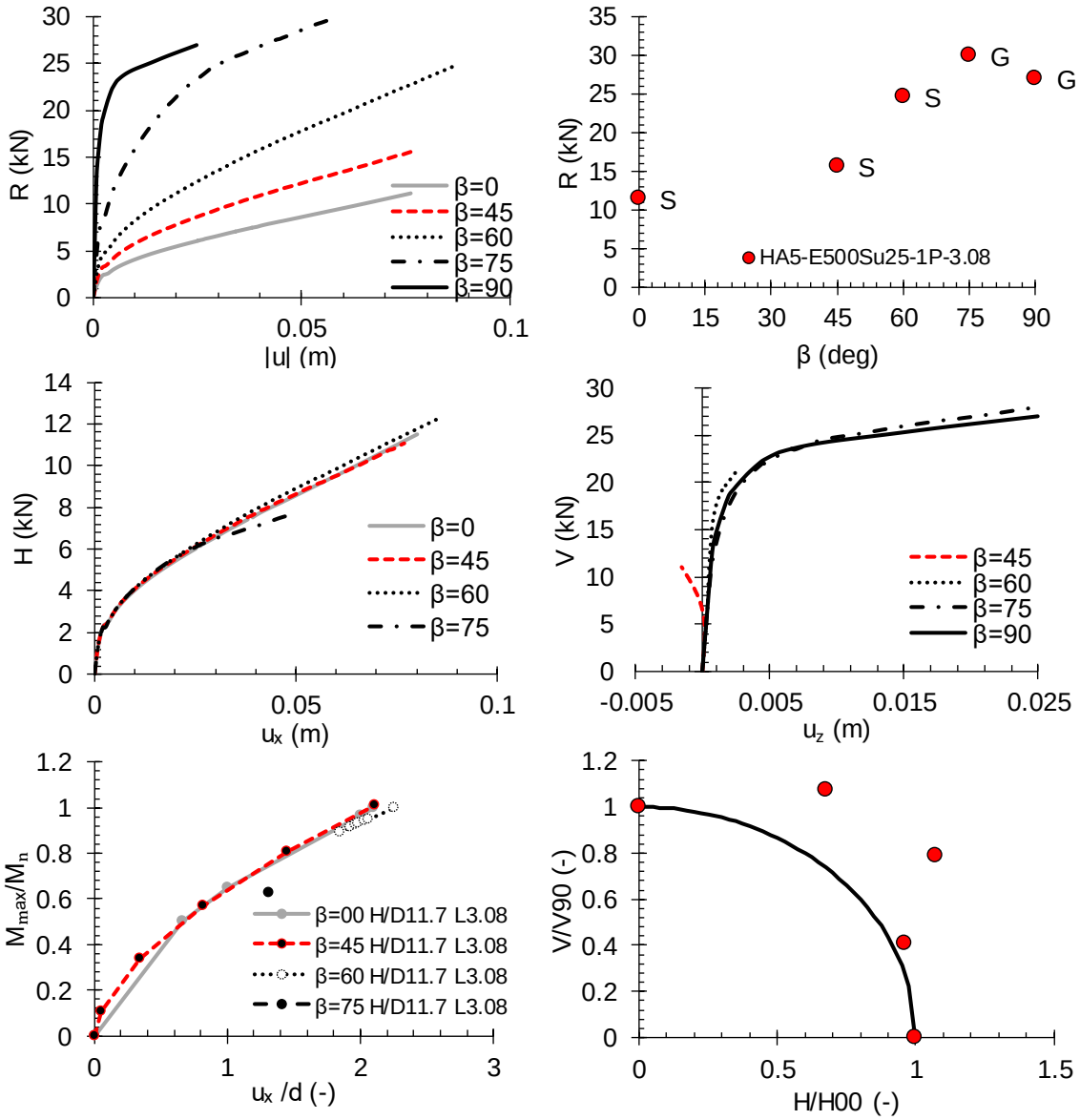

Figure B.4. FE results of one-plate helical anchor HA5 1P H/D 8.7 L3.08 E500Su25

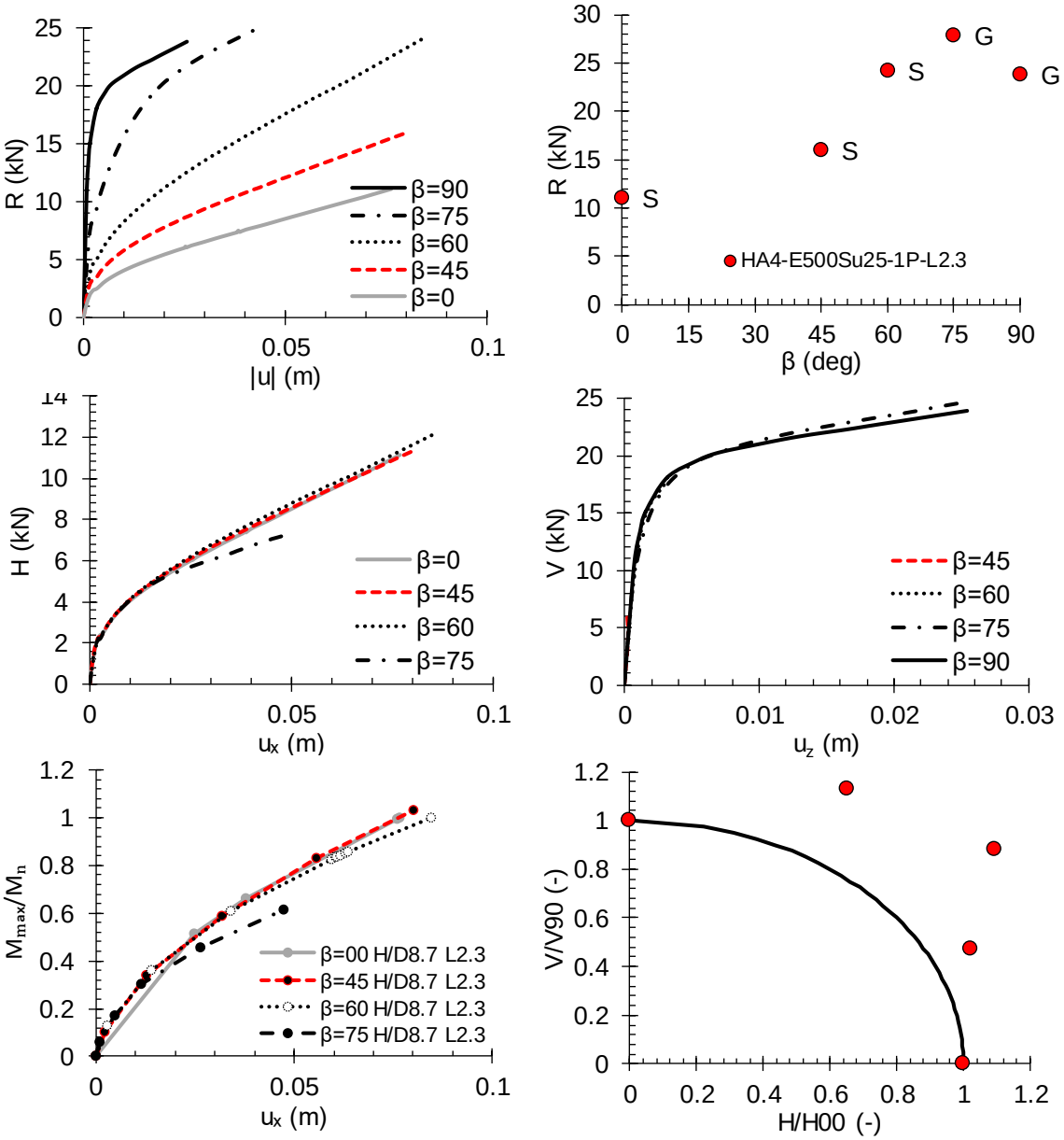

Figure B.5. FE results of two-plates helical anchor HA6-E500Su25-2P-H1.7-L1.6

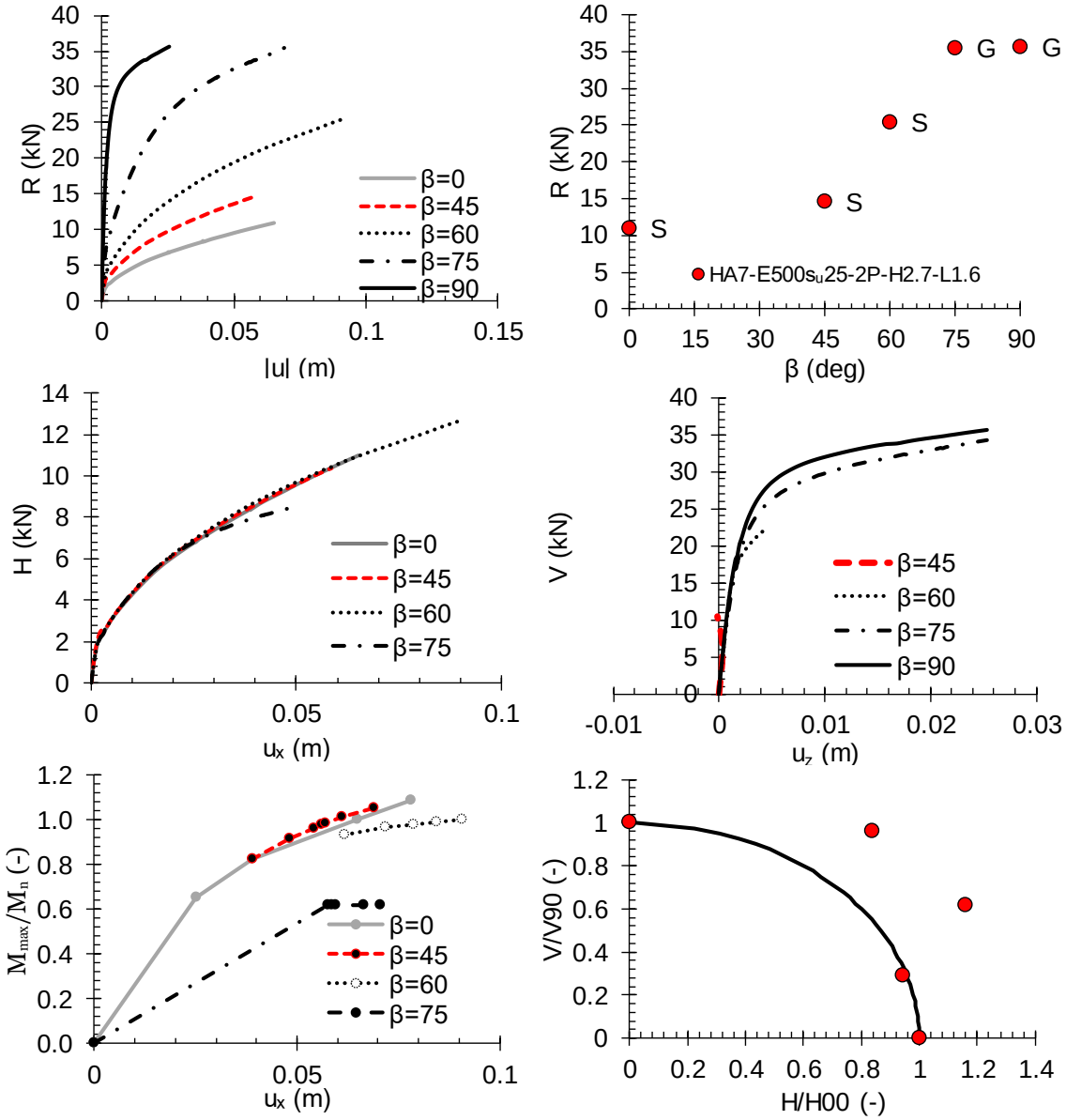

Figure B.6. FE results of two-plates helical anchor HA7 2P H/D2.7 L1.6 E500Su25

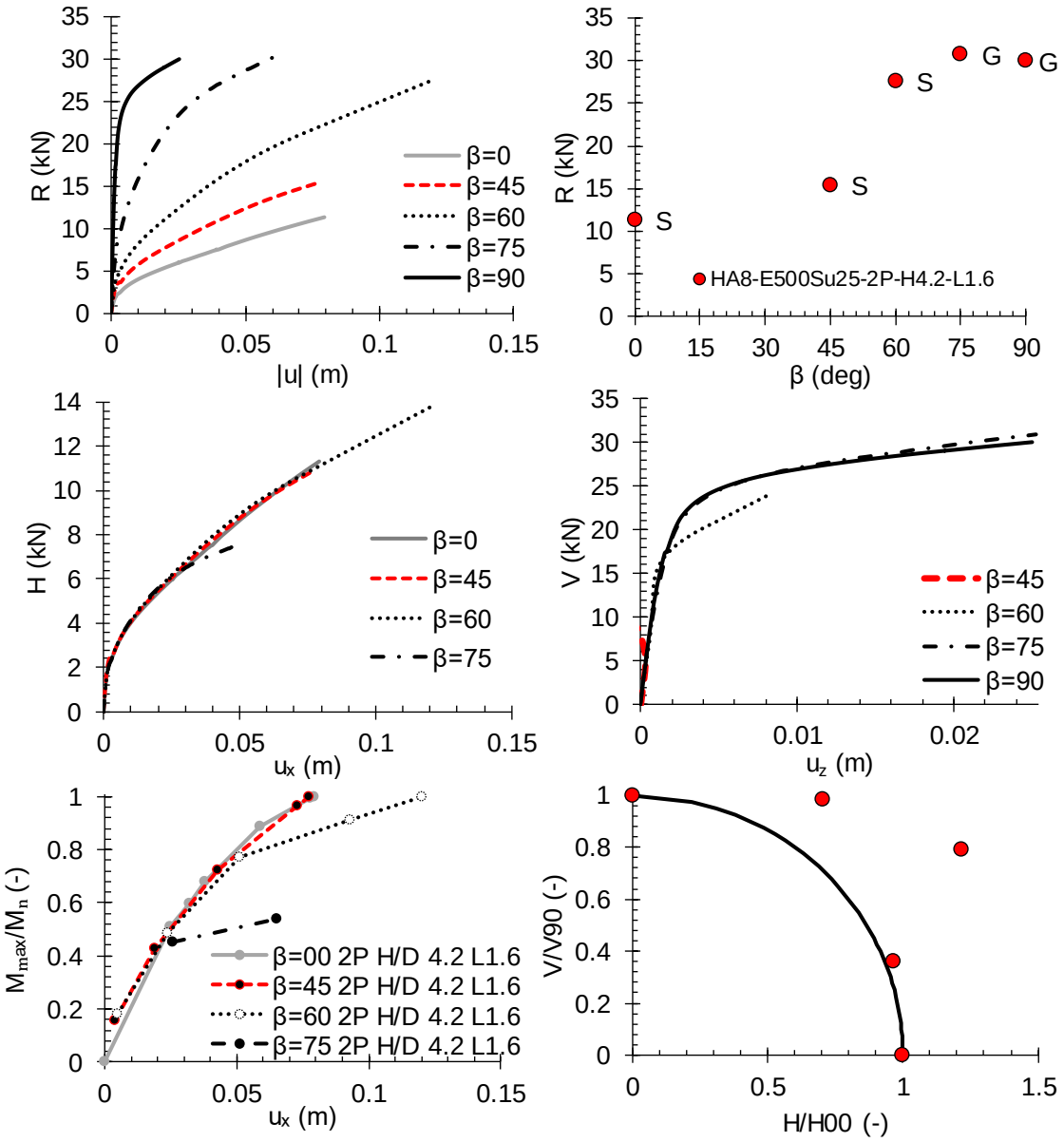

Figure B.7. FE results of two-plates helical anchor HA8 2P H/D4.2 L1.6 E500Su25

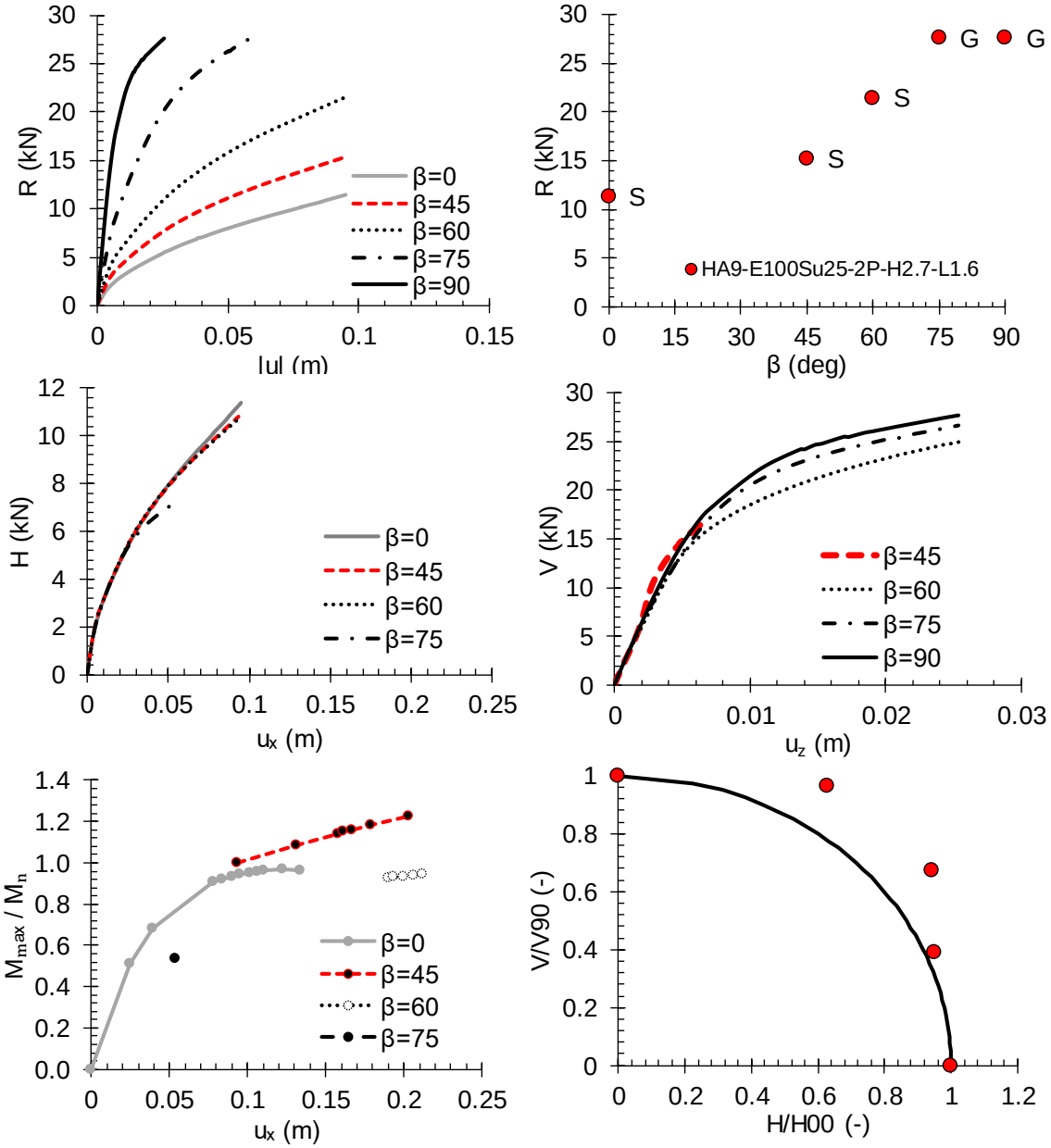

Figure B.8. FE results of two-plates helical anchor HA9 E100Su25

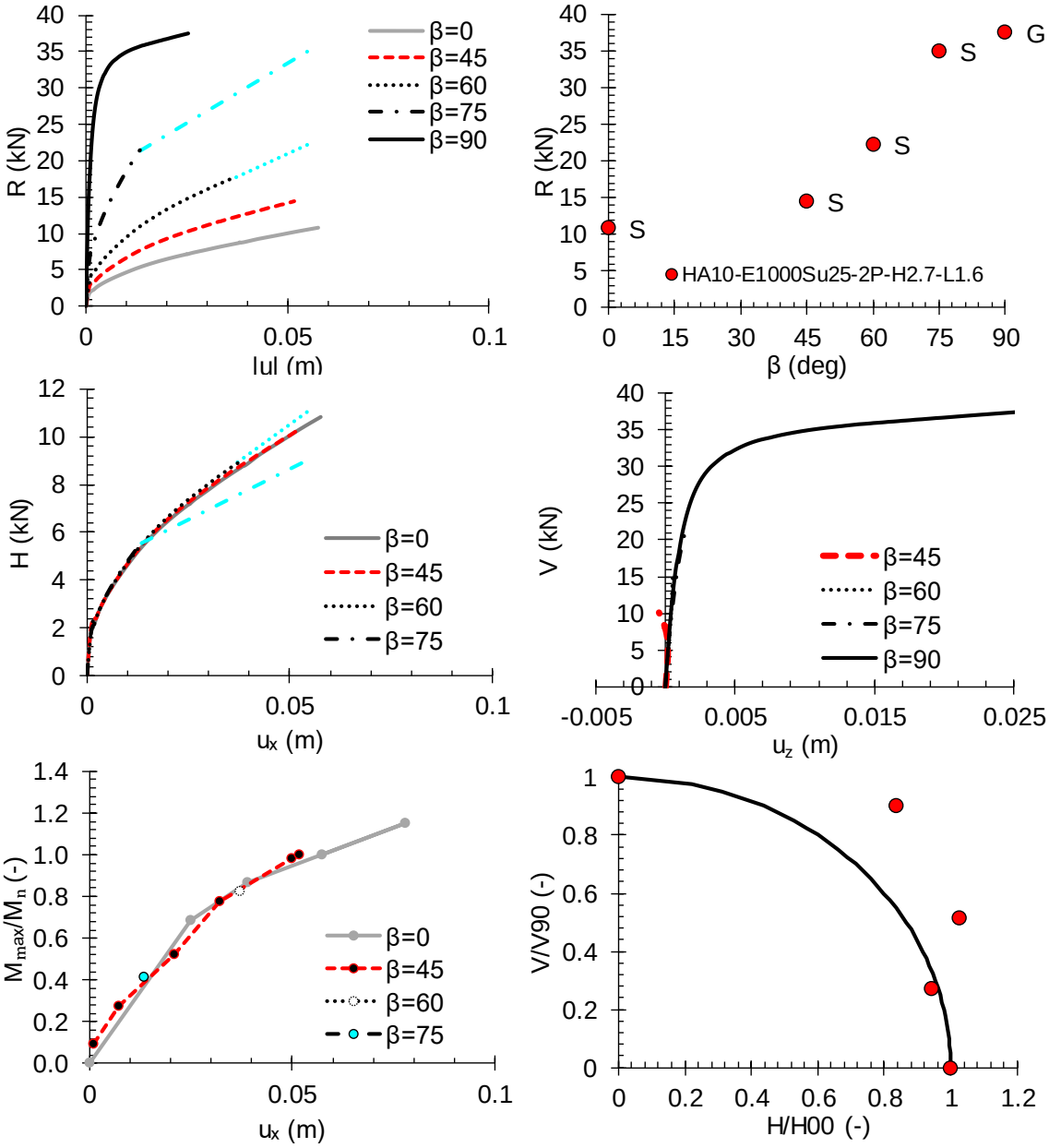

Figure B.9. FE results of two-plates helical anchor HA10-E1000Su25-2P-H2.7-L1.6

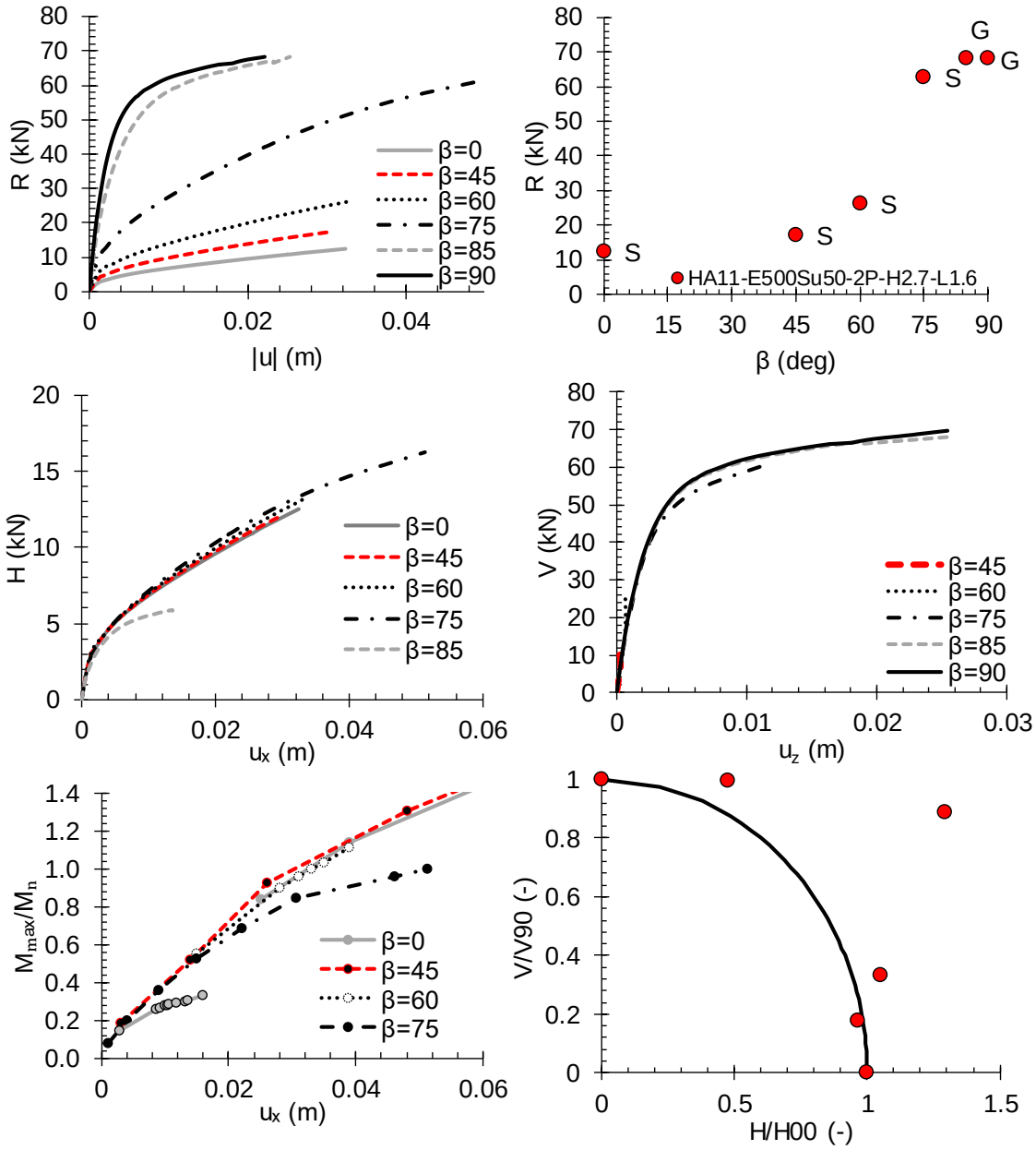

Figure B.10. FE results of two-plates helical anchor HA11-2P H/D2.7 L1.6 E500Su50

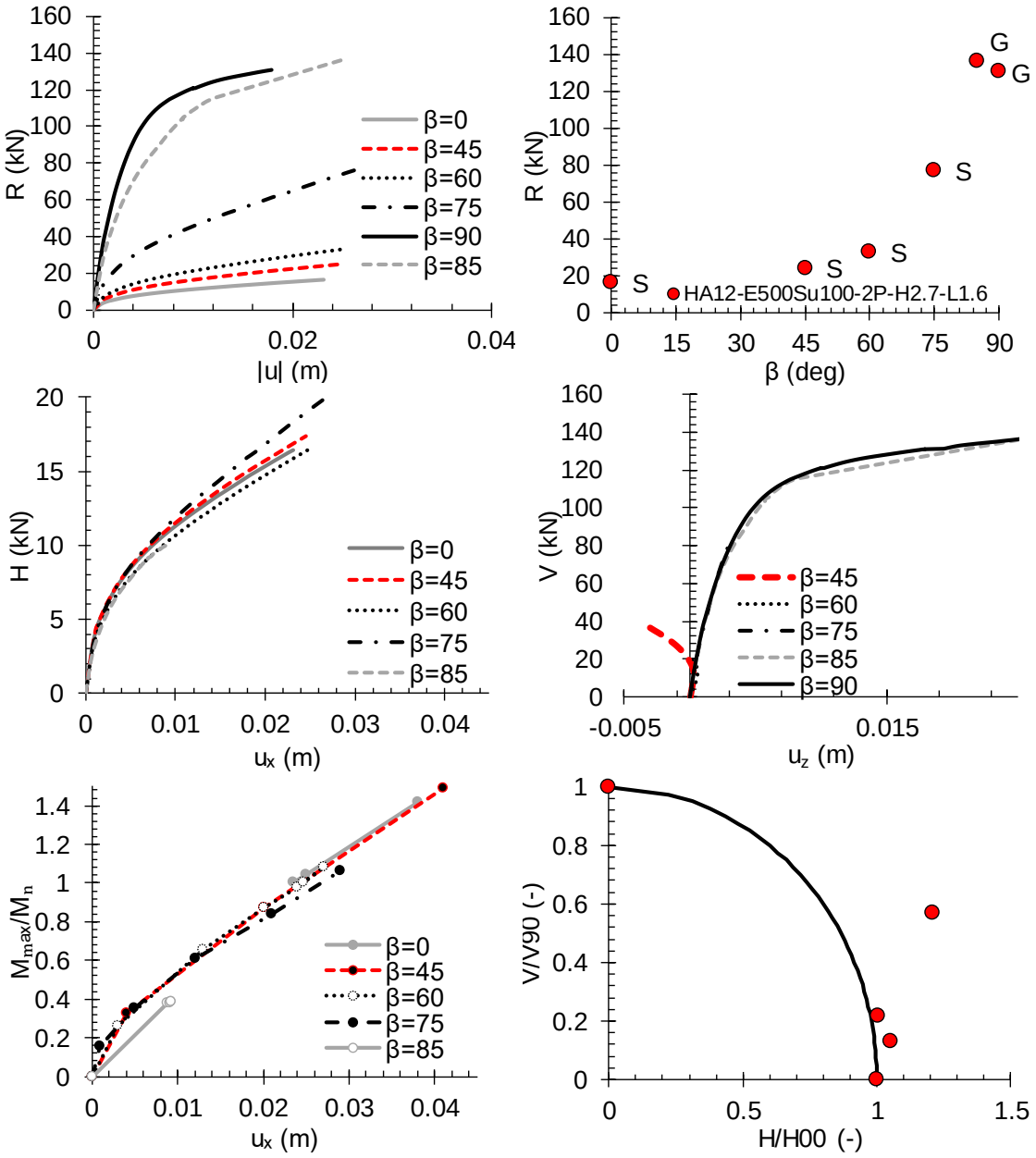

Figure B.11. FE results of two-plates helical anchor HA12-2P H/D2.7 L1.6 E500Su100

APPENDIX C-RELIABILITY USING HASOFER-LIND METHOD-MATLAB

Main Pbeta

```
clear all
global d L H D beta_ang EpIp  n Mn r_dz gamma_ef Su J epsilon
COV_Ph COV_Su Miu_Ph Miu_Su...
    stepi Beta_vec g_vec Xopt_vec Ypy_res Equil_res Ypy_vec
Equil_vec step2
%----Anchor Definition---
d=0.038;%Pile diameter
L=3.1;%Pile embedded length
H=3.0;%Plate Depth
D=0.254;%Plate diameter
% e=0;%Eccentricity of the pile
% delta=2;%Parameter to spacial variability
EpIp=35.12;%Pile Stiffness
Mn=3.35;%(kN-m) Shaft nominal moment
%Soil Properties
gamma_ef=20-9.8;%(kN/m3)
Su=25;%(kPa)
J=0.5;%(-)
epsilon=0.02;%

%Depth discretization
n=31;%number of segments, nodes=n+1
r_dz=L/n;%ratio of geometric ratio

%Working conditions
Miu_Ph=3;
Miu_Su=25;%(kPa)
beta_ang=9*pi/180;
COV_Ph=0.2;
COV_Su=0.2;
% COV_beta_ang=0.1;
% Rho_P_beta_ang=0.99;

miu(1)=Miu_Ph;
miu(2)=Miu_Su;miu=miu';

%Change in FS and Beta_RBD with changes in beta_ang thus Ph
step_ang=1;
beta_ang_vec=4:step_ang:23;beta_ang_vec=beta_ang_vec';%beta_ang
vector
beta_rad=beta_ang_vec*pi/180;
a=0.247;b=0.805;%P=a*(beta_ang)+b from Nguyen et al. (2018) paper
Fig 15
P_vec=a.*beta_ang_vec(:)+b;

Beta_vec=zeros(size(P_vec,1),1);g_vec=zeros(size(P_vec,1),1);
```

```
Xopt_vec=zeros(size(P_vec,1),2);iter_Beta=zeros(size(P_vec,1),1);
flag_Beta=zeros(size(P_vec,1),1);H0_vec=zeros(size(P_vec,1),1);
stepi=1;
tic%Start timer
%Changing Attack angle
for stepi=1:size(P_vec,1)
    beta_ang=beta_rad(stepi);
    miu(1)=P_vec(stepi);
    %Compute Reliability
    [Beta,c,Xopt,iter,flag]=Beta_RBD_miu(miu);
    Beta_vec(stepi)=Beta;
    g_vec(stepi)=c;
    Xopt_vec(stepi,:)=Xopt';
    iter_Beta(stepi)=iter;
    flag_Beta(stepi)=flag;
    toc%Finish timer
end

%Compute unsafe region
H0=Horizontal(miu);%H0 does not depends on the angle or load,
just P
V90= Vert_bearing(H,D,d,gamma_ef,miu(2));%V90 does not depends on
the angle or load, just P
R_vec=min(H0*ones(size(P_vec,1),1)./cos(beta_rad),V90*ones(size(P
_vec,1),1)./sin(beta_rad));
FS=R_vec./P_vec;%Factor of Safety
figure(3);plot(beta_ang_vec,FS);xlabel('\beta_{angle} (deg)');
ylabel ('Factor of Safety,FS');ylim([0 4])

figure(1)
subplot(2,2,1);
plot(beta_ang_vec,Beta_vec,'-or');hold on
xlabel('\beta_{angle} (deg)'); ylabel
('\beta_R');legend('Beta_{RBD-Su}')
% figure
subplot(2,2,2);
plot(beta_ang_vec,g_vec,'-or');hold on
xlabel('\beta_{angle} (deg)'); ylabel ('g(x)');legend('Beta_{RBD-
Su}')
% figure
subplot(2,2,3);
plot(beta_ang_vec,Xopt_vec(:,1),'-or');hold on
xlabel('\beta_{angle} (deg)'); ylabel
('Pcritical');legend('Beta_{RBD-Su}')
% figure
subplot(2,2,4);
plot(beta_ang_vec,Xopt_vec(:,2),'-or');hold on
xlabel('\beta_{angle} (deg)'); ylabel
('Su_critical');legend('Beta_{RBD-Su}')

figure(2)%Unsafe region
plot(R_vec,beta_ang_vec,'-k','LineWidth',2);hold on
```

```
xlabel('R_{vec}'); ylabel ('\beta_{angle} (deg)');legend('Unsafe
Region')
plot(Xopt_vec(:,1),beta_ang_vec,'-or');hold on
plot(P_vec,beta_ang_vec,'-ob')
ylabel('Demand'); xlabel ('\beta_{angle} (deg)');legend('Unsafe
Region','X_{critic}');hold on

XYZ_Plot
```

Main_Su

```
%clear all
global d L H D beta_ang EpIp  n Mn r_dz gamma_ef Su J epsilon
COV_Ph COV_Su Miu_Ph Miu_Su...
    stepi Beta_vec g_vec Xopt_vec Ypy_res Equil_res Ypy_vec
Equil_vec step2
%----Anchor Definition---
d=0.038;%Pile diameter
L=3.1;%Pile embedded length
H=3.0;%Plate Depth
D=0.254;%Plate diameter
% e=0;%Eccentricity of the pile
% delta=2;%Parameter to spacial variability
EpIp=35.12;%Pile Stiffness
Mn=3.35;%(kN-m) Shaft nominal moment
%Soil Properties
gamma_ef=20-9.8;%(kN/m3)
Su=25;%(kPa)
J=0.5;%(-)
epsilon=0.02;%

%Depth discretization
n=31;%number of segments, nodes=n+1
r_dz=L/n;%ratio of geometric ratio

%Working conditions
Miu_Ph=3;
Miu_Su=25;%(kPa)
beta_ang=9*pi/180;
COV_Ph=0.2;
COV_Su=0.2;
% COV_beta_ang=0.1;
% Rho_P_beta_ang=0.99;

miu(1)=Miu_Ph;
miu(2)=Miu_Su;miu=miu';

Su_step=1;
m_Su=9:Su_step:45;m_Su=m_Su';
Beta_vec=zeros(size(m_Su,1),1);g_vec=zeros(size(m_Su,1),1);
```

```
Xopt_vec=zeros(size(m_Su,1),2);iter_Beta=zeros(size(m_Su,1),1);fl
ag_Beta=zeros(size(m_Su,1),1);H0_vec=zeros(size(m_Su,1),1);
stepi=1;
tic%Start timer
%Changing Sui
for stepi=1:size(m_Su,1)
    miu(2)=m_Su(stepi);
    %Compute Reliability
    [Beta,c,Xopt,iter,flag]=Beta_RBD_miu(miu);
    Beta_vec(stepi)=Beta;
    g_vec(stepi)=c;
    Xopt_vec(stepi,:)=Xopt';
    iter_Beta(stepi)=iter;
    flag_Beta(stepi)=flag;
    toc%Finish timer
end

%Compute unsafe region
step2=1;
for step2=1:size(m_Su,1)
    miu(2)=m_Su(step2);
    %Compute Factor of Safety
    H0_vec(step2)=Horizontal(miu);
    V90(step2)= Vert_bearing(H,D,d,gamma_ef,miu(2));
%     H0_vec(step2)=Horizontal2(miu);%To improve py solver
%     Ypy_vec(step2,:)=Ypy_res';%To improve py solver
%     Equil_vec(step2)=Equil_res;%To improve py solver
end

R_vec=min(H0_vec./cos(beta_ang),V90'./sin(beta_ang));%When P=R,
unsafe region
FS=R_vec./(Miu_Ph*ones(size(R_vec,1),1));%Factor of Safety
figure(3);plot(m_Su,FS);xlabel('\mu_{Su}'); ylabel ('Factor of
Safety,FS');ylim([0 4])

figure(1)
subplot(2,2,1);
plot(m_Su,Beta_vec,'-or');hold on
xlabel('\mu_{Su}'); ylabel ('\beta_R');legend('Beta_{RBD-Su}')
% figure
subplot(2,2,2);
plot(m_Su,g_vec,'-or');hold on
xlabel('\mu_{Su}'); ylabel ('g(x)');legend('Beta_{RBD-Su}')
% figure
subplot(2,2,3);
plot(m_Su,Xopt_vec(:,1),'-or');hold on
xlabel('\mu_{Su}'); ylabel ('Pcritical');legend('Beta_{RBD-Su}')
% figure
subplot(2,2,4);
plot(m_Su,Xopt_vec(:,2),'-or');hold on
xlabel('\mu_{Su}'); ylabel ('Su_critical');legend('Beta_{RBD-
Su}')
```

```
figure(2)
plot(m_Su,R_vec,'-k','LineWidth',2);ylim([0 10]);hold on
xlabel('\mu_{Su}'); ylabel ('P, Demand (kN)');legend('Unsafe
Region')
plot(Xopt_vec(:,2),Xopt_vec(:,1),'-or');hold on
ylabel('P (kN)'); xlabel ('Su (kPa)');legend('Unsafe
Region','X_{critic}');hold on

%Plot ellipses
%%Initial Ellipse
Su=25;
a=Su*COV_Su; b=Miu_Ph*COV_Ph; % a,horizontal radius;b,vertical
radius
x0=Su;y0=Miu_Ph; % x0,y0 ellipse centre coordinates
t=-pi:0.01:pi;x=x0+a*cos(t);y=y0+b*sin(t);figure (2);plot(x,y,'-
k','LineWidth',1.5);hold on;plot(Su,Miu_Ph,'*')%Inital Ellipse
aa=Su*COV_Su*Beta_vec(find(m_Su==Su)); % horizontal radius
bb=Miu_Ph*COV_Ph*Beta_vec(find(m_Su==Su)); % vertical radius
t=-pi:0.01:pi;x=x0+aa*cos(t);y=y0+bb*sin(t);figure
(2);plot(x,y,'--
k','LineWidth',1.5);plot(Xopt_vec(find(m_Su==Su),2),Xopt_vec(find
(m_Su==Su),1),'or')%Optimized ellipse
Su=15;
a=Su*COV_Su; % horizontal radius
b=Miu_Ph*COV_Ph; % vertical radius
x0=Su; % x0,y0 ellipse centre coordinates
y0=Miu_Ph;
t=-pi:0.01:pi;x=x0+a*cos(t);y=y0+b*sin(t);figure (2);plot(x,y,'-
b','LineWidth',1.5);hold on;plot(Su,Miu_Ph,'*')%Inital Ellipse
a=Su*COV_Su*Beta_vec(find(m_Su==Su)); % horizontal radius
b=Miu_Ph*COV_Ph*Beta_vec(find(m_Su==Su)); % vertical radius
t=-pi:0.01:pi;x=x0+a*cos(t);y=y0+b*sin(t);figure (2);plot(x,y,'--
b','LineWidth',1.5);plot(Xopt_vec(find(m_Su==Su),2),Xopt_vec(find
(m_Su==Su),1),'ob')%Optimized ellipse
```

Main COV

```
clear all;close all
global d L H D beta_ang EpIp  n Mn r_dz gamma_ef Su J epsilon
COV_Ph COV_Su Miu_Ph Miu_Su...
    stepi Beta_vec g_vec Xopt_vec Ypy_res Equil_res Ypy_vec
Equil_vec step2
%----Anchor Definition---
d=0.038;%Pile diameter
L=3.1;%Pile embedded length
H=3.0;%Plate Depth
D=0.254;%Plate diameter
% e=0;%Eccentricity of the pile
% delta=2;%Parameter to spacial variability
EpIp=35.12;%Pile Stiffness
Mn=3.35;%(kN-m) Shaft nominal moment
```

```
%Soil Properties
gamma_ef=20-9.8;%(kN/m3)
Su=25;%(kPa)
J=0.5;%(-)
epsilon=0.02;%

%Depth discretization
n=31;%number of segments, nodes=n+1
r_dz=L/n;%ratio of geometric ratio

%Working conditions
Miu_Ph=3;
Miu_Su=25;%(kPa)
beta_ang=9*pi/180;
COV_Ph=0.2;
COV_Su=0.2;
% COV_beta_ang=0.1;
% Rho_P_beta_ang=0.99;

miu(1)=Miu_Ph;
miu(2)=Miu_Su;
miu=miu';

COV_step=0.025;
COV_i=0.05:COV_step:0.5;COV_i=COV_i';
Beta_vec=zeros(size(COV_i,1),1);g_vec=zeros(size(COV_i,1),1);
Xopt_vec=zeros(size(COV_i,1),2);iter_Beta=zeros(size(COV_i,1),1);
flag_Beta=zeros(size(COV_i,1),1);
stepi=1;
tic%Start timer
%Changing COV Su
for stepi=1:size(COV_i,1)
    COV_Su=COV_i(stepi);
    %Compute Reliability
    [Beta,c,Xopt,iter,flag]=Beta_RBD_miu(miu);
    Beta_vec(stepi)=Beta;
    g_vec(stepi)=c;
    Xopt_vec(stepi,:)=Xopt';
    iter_Beta(stepi)=iter;flag_Beta(stepi)=flag;
    toc%Finish timer
end
Beta_COV_Su=Beta_vec;Xopt_COV_Su=Xopt_vec;
figure
subplot(2,2,1);     plot(COV_i,Beta_vec,'-or');hold on
    xlabel('COV_{Su}'); ylabel ('\beta_R');legend('Beta_{RBD-
Su}')
subplot(2,2,2);     plot(COV_i,g_vec,'-or');hold on
    xlabel('COV_{Su}'); ylabel ('g(x)');legend('Beta_{RBD-Su}')
subplot(2,2,3);     plot(COV_i,Xopt_vec(:,1),'-or');hold on
    xlabel('COV_{Su}'); ylabel ('P_{opt}');legend('Beta_{RBD-
Su}')
subplot(2,2,4);     plot(COV_i,Xopt_vec(:,2),'-or');hold on
```

```
    xlabel('COV_{Su}'); ylabel ('Su_{opt}');legend('Beta_{RBD-
Su}')
%Plot optimum points


%Changing COV P
COV_Su=0.2;
for stepi=1:size(COV_i,1)
    COV_Ph=COV_i(stepi);
    %Compute Reliability
    [Beta,c,Xopt,iter,flag]=Beta_RBD_miu(miu);
    Beta_vec(stepi)=Beta;
    g_vec(stepi)=c;
    Xopt_vec(stepi,:)=Xopt';
    iter_Beta(stepi)=iter;flag_Beta(stepi)=flag;
    toc%Finish timer
end
Beta_COV_P=Beta_vec;Xopt_COV_P=Xopt_vec;
figure
subplot(2,2,1);     plot(COV_i,Beta_vec,'-or');hold on
    xlabel('COV_P'); ylabel ('\beta_R');legend('Beta_{RBD-Su}')
subplot(2,2,2);     plot(COV_i,g_vec,'-or');hold on
    xlabel('COV_P'); ylabel ('g(x)');legend('Beta_{RBD-Su}')
subplot(2,2,3);     plot(COV_i,Xopt_vec(:,1),'-or');hold on
    xlabel('COV_P'); ylabel ('P_{opt}');legend('Beta_{RBD-Su}')
subplot(2,2,4);     plot(COV_i,Xopt_vec(:,2),'-or');hold on
    xlabel('COV_P'); ylabel ('Su_{opt}');legend('Beta_{RBD-Su}')

%Compute unsafe region
Su_step=1;m_Su=9:Su_step:30;m_Su=m_Su';H0_vec=zeros(size(m_Su,1),
1);
step2=1;
for step2=1:size(m_Su,1)
    miu(2)=m_Su(step2);
    H0_vec(step2)=Horizontal(miu);
    V90(step2)= Vert_bearing(H,D,d,gamma_ef,miu(2));
end
R_vec=H0_vec./cos(beta_ang);
figure(3);       plot(m_Su,R_vec,'-k','LineWidth',1);ylim([0
10]);hold on
xlabel('\mu_{Su}'); ylabel ('P, Demand (kN)');legend('Unsafe
Region')

%Plot ellipses
COV=0.3;%Point to draw
index=find(COV_i==COV);
%Initial Values
COV_Su=0.2;COV_Ph=0.2;
%---------Initial Ellipse----------
x0=Su;y0=Miu_Ph; % x0,y0 ellipse centre coordinates
%Initial covariances
```

```
a=Miu_Su*COV_Su; b=Miu_Ph*COV_Ph; % a,horizontal
radius;b,vertical radius
t=-pi:0.01:pi;x=x0+a*cos(t);y=y0+b*sin(t);figure (3);plot(x,y,'-
c','LineWidth',1);hold on;plot(Su,Miu_Ph,'*')%Inital Ellipse
%----------Deformed in Su----------
a=Miu_Su*COV; b=Miu_Ph*COV_Ph; % a,horizontal radius;b,vertical
radius
t=-pi:0.01:pi;x=x0+a*cos(t);y=y0+b*sin(t);figure (3);plot(x,y,'--
b','LineWidth',1);hold on;
%----------Deformed in P----------
a=Miu_Su*COV_Su; b=Miu_Ph*COV; % a,horizontal radius;b,vertical
radius
t=-pi:0.01:pi;x=x0+a*cos(t);y=y0+b*sin(t);figure (3);plot(x,y,'--
r','LineWidth',1);hold on;
%----------Critical COV for Su----------
a=Miu_Su*COV*Beta_COV_Su(index);
b=Miu_Ph*COV_Ph*Beta_COV_Su(index); % a,horizontal
radius;b,vertical radius
t=-pi:0.01:pi;x=x0+a*cos(t);y=y0+b*sin(t);figure
(3);plot(x,y,':b','LineWidth',1);hold on;
plot(Xopt_COV_Su(index,2),Xopt_COV_Su(index,1),'o');
%----------Critical COV for P----------
a=Miu_Su*COV_Su*Beta_COV_P(index);
b=Miu_Ph*COV*Beta_COV_P(index); % a,horizontal radius;b,vertical
radius
t=-pi:0.01:pi;x=x0+a*cos(t);y=y0+b*sin(t);figure
(3);plot(x,y,':r','LineWidth',1);hold on;
legend('Unsafe region','Initial ellipse','Mean values','COV
Su','COV P','Opti COV Su','Opti COV P')
plot(Xopt_COV_P(index,2),Xopt_COV_P(index,1),'o');
```

Beta RBD_miu

```
function [Beta,c,X_opt,iter,flag]=Beta_RBD_miu(miu)
%Beta_RBD_miu optimizes the reliability Index Beta_R using the
%Hasofer-Lind method

global d L H D beta_ang EpIp  n Mn r_dz gamma_ef Su J epsilon ...
 COV_Su  COV_Ph delta Miu_Ph Miu_Su X stepi Beta_vec g_vec
Xopt_vec

%Statistical properties
Miu_Ph=miu(1);
Miu_Su=miu(2);%(kPa)

%---Initial Input---
% Ph=Miu_Ph;%1.Load
if stepi==1
    X0(1)=Miu_Ph;X0(2)=Miu_Su;X0=X0';
else,if abs(g_vec(stepi-1))<0.5
```

```
    X0=1.1*Xopt_vec(stepi-1,:)';%Initial value similar to
previous solution but not the same.
    else
    X0(1)=Miu_Ph;X0(2)=Miu_Su;X0=X0';
    end
end

%---Reliability optimization
fun = @OBJ;
A = [];
b = [];
Aeq = [];
beq = [];
lb = [0;0];
ub = [];
nonlcon = @const;
options =
optimoptions('fmincon','MaxFunctionEvaluations',60000,'StepTolera
nce',1e-9,'Display','off');
[X,fval,exitflag] =
fmincon(fun,X0,A,b,Aeq,beq,lb,ub,nonlcon,options);
% Beta=fval
% X
% c = const(X);

tol=0.0001;maxiter=100;iter=1;maxdiff=1;
while abs(maxdiff)>tol && iter<=maxiter
    if iter==1
        Xprev=0.0001;
    end
    if iter>1
        Xprev=X;
    end
    options = optimset('MaxFunEvals',60000,'Display','off');
    [X,fval,exitflag] =
fmincon(fun,X,A,b,Aeq,beq,lb,ub,nonlcon,options);
%     [y] = py_RBD_y_Q(X);
    maxdiff=max(abs(Xprev-X));
    iter=iter+1;
end
flag=exitflag;
X_opt=X;
Beta=fval;
c = const(X);
end


function [c,ceq] = const(X)
global beta_ang H D d gamma_ef
tol2=0.0001;
% c(1) = py_RBD3(X)-tol2;%Equlibrium to find H0 using p-y
```

```
V90=Vert_bearing(H,D,d,gamma_ef,X(2));%Vertical capacity
H0=Horizontal(X);%Horizontal capacity from p-y
R=min(H0/cos(beta_ang),V90/sin(beta_ang));
P_demand=X(1);
g_perf=abs(P_demand-R);
c(1)=g_perf-tol2;
ceq = [];
[X(2) c(1);X(1) R];
% hola=1+1;


function [H00]=Horizontal(X)
global XX
XX=X;%X(1)=Ph;X(2)=Su
y0=[0 0];
tol=0.0001;maxiter=100;iter=1;maxdiff=1;
Ypy=[y0]';
while abs(maxdiff)>tol && iter<=maxiter
    if iter==1
        yprev=0.0001;
    end
    if iter>1
        yprev=y;
    end
    options = optimset('MaxFunEvals',30000);
    Ypy = fminsearch(@py_RBD3,Ypy,options);%EQULIBRIUM IN PY
%     options =
optimoptions('fmincon','MaxFunctionEvaluations',30000,'Display','
off');
%     [Xpy] = fmincon(@py_RBD3,Xpy,[],[],[],[],[-0.1;-
0.1],[0.1;0.1],[],[]);
    [Equil] = py_RBD3(Ypy);
    [y] = py_RBD_y_Q(Ypy);
    maxdiff=max(abs(yprev-y));
    iter=iter+1;
end
[y,Q] = py_RBD_y_Q(Ypy);
H00=Q(1);



function [V90] = Vert_bearing(H,D,d,gamma_ef,Su)
%Vert computes vertical capacity of helical anchors

a=pi/4*D^2;
Nc=13.7*(1-exp(-0.35*H/D));%Merifield 2002
if Nc>12.6
    Nc=12.6;
end
alpha=1.0;%Adhesion factor on the shaft
V90=(Su*Nc+gamma_ef*H)*a+(pi*d*H)*Su*alpha;
end
```

```
function [ksecd] = Matlock_SoftC(gamma_ef, J, d, epsilon, cu, z,
y)
%Matlock_OC Computes p-y distribution for OC clays
% pu = (3 + gamma_ef*z/cu + J * z / d) * cu * d;

RSpile_factor=0.88;%RSpile factor of 22/25 in critical
displacement y50 and reaction force

%Ultimate resistance force
pu =(3 + gamma_ef*z/cu + J * z / d ) * d*cu;

if pu > (9 * cu * d)
    pu = 9 * cu * d;
end

y50 =2.5*epsilon * d*RSpile_factor;

y = abs(y);
if (y/y50) <8
    p=0.5*pu*(y/y50)^(1/3);
end
if (y/y50) >= 8
    p = pu;
end
if y==0
    ksecd=0;
else
ksecd = p / y;
end
ksecd=RSpile_factor*ksecd;%
end
```

XYZ PLOT

```
m_Su=5:1:30;m_Su=m_Su';
%Compute unsafe region
H0_vec=zeros(size(m_Su,1),1);
step2=1;
for step2=1:size(m_Su,1)
    miu(2)=m_Su(step2);
    H0_vec(step2)=Horizontal(miu);
end
H0_vec(22)=nan;H0_vec(26)=nan;
RR=ones(size(beta_rad,1),size(H0_vec,1));
for i=1:size(beta_rad,1)
    RR(i,:)=H0_vec./cos(beta_rad(i));
end

for i=1:size(beta_rad,1)
```

```
    figure (5)

plot3(m_Su,RR(i,:)',beta_ang_vec(i)*ones(size(m_Su,1),1));hold
on;xlim([5,45]);ylim([2,8])
end

figure (5);hold on;
plot3(Xopt_vec(:,2),Xopt_vec(:,1),beta_ang_vec,'-
o','LineWidth',1)

%%Ellipse
for i=1:size(beta_ang_vec,1)
beta_ang2=beta_ang_vec(i);
Su=25;
P_vec2=P_vec(find(beta_ang_vec==beta_ang2),1);

a=Su*COV_Su; b=P_vec2*COV_Ph; % a,horizontal radius;b,vertical
radius
x0=Su;y0=P_vec2; % x0,y0 ellipse centre coordinates
t=-pi:0.01:pi;x=x0+a*cos(t);y=y0+b*sin(t);
figure (5);
plot3(x,y,beta_ang2(ones(1,size(x,2))),'-k','LineWidth',1);hold
on;plot3(Su,P_vec2,beta_ang2,'*')%Inital Ellipse

aa=Su*COV_Su*Beta_vec(find(beta_ang_vec==beta_ang2)); %
horizontal radius
bb=P_vec2*COV_Ph*Beta_vec(find(beta_ang_vec==beta_ang2)); %
vertical radius
t=-pi:0.01:pi;x=x0+aa*cos(t);y=y0+bb*sin(t);
figure (5);
plot3(x,y,beta_ang2(ones(1,size(x,2))),'--
k','LineWidth',1);plot3(Xopt_vec(find(beta_ang_vec==beta_ang2),2)
,Xopt_vec(find(beta_ang_vec==beta_ang2),1),beta_ang2,'or')%Optimi
zed ellipse

% beta_ang2=9;
% Su=25;
% P_vec2=P_vec(find(beta_ang_vec==beta_ang2),1);
%
% a=Su*COV_Su; b=P_vec2*COV_Ph; % a,horizontal radius;b,vertical
radius
% x0=Su;y0=P_vec2; % x0,y0 ellipse centre coordinates
% t=-pi:0.01:pi;x=x0+a*cos(t);y=y0+b*sin(t);
% figure (5);
% plot3(x,y,beta_ang2(ones(1,size(x,2))),'-
k','LineWidth',1.5);hold on;plot3(Su,P_vec2,beta_ang2,'*')%Inital
Ellipse
%
% aa=Su*COV_Su*Beta_vec(find(beta_ang_vec==beta_ang2)); %
horizontal radius
% bb=P_vec2*COV_Ph*Beta_vec(find(beta_ang_vec==beta_ang2)); %
vertical radius
```

```
% t=-pi:0.01:pi;x=x0+aa*cos(t);y=y0+bb*sin(t);
% figure (5);
% plot3(x,y,beta_ang2(ones(1,size(x,2))),'--
k','LineWidth',1.5);plot3(Xopt_vec(find(beta_ang_vec==beta_ang2),
2),Xopt_vec(find(beta_ang_vec==beta_ang2),1),beta_ang2,'or')%Opti
mized ellipse
end
xlabel('Su (kPa)'),ylabel('P (kN)'),zlabel('\beta (degrees)')


function [Beta] = OBJ(X)
global Miu_Su COV_Su Miu_Ph COV_Ph  %dz1 delta n r_dz
%Taking Data  Out
%Reliability
m=zeros(size(X,1),1);
sigma=zeros(size(X,1),1);
m(1)=Miu_Ph;
m(2)=Miu_Su;
sigma(1)=Miu_Ph*COV_Ph;
sigma(2)=Miu_Su*COV_Su;

%Correlation matrix
R=eye(size(X,1));
%Spatial correlation matrix
% for i=2:size(x,1)
%     for j=2:size(x,1)
%         R(i,j)=exp(-abs((z(i-1)-z(j-1)))/delta);
%     end
% end

Beta_prev=inv(R)*((X-m)./sigma);
Beta=((X-m)./sigma)'*Beta_prev;
Beta=Beta^0.5;
end
```

%Unsafe Region

```
global d L H D beta_ang EpIp  n Mn r_dz gamma_ef Su J epsilon
COV_Ph COV_Su Miu_Ph Miu_Su
%----Anchor Definition---
d=0.038;%Pile diameter
L=3.1;%Pile embedded length
H=3.0;%Plate Depth
D=0.254;%Plate diameter
% e=0;%Eccentricity of the pile
% delta=2;%Parameter to spacial variability
EpIp=35.12;%Pile Stiffness
Mn=3.35;%(kN-m) Shaft nominal moment
%Soil Properties
gamma_ef=20-9.8;%(kN/m3)
Su=25;%(kPa)
```

```
J=0.5;%(-)
epsilon=0.02;%

%Depth discretization
n=31;%number of segments, nodes=n+1
r_dz=L/n;%ratio of geometric ratio

%Working conditions
Miu_Ph=3;
Miu_Su=25;%(kPa)
beta_ang=9*pi/180;
COV_Ph=0.2;
COV_Su=0.3;
% COV_beta_ang=0.1;
% Rho_P_beta_ang=0.99;



miu(1)=Miu_Ph;
miu(2)=Miu_Su;
miu=miu';
Su_step=1;
m_Su2=[5:1:20 20:0.1:40];m_Su2=m_Su2';
H0_i=zeros(size(m_Su2,1),1);
R_ii=zeros(size(m_Su2,1),1);

%
X_opt_i=zeros(size(m_Su,1),2);iter_i=zeros(size(m_Su,1),2);flag_i
=zeros(size(m_Su,1),2);

%Changing Sui
for i=1:size(m_Su2,1)
    miu(2)=m_Su2(i);
    H0_i(i)=Horizontal(miu);%Horizontal capacity from p-y
end
R_ii=H0_i./cos(beta_ang);
figure(2)
plot(m_Su2,R_ii,'-r','LineWidth',4);ylim([0 10])
xlabel('\mu_{Su}'); ylabel ('P, Demand (kN)');legend('Beta_{RBD-
Su}')
hold on

Miu_Su=26;
plot(Miu_Su,Miu_Ph,'*k')

%Plot Ellipse
a=Miu_Su*COV_Su; % horizontal radius
b=Miu_Ph*COV_Ph; % vertical radius
x0=Miu_Su; % x0,y0 ellipse centre coordinates
y0=Miu_Ph;
t=-pi:0.01:pi;
x=x0+a*cos(t);
```

```
y=y0+b*sin(t);
plot(x,y,'-k','LineWidth',8)

hold on
Miu_Su=26;
a=Miu_Su*COV_Su*Beta_i(12); % horizontal radius
b=Miu_Ph*COV_Ph*Beta_i(12); % vertical radius
x0=Miu_Su; % x0,y0 ellipse centre coordinates
y0=Miu_Ph;
t=-pi:0.01:pi;
x=x0+a*cos(t);
y=y0+b*sin(t);
plot(x,y,'-b','LineWidth',8)
Sub=X_opt_i(12,2);
Pb=X_opt_i(12,1);
plot(Sub,Pb,'-or','LineWidth',8)

legend('Unsafe Region','Initial mean values','Initial
Ellipse','Optimum ellipse', 'Optimum value')
% [xx, yy, zz] =
ellipsoid(Miu_Su,Miu_Ph,9,Miu_Su*COV_Su,Miu_Ph*COV_Ph,9*0.1,30);
% figure
% surf(xx, yy, zz)
% axis equal
```

BIOGRAPHY OF THE AUTHOR

Leon Dario Cortes Garcia was born in Medellin, Colombia, on September 10th, 1991. After finishing high school, Leon dreamed of being a Civil Engineer. Before starting his wanted profession, Leon studied Sanitary and Environmental Engineering at Universidad de Antioquia, until he got a place in Civil Engineering in Universidad Nacional de Colombia-Sede Medellín. During his undergraduate, Leon was doubting between structural and geotechnical engineering fields, until he met the professor David Zapata-Medina, who later on was his mentor, shaped his path, and formed his foundations as a geotechnical engineer.

Once Leon earned his major as Civil Engineer, he started working for a geotechnical engineering consulting company in Colombia where he went from theory to practice. After one year and a half working, Leon started his master's in civil engineering with an emphasis in Geotechnical Engineering in the University of Maine, where he improved his research and consulting skills. After finishing his Masters, Leon will continue practicing consulting for Geosyntec Consultants based in Chicago. Leon is a candidate for the Master of Science degree in Civil Engineering from the University of Maine in August 2019.